

A Nonlinear Analysis Framework for Electronic Synthesizer Circuits

François Georges Germain



Department of Music Research
McGill University
Montreal, Canada

October 2011

A thesis submitted to McGill University in partial fulfillment of the requirements for the degree of Master of Arts.

© 2011 François Georges Germain

Abstract

This thesis presents a theoretical and experimental study of the nonlinear behaviour of analog synthesizers' effects. The goal of this thesis is to evaluate and complete current research on nonlinear system modelling, both in and out of the field of music technology. The cases of single-input and multiple-input effects are considered.

We first present an electronic analysis of the circuits of common examples of analog effects such as Moog's lowpass filter and Bode's ring modulator, extracting the equations of each system. We then discuss the results of experiments made on these systems in order to extract qualitative information about the distortion found in the system input-output relationship.

Secondly, we look at the literature for methods used to model single-input nonlinear systems, and we investigate the opportunities to extend these techniques to multi-input systems. We focus on two different modelling approaches. The black-box approach seeks to model the input-output transfer function of the system as closely as possible without any particular assumption on the system. The circuit modelling approach uses the knowledge of electronic component behaviour to extract a transfer function from the known circuit of the system. The results of both approaches are compared to our experiments in order to evaluate their accuracy, identify flaws and, when possible, suggest potential improvements of the methods.

Résumé

Cette thèse présente une étude théorique et expérimentale du comportement nonlinéaire des effets de synthétiseurs analogiques. Elle vise à évaluer et compléter les recherches actuelles sur la modélisation des systèmes non-linéaires, à la fois dans le domaine de la technologie de la musique et en dehors. Les cas des effets à une ou plusieurs entrées sont examinés.

Pour ce faire, nous présentons d'abord une analyse électronique des circuits de plusieurs exemples usuels d'effets analogiques tels que le filtre passe-bas de Moog ou le modulateur en anneau de Bode. Les équations régissant chaque système en sont dérivées. Nous discutons ensuite le résultat d'expériences menées sur ces systèmes pour extraire une caractérisation qualitative de la distorsion présente dans le rapport entrée-sortie du système.

Dans un second temps, nous examinons les méthodes de modélisation des systèmes non-linéaires à une entrée trouvées dans la littérature, et nous explorons les possibilités d'extension de ces techniques aux systèmes à plusieurs entrées. Deux approches de modélisation sont abordées. L'approche boîte noire vise à modéliser la fonction de transfert entrée-sortie du système aussi fidèlement que possible sans hypothèse sur la structure du système. L'approche de la modélisation du circuit utilise quant à elle la connaissance du comportement des composants électroniques pour extraire une fonction de transfert à partir du circuit (connu) du système. Les résultats associés aux deux approches sont comparés à nos expériences pour évaluer leur performance, et identifier des lacunes et, quand c'est possible, des opportunités d'amélioration de ces méthodes.

Acknowledgments

I gratefully acknowledge McGill University and the Schulich School of Music for their financial aid, as well as the Centre for Interdisciplinary Research in Music Media and Technology (CIRMMT) and the Digital Composition Studios (DCS) for their material support.

Many thanks to my directors, Professor Philippe Depalle and Professor Marcelo M. Wanderley, for their support, advice and encouragement. Special thanks to Carolina Brum, Darryl Cameron, Yves Méthot (CIRMMT) and Richard McKenzie for their technical assistance in setting up my experiments, and to my colleagues Vincent Fréour, Joseph Thibodeau and Jason A. Hockman for their suggestions.

I am grateful to Doctor Thomas Hélie from IRCAM for sharing data about his research.

I also wish to thank Gabriel Vigliensoni, Junk Suk Lee and Hani Bakhshaei for accompanying all along the days (and sometimes the nights) in the laboratory, all the members of the lab soccer and basketball teams, and the professors and students of Music Technology in general for all the discussions we had about graduate work, research and life through these two years.

Finally, many thanks to my parents Gérard and Yvette for their never-ending support all along my graduate work at McGill.

Contents

1	Introduction	1
1.1	Project overview	1
1.2	Analog synthesis history	2
1.3	Analog synthesizers effects	3
1.4	System description	3
1.5	Nonlinear analysis	5
1.6	Distortion characterization	6
1.7	Single-input and multiple-input nonlinear models	8
1.8	Thesis' layout	9
2	Synthesizer circuits	10
2.1	Lowpass filters in synthesizers	10
2.1.1	Ladder filters	10
2.1.2	Alternative filter designs	11
2.1.3	The Moog ladder filter	11
2.2	Ring modulators	15
2.2.1	Diode-based ring modulator	15
2.2.2	Transistor-based ring modulator	17
2.3	Circuit asymmetries	19
2.3.1	Hoffmann-Burchardi's experiment	19
2.3.2	Asymmetries in symmetric stages	20
2.4	Summary	23
3	Experimental study	24
3.1	Remarks	25

3.2	Experiments on lowpass filters	26
3.2.1	Setup for measurements at the outlets	26
3.2.2	Setup for measurements on the circuit board	27
3.2.3	Cutoff frequency extraction	27
3.2.4	Distortion measurement	28
3.3	Moog filter	28
3.3.1	Input-output behaviour for a DC input	28
3.3.2	Cutoff frequency control	30
3.3.3	Harmonic distortion of the Moog filter	33
3.3.4	Influence of the frequency cutoff setting on the filter harmonic distortion	34
3.3.5	Influence of the input amplitude on the filter harmonic distortion .	36
3.4	Experiments on ring modulators	37
3.5	Korg MS-50 ring modulator	38
3.6	Moogerfooger ring modulator	40
3.7	Summary	44
4	Nonlinear modelling using black-box approach	45
4.1	Linear theory	45
4.2	Volterra series	47
4.2.1	SISO model	47
4.2.2	Laplace transform and Z-transform of the expansion	49
4.2.3	MISO model	49
4.2.4	Mathematical properties	50
4.2.5	Practical use	51
4.3	Block-based models	52
4.3.1	SISO models	52
4.3.2	MISO Hammerstein models	53
4.3.3	Number of coefficients	54
4.4	Summary	54
5	Identification methods	56
5.1	Excitation signals	56
5.1.1	Sinusoids and swept-sines	56

5.1.2	Pseudo-random and random signals	57
5.2	LTI system identification	58
5.3	Order separation	61
5.3.1	Method	61
5.3.2	Use	62
5.4	Correlation-based methods	62
5.4.1	Functional expansions	63
5.4.2	Hammerstein model	67
5.4.3	Wiener model	68
5.4.4	Polynomial Hammerstein model	69
5.4.5	Extension to two-input systems	71
5.5	Explicit least-squares method	73
5.5.1	Kernel orthogonalization	73
5.5.2	Functional expansions	73
5.5.3	Polynomial Hammerstein model	73
5.5.4	Extension to two-input systems	77
5.5.5	Computation cost	77
5.6	Swept-sine-based method	77
5.6.1	Excitation signal	77
5.6.2	Inverse signal	78
5.6.3	Extraction of the impulse responses	78
5.6.4	Extension to two-input systems	78
5.7	Summary	79
6	Applications to synthesizer circuits	80
6.1	Implementation of the identification methods	80
6.2	Moog ladder filter numerical models	81
6.2.1	Circuit modelling	81
6.2.2	Backward finite difference	81
6.2.3	Truncated Volterra series	82
6.3	Finite difference model study	84
6.3.1	Sinusoidal excitation	85
6.3.2	Even-order distortion	85

6.3.3	Distortion	87
6.3.4	Nonlinear identification	88
6.4	Nonlinear identification of the Moog ladder filter	90
6.5	Nonlinear identification of ring modulators	96
6.6	Summary	100
7	Conclusion and Future Work	102
7.1	Summary	102
7.2	Future work	103
7.3	Conclusion	104
A	Electronic components	106
A.1	Linear elements	106
A.2	Diode	106
A.3	Transistor	108
A.4	Operational amplifier	109
B	Studied synthesizers' effects	111
B.1	Moog effects	111
B.1.1	Moog 904A Lowpass filter	111
B.1.2	Moogerfooger MF-102 ring modulator	114
B.2	Korg MS-50 audio effects	114
B.2.1	Ring modulator	114
C	Experimental setups	120
C.1	Moog lowpass filter	120
C.1.1	DC excitation of the filter	120
C.1.2	Swept-sine excitation of the filter	120
C.1.3	Sinusoidal excitation of the filter	121
C.2	Korg MS-50 ring modulator	122
C.2.1	Sinusoidal excitation of the Korg ring modulator	122
C.3	Moogerfooger MF-102 ring modulator	122
C.3.1	Sinusoidal excitation of the MF-102	123

D Hermite polynomials	124
D.1 Polynomial expression	124
D.2 Extension for multi-variable polynomials	126
D.2.1 Two-variable case	127
D.2.2 N -variable case	129

List of Figures

1.1	Ring modulation using germanium or silicon diodes	4
1.2	Structure of a single-input/single-output system	8
1.3	Structure of a multi-input/single-output system	8
2.1	Examples of diode-based ladder filters	12
2.2	Moog filter — Ladder filter circuit	13
2.3	Moog filter — Filtering stage circuit	14
2.4	Moog filter — Driver stage circuit	14
2.5	Diode-based ring modulator	16
2.6	Modified diode-based ring modulator	16
2.7	Differential transistor-based amplifier stage	17
2.8	Transistor-based ring modulator	18
2.9	Frequency spectrum of the output signal of a Doepfer A-114	19
2.10	Frequency spectrum of the output signal of an unbalanced model of transistor-based ring modulator	21
2.11	Transistor-based differential amplifier	22
3.1	Experimental benchmark (1)	24
3.2	Experimental benchmark (2)	25
3.3	Experimental setup for measurements at the outlets for lowpass filters	26
3.4	Experimental setup for measurements on the circuit board for lowpass filters	27
3.5	Moog filter — Measured voltages in the case of a DC input	30
3.6	Moog filter — Magnitude response of the filter	32
3.7	Moog filter — Cutoff frequency as function of the control voltage	32
3.8	Moog filter — Input signal spectrogram of the experiment 42	33

3.9	Moog filter — Output signal spectrogram of the experiment 42	34
3.10	Moog filter — Relative magnitude of the distortion orders at resonance 0	35
3.11	Moog filter — Relative magnitude of the distortion orders at resonance ~ 7	35
3.12	Moog filter — Relative magnitude of the distortion orders at resonance 10	36
3.13	Moog filter — Variation of the distortion orders for different input amplitudes	38
3.14	Experimental setup for measurements at the outlets for ring modulators	38
3.15	Korg ring modulator — Output signal spectrum	39
3.16	MF-102 ring modulator — Output signal spectrum	41
6.1	Types of subsystem composition	83
6.2	Huovilainen model — Input and output spectra for sinusoidal excitation	85
6.3	Huovilainen model — Input and output spectra for asymmetric stages	86
6.4	Huovilainen model — Input and output spectra for input signal with DC offset	87
6.5	Huovilainen model — Distortion	87
6.6	Huovilainen model — filter of the Wiener and the Hammerstein models	88
6.7	Huovilainen model — filters of the polynomial Hammerstein model	90
6.8	Huovilainen model — Distortion of the polynomial Hammerstein model	91
6.9	Moog filter — filter of the Wiener and the Hammerstein models	92
6.10	Moog filter — filters of the polynomial Hammerstein model	93
6.11	Moog filter — Distortion of the polynomial Hammerstein model	94
6.12	Moog filter — filters of the polynomial Hammerstein model	95
6.13	Korg MS-50 ring modulator — filters of the polynomial Hammerstein model	96
6.14	Korg MS-50 ring modulator — filters of the polynomial Hammerstein model	97
6.15	MF-102 ring modulator — filters of the polynomial Hammerstein model	98
6.16	MF-102 ring modulator — filters of the polynomial Hammerstein model using explicit least-squares	99
A.1	Diode	107
A.2	Diode I-V relationship in the forward region	108
A.3	NPN bipolar junction transistor	109
A.4	Operational amplifier	110
B.1	Moog ladder filter 904A	112
B.2	Circuit of the Moog lowpass filter	116

B.3	Adder circuit of the Moog lowpass filter	117
B.4	Input buffer circuit of the Moog lowpass filter	117
B.5	Output buffer circuit of the Moog lowpass filter	118
B.6	Filtering circuit of the Moog lowpass filter	118
B.7	Moogerfooger MF-102	119
B.8	Ring modulator interface of the Korg MS-50	119
B.9	Ring modulator circuit of the Korg MS-50	119

List of Tables

3.1	Measurement of the control voltage coming from the DAC	31
3.2	Estimated frequency range values for the range switch	33
3.3	Amplitudes of odd-order distortion of a simple nonlinear system	37
3.4	Korg ring modulator — Strongest peaks in the output signal spectrum (1st experiment)	40
3.5	Korg ring modulator — Strongest peaks in the output signal spectrum (2nd Experiment)	40
3.6	Comparison of the two output signal spectra of the Korg	40
3.7	MF-102 ring modulator — Strongest peaks in the output signal spectrum (1st Experiment)	42
3.8	MF-102 ring modulator — Strongest peaks in the output signal spectrum .	43
3.9	Comparison of the two output signal spectra of the MF-102	43
4.1	Examples of SISO nonlinear block-based models	53
4.2	Examples of MISO nonlinear block-based models	54
4.3	Computational complexity of SISO nonlinear block-based models	54
6.1	Huovilainen model — Polynomial coefficients of the Wiener model	89
6.2	Huovilainen model — Polynomial coefficients of the Hammerstein model .	89
6.3	Huovilainen model — Estimation error of the polynomial Hammerstein model	90
6.4	Moog filter — Polynomial coefficients of the Wiener model	92
6.5	Moog filter — Polynomial coefficients of the Hammerstein model	93
6.6	Moog filter — Estimation error of the polynomial Hammerstein model . . .	94
6.7	Moog filter — Estimation error of the polynomial Hammerstein model using explicit least-squares	94

6.8	Korg MS-50 ring modulator — Estimation error of the polynomial Hammerstein model	97
6.9	Korg MS-50 ring modulator — Estimation error of the polynomial Hammerstein model using explicit least-squares	98
6.10	MF-102 ring modulator — Estimation error of the polynomial Hammerstein model	98
6.11	MF-102 ring modulator — Estimation error of the polynomial Hammerstein model using explicit least-squares	99
B.1	Frequency range values for the range switch	113
C.1	Moog filter with DC excitation — Experimental set-ups	120
C.2	Moog filter with DC excitation — Experimental variables	121
C.3	Moog filter with swept-sine excitation — Experimental set-ups	121
C.4	Moog filter with swept-sine excitation — Experimental variables	121
C.5	Moog filter with sinusoidal excitation — Experimental set-ups	122
C.6	Moog filter with sinusoidal excitation — Experimental variables	122
C.7	Moog filter with noise excitation — Experimental set-ups	122
C.8	Moog filter with noise excitation — Experimental variables	123
C.9	Korg ring modulator with sinusoidal excitation — Experimental variables	123
C.10	MF-102 ring modulator with sinusoidal excitation — Experimental variables	123

List of Acronyms

ADC	Analog-to-Digital Converter
ARMA	Autoregressive Moving Average
BJT	Bipolar Junction Transistor
LFO	Low Frequency Oscillator
LTI	Linear Time-Invariant
MLS	Maximum-Length Sequence
OPA	Operational (Voltage) Amplifier
VAF	Variance Accounted For
VCF	Voltage-Controlled Filter
VCO	Voltage-Controlled Oscillator
WDF	Wave Digital Filter

List of Abbreviations

Ampl.	Amplitude
Ctrl.	Control
Exp.	Experiment
Freq.	Frequency
Reson.	Resonance
Volt.	Voltage

List of Notations

$\langle \cdot \rangle_n$	n -dimensional scalar product
$E[\cdot]$	expectation
$Var(\cdot)$	variance
$\mathcal{FT}(\cdot)$	Fourier transform
$\cdot *_x \cdot$	convolution relatively to the variable x
$\mathcal{H}^{(m_1, \dots, m_k)}$	Hermite polynomial of order (m_1, \dots, m_k)
$\mathcal{H}_{\mathcal{N}}^{(m_1, \dots, m_k)}$	normalized Hermite polynomial of order (m_1, \dots, m_k)
ϕ_{xx}, ϕ_{xy}	autocorrelation and cross-correlation of x and y
S_{xx}, S_{xy}	power and cross spectral density of x and y
μ_x	mean of x
σ_x	standard deviation of x
F	functional describing the behaviour of the system
F_{m_1, \dots, m_k}	kernel of the functional expansion of order (m_1, \dots, m_k)
$h(\cdot), h[\cdot]$	function (continuous and discrete)
$\hat{h}(\cdot)$	function estimation
M	order of the system
N	length of the model filters (in samples)
x or $X = [x_1, \dots, x_k]^T$	input signal(s)
y	output signal
t, n	time (continuous and discrete)
τ	delay (both continuous and discrete)
f	frequency
$\delta(t)$ or $\delta[n]$	Dirac function
$X[k, :], X[:, l]$	k -th row and l -th column of matrix X

Chapter 1

Introduction

In the last decade, virtual analog synthesis has become a recurrent topic in computer music research. Both the popularity of analog synthesizers and the increasing computational power of modern computers have made it possible to accurately reconstruct the very typical sound of electronic audio effects.

The motivation of such research lies in the artistic desire of a generation of composers and musicians to access the particular features or sounds that were characteristic of these vintage devices. However, the scarce availability of this material and the disappearance of manufacturers, combined with their intrinsic disadvantages, such as cost or use of obsolete components, make the application of original effects often impractical and/or impossible: thus, the preservation of the sound and their reproduction on modern platforms and, in particular, computers.

This thesis comes aims to address these concerns by attempting to unify current approaches to the reproduction of vintage analog sound using electronic effects.

1.1 Project overview

This research project aims to identify and characterize the sources of nonlinear behaviour in electronic synthesizers' effects, and then to evaluate the opportunities to use various existing nonlinear modelling approaches to integrate properly these behaviours in simulating these effects.

The main focus of this thesis will be on one-input/one-output systems due to the richer literature on such systems, especially in the domain of audio and electronic music. However,

we will also study the possibilities to extend our observations and conclusions to the case of multi-input systems.

The comparison of the different modelling approaches will in particular look at the difference of performance between methods with different levels of information on the system.

1.2 Analog synthesis history

The invention of modular analog synthesizers was a major breakthrough in the field of electronic music, providing performers with a powerful medium to create a variety of new sounds without the need of specific knowledge in electronics or computers, while using familiar forms and features. Following the work of precursors such as H. Le Caine and its Electronic Sackbut (Young 1989), three men independently invented analog synthesizers in 1964: R. Moog, P. Ketoff and D. Buchla (Chadabe 2000). The first Moog's model comprised of two *voltage-controlled oscillators* (VCO) and his now famous *voltage-controlled filter* (VCF). These new instruments quickly met commercial viability, becoming an essential element in electronic music production. The general structure of analog synthesizers has stayed quite the same since then, based on a modular architecture with subsystems performing specific tasks, such as oscillators, filters, noise generators, and amplifiers. The difference between the devices is in the internal circuit design of these modules developed by manufacturers.

Synthesis software along with cheaper, simpler and more compact digital synthesizers, where signal generation and processing is performed by digital processors, and then synthesis software have progressively replaced earlier analog synthesizers as sound synthesis platforms during the 1980's and the 1990's. However, some users were not satisfied with these new devices since they were deemed to sound less "warm" due in part to the absence of the nonlinearities introduced by analog circuits and that is why systems such as the Moog ladder filter remained very popular in the electronic music community.

This fact led, on the one hand, to the continuation of analog synthesizer manufacturing on a smaller scale, and on the other hand, to the invention of *virtual analog* synthesis. In a similar way as acoustic instrument modelling is made, virtual analog devices try to emulate the behaviour of analog synthesizers. Two issues have been identified in this modelling process (Välämäki and Huovilainen 2006). Concerning the signal sources, it is necessary to deal with the presence of aliasing due to the sampling of fast time-varying

signals, which may contain infinitely high-frequency components. Concerning the effects, nonlinear behaviour of the electronic circuits has to be taken into account. This thesis will focus on the latter.

1.3 Analog synthesizers effects

Voltage-controlled filters Explored as early as the 1940s by pioneers such as H. Le Caine (Young 1989), the voltage-controlled filter (VCF) quickly became a basic component of electronic sound producing devices, and in particular of modular synthesizers. The design of this effect varies from one device to another.

The Moog ladder filter The Moog ladder filter is probably the most famous analog effect ever produced. Patented in the 1969 (Moog 1969), this filter has appeared on most of the commercial Moog synthesizers. It has also been emulated on numerous digital or computer platforms due to its popularity in the music community.

Ring modulators The ring modulator was used as early as the 1930s for communication applications (Davies 1976). Its introduction in electronic music started in the mid-1950s as part of two well-known devices: the vocoder and the frequency shifter. Then, it was popularized as an independent effect in pieces by Stockhausen (Stockhausen 1967). First designs of ring modulators had diodes in switching mode what made them useless for sound modifications due to the very harsh sounds they produced (Bode 1984). However, the introduction of new germanium diodes and the use of the diode circuits in the “square law region” of the diodes (Fig. 1.1) allowed the use of ring modulators as four-quadrant signal multipliers that proved to be musically interesting. Bode developed his own multiplier ring modulator in 1959-60, later included as an effect in the Moog modular synthesizer (Bode 1961, 1967, 1984).

1.4 System description

We define here the quantities that will appear in the mathematical system descriptions and in the models developed later in this thesis.

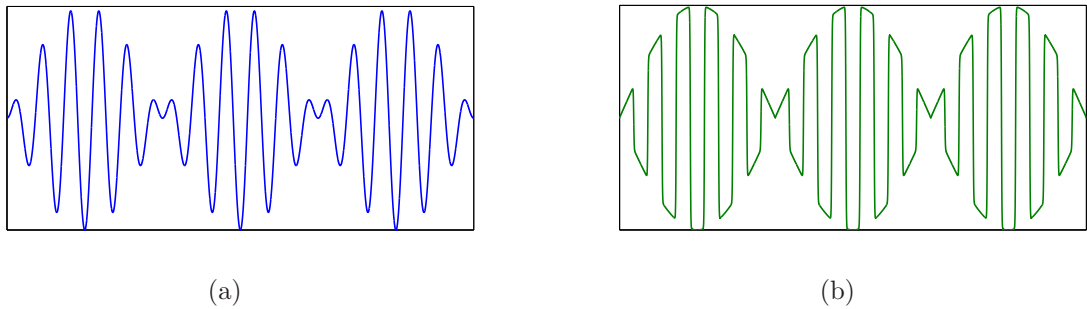


Fig. 1.1 Ring modulation using (a) germanium — quadratic mode — or (b) silicon diodes — switching mode — (after Bode 1984)

Time The time is denoted by the variable t . The sample of a signal is identified with the variable n , with the convention that the sample with the index $n = 0$ occurred at time $t = 0$.

Inputs and Outputs Since the systems studied here may have multiple input signals (x_1, x_2, \dots, x_n) considered as being infinitely-differentiable bounded functions of the time, the inputs can be denoted using the vector $X = [x_1 \dots x_n]^T$. This thesis deals only with **single-output** systems so the output is simply denoted by the function of time y .

Functionals The behaviour of a system is described by a *functional* denoted F . Functionals are functions of functions, since here every point of the output may depend on the input signals as a whole. Then, F transforms input *functions* in another function. The input/output relationship is expressed by

$$y(t) = F[t, X](t) \quad (1.1)$$

Time-invariance In this thesis, as in most of the reviewed literature, we deal only with *time-invariant* systems, which means that the behaviour of the system under study is independent of the choice of the time origin. Mathematically, if we describe the behaviour of the system using the functional F that transforms the input X into the output Y , the time-invariance means that this functional does not depend **explicitly** on the time variable

t (even if, of course, inputs are time-varying signals):

$$y(t) = F[t, X](t) = F[X](t) \quad (1.2)$$

In this thesis, we assume that the systems are time-invariant, which leads us to the following hypotheses:

- In the case of electronic systems, it is well-known that the behaviour of electronic components can vary depending on their temperature (Sedra and Smith 1997). Here we consider the systems as being at constant usual temperature ($\approx 25^\circ\text{C}$) for modelling considerations;
- The control parameters of the systems can vary in time. However, we assume here that they are not varying, or varying slowly enough so that the system can be considered as being in a quasi-time-invariant state at all times.

Causality The common physical assumption of causality is valid here as well. It means that the system functional F depends only on the past and the present of the inputs (ie. $X(s)$ for $s \leq t$).

1.5 Nonlinear analysis

Most of the physical systems are actually nonlinear. The use of linear theory in science is usually made possible in cases where the influence of nonlinearities is negligible. For example, this is the case for linear acoustics, used to simulate acoustic waves in rooms. However these approximations are sometimes insufficient to characterize physical systems in a satisfactory way. In such cases, the use of nonlinear analysis is necessary to achieve a proper description of the behaviour of the system.

The simulation and the optimization of linear systems is a field mastered in mathematics and physics. In signal processing, several methods have been drawn to determine the characteristics of any linear systems that one can represent in Fourier analysis either as an impulse response or as a transfer function (which is equal to the Fourier transform of the impulse response).

On the contrary, the identification of nonlinear systems is an ongoing field of research. This research involves the definition of appropriate nonlinear models as well as the development of identification techniques in order to parametrize these models from existing systems.

Nonlinear models Generic models for nonlinear systems were first developed from the work of Volterra in 1887 (Volterra 1930) on the mathematical theory of analytic functions. His theory is an extension of Taylor series, which considered memory effects, and is nowadays called the Volterra series. However, models based on this expansion are not often used both because of their complexity and of the number of parameters needed to describe strongly nonlinear systems, requiring too much computation power. Wiener was one of the first to specifically study the problem of parameter estimation for nonlinear systems (Wiener 1958) in the 1950's. He simplified the approach of the Volterra series by cascading a memoryless nonlinear block and a memory linear block. Many other models (Bendat 1998; Chang and Luus 1971; Chen and Billings 1989; Greblicki 1997; Sorenson 1985) have been studied in various research areas (Giannakis and Serpedin 2001) since then, focusing on simplifying and adapting different frameworks to build relevant representations with fewer parameters to compute.

Model identification While the parametrization of linear systems is relatively easy, the extraction of the numerous parameters of a nonlinear model from measurement on the systems can be difficult due both to the necessity of separating the response of the different nonlinear elements used in modelling (e.g., the different powers of a polynomial expansion) and to the extraction of their respective parameters. This fact explains why numerous techniques are based on noise excitation of the systems, allowing extraction of the different parameters through decorrelation techniques.

1.6 Distortion characterization

When using synthesizers, the audio effects are often used with oscillators that produce harmonic signals (e.g., sinusoid, sawtooth, square). For this reason, distortion in audio is often characterized relatively to the nonlinearities related to signals with distinct components.

Harmonic distortion This distortion is the one observed when a system is excited by a single-component signal at frequency f . In the case of nonlinearities, we observe the presence of harmonic components in the system output (e.g., components at frequency $2f$, $3f$, $4f, \dots$).

Total harmonic distortion A common way to measure distortion in a system is called Total Harmonic Distortion (THD). In the case of harmonic distortion, it measures the relative power between the component originally present in the signal and the total power of the harmonics introduced by the system nonlinearities. If we denote $P(f)$ the power of the signal component at frequency f , this quantity is given by:

$$THD(f) = \frac{\sum_{n=2}^{+\infty} P(nf)}{P(f)} \quad (1.3)$$

As we can see, this quantity depends on the frequency of the component. In many systems, we also observe a dependence of that quantity on the amplitude (or the power) of that component.

Intermodulation distortion The harmonic distortion can be insufficient to characterize correctly the behaviour of a nonlinear system in audio since input signals can consist of several components and/or several signals can be involved (multi-input effects). The distortion is observed at non-harmonic frequencies when the system is excited by two components f_1 and f_2 . In that case, we usually observe the presence of intermodulation components in the system output (e.g., components at frequency $f_1 - f_2$, $f_1 + f_2$, $2f_1 - f_2$, $f_1 + 2f_2, \dots$)

Distortion order As we will see in Chapter 4, nonlinear models can always be expressed as an infinite sum of polynomials of the signal samples. A polynomial of order n is always related to the harmonic distortion at frequencies up to nf . In the case of two single-component input signals, a polynomial of order (n, m) (ie. $x^n y^m$) relates to the intermodulation distortion at frequency $nf_1 + mf_2$. Thus, to simplify, we refer to distortion components in the output signal with such polynomial order (e.g., $3f_1$ is the 3rd-order distortion, and $2f_1 + f_2$ is the (2,1)-order distortion).

1.7 Single-input and multiple-input nonlinear models

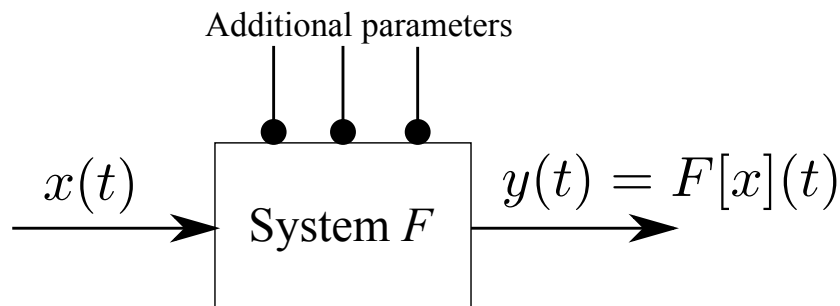


Fig. 1.2 Structure of a single-input/single-output (SISO) system¹

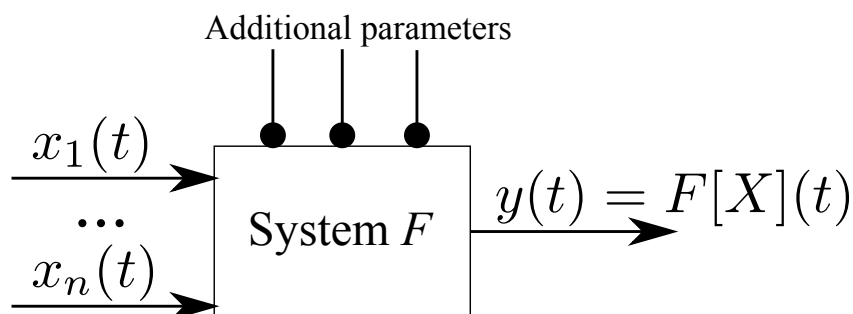


Fig. 1.3 Structure of a multi-input/single-output (MISO) system

The most common case of audio systems encountered in literature are *single-input/single-output* (SISO) systems, with the possibility of additional parameters (Fig. 1.2). As a consequence, most of the research on nonlinear models in audio applications focuses on SISO structures. In analog synthesizers, several examples of SISO effects can be found, such as amplifiers, filters, reverberators or envelope followers. In this thesis, we also look at multiple-input configuration (Fig. 1.3). If this configuration is less present in the literature about electronics, it has been studied in domains such as telecommunications (e.g., frequency conversion (Rice 1973)) or biomedical engineering (e.g., binocular vision modelling (Hall and Hall 1977)).

¹Convention for system structure drawing is based on (Durr 1976)

1.8 Thesis' layout

This thesis is organized as follows. First, we look at the effects' circuits and the different sources of nonlinearities that can be found analytically in Chapter 2. These sources are observed experimentally in Chapter 3. Then, we explore the different approaches in non-linear modelling as well as parameter extraction methods in Chapters 4 and 5. Finally, we apply these techniques to the studied systems and compare the behaviour of the models to the measurements made earlier in Chapter 6.

Chapter 2

Synthesizer circuits

As mentioned in the introduction, this thesis focuses on the study of nonlinear circuits present in electronic synthesizers. Many electronic effects have been developed since the 1950's. Due to the presence of nonlinear components in the circuits, such as diodes and transistors, the behaviour of these synthesizers was nonlinear. This gave their sound a colouration particular to each device. In this section, we review the various designs encountered for two different and popular effects: the lowpass filter as a weakly nonlinear system, and the ring modulator as a strongly nonlinear system.

The different characteristics of the electronic components involved in the design of these effects are presented in Appendix A.

2.1 Lowpass filters in synthesizers

The lowpass filter is one of the most common effects on electronic synthesizer. Its design varies from one device to another. It is often used as an example of a weakly nonlinear system, in the sense that its total harmonic distortion (see Section 1.6) is low and does not involve audible high orders of distortion (usually up to order 5).

2.1.1 Ladder filters

A popular design for lowpass filters is the ladder filter structure first introduced by Robert Moog. This approach consists of stacking several identical filter stages. The use of transistor-based filtering stage was patented by Moog in 1969 (Moog 1969) so all sub-

sequent designs used diodes instead. Examples of such diode-based designs were present in the Roland TB-303 (Fig. 2.1(a)), Doepfer A-102 (Fig. 2.1(b)), EMS (Figs. 2.1(c) and 2.1(d)), PE Minisonic (Fig. 2.1(e)) and Roland 100 (Fig. 2.1(f)) synthesizers (Stinchcombe 2008).

There have been some studies that investigate these designs. An example is the study of the EMS VCS3 filter by Fontana (Fontana and Civolani 2010). The design of this filter is unique in that each filtering stage is not buffered from the next, which differentiates them from the transistor-based design of Moog (Stinchcombe 2008). This characteristic makes them harder to study analytically.

2.1.2 Alternative filter designs

Another example of lowpass filter design is the one implemented in Korg synthesizers of the late 1970's (e.g., MS-10, MS-20). The popularization of operational transconductance amplifiers allowed the implementation of active electronic effects such as voltage-controlled filters. A study of the lowpass filter circuits of the MS-10 and the MS-20 is presented in Stinchcombe (2006). Later Korg designs also explored circuits using a diode ring as it can be seen on the Korg MS-50 schematics (Korg 1978).

2.1.3 The Moog ladder filter

The device developed by Moog in the 1960's is the main example of transistor-based ladder filter. This famous device has been thoroughly studied in literature (Hélie 2010; Huovilainen 2004; Stilson and Smith 1996) with the purpose of developing always better digital models reproducing the typical nonlinear effects of this system.

Device The interface of the Moog lowpass filter 904A (1969 model) can be seen on Fig. B.1. The device has one input, one output and three control inputs to control filter cutoff through voltage. As explained in Appendix B.1.1, the three control inputs are simply added to get one single voltage control value.

Filter circuit The Moog filter uses the base-to-emitter resistance of bipolar transistors to build several RC filter circuits (Huovilainen 2004). The filter consists of four of such stages (Fig. 2.2), each of which comprising two BJTs and one capacitor (Fig. 2.3). A last

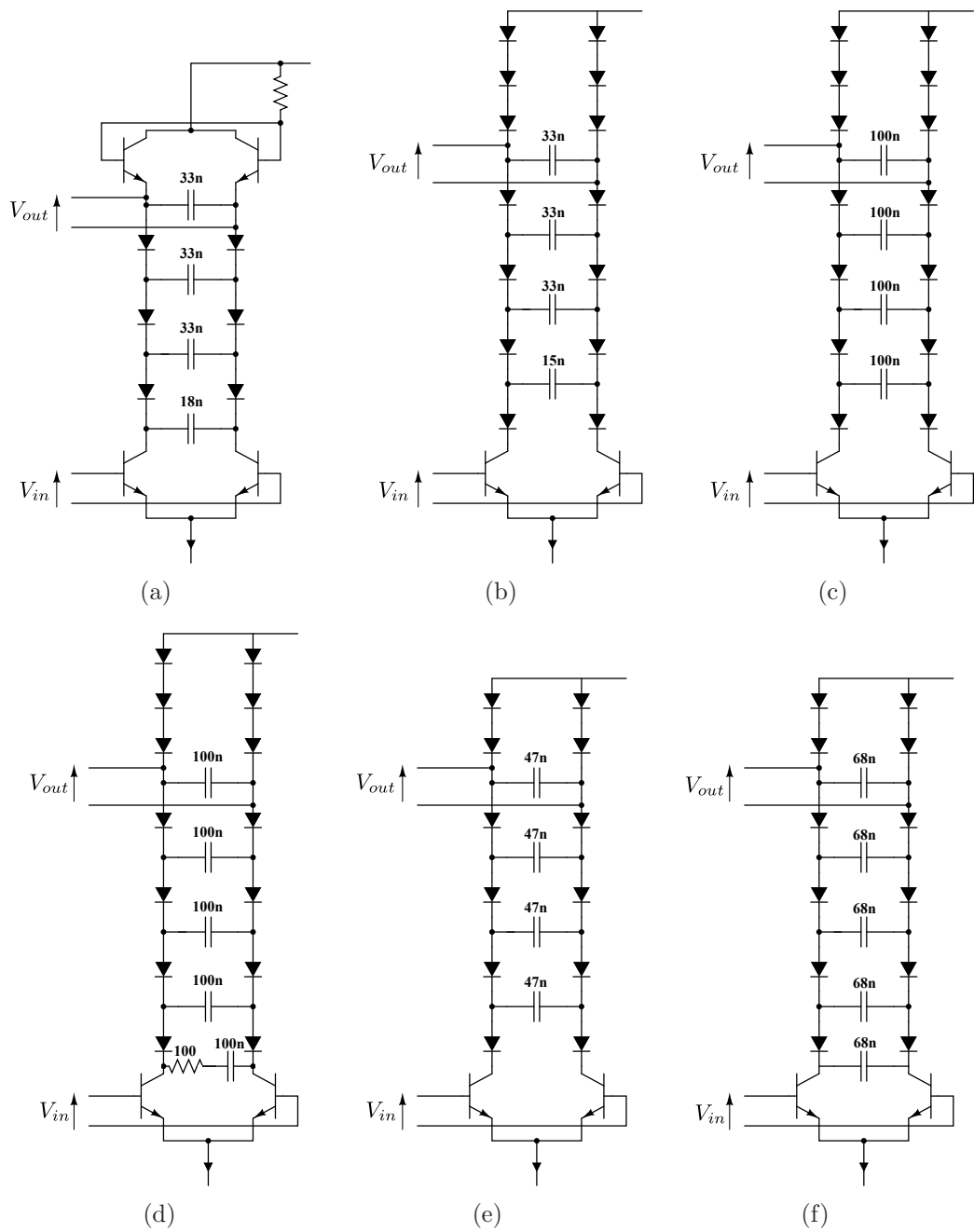


Fig. 2.1 Examples of diode-based ladder filters: (a) Roland TB-303, (b) Doepfer A-102, (c) EMS early version, (d) EMS late version, (e) PE Minisonic, (f) Roland 100 (after Stinchcombe 2008)

part is the driving stage (Fig. 2.4) which is connected to the filter input and to the control circuit, usually modelled as a control current source varying with the cutoff frequency control parameter of the filter.

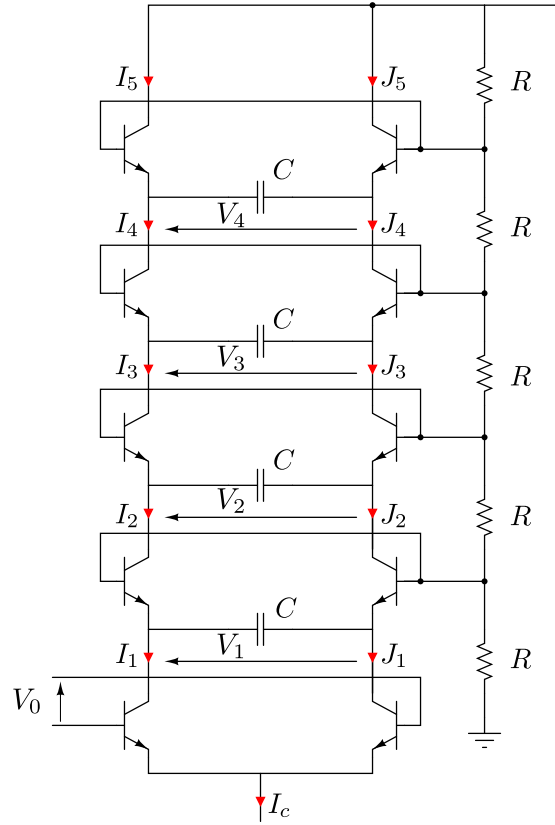


Fig. 2.2 Moog filter — Ladder filter circuit

Equations The equations related to the filter stage have been derived in literature (Hélie 2010). We use the notations as displayed in Figs. 2.2 and 2.3.

If we take the usual assumption that the base current of all transistors in the circuit is negligible ($I_B \ll I_E$), each stage follows:

$$2C \frac{dV_n}{dt} = -I_c \left(\tanh \frac{V_n}{2V_T} - \tanh \frac{V_{n-1}}{2V_T} \right) \quad (2.1)$$

By using the notation (Hélie 2010), $v_n = V_n/2V_T$ and $\omega = I_c/4CV_T$, the system is driven

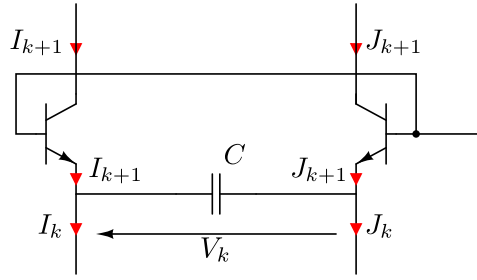


Fig. 2.3 Moog filter — Filtering stage circuit

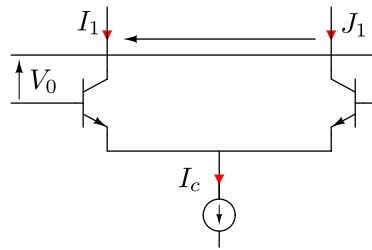


Fig. 2.4 Moog filter — Driver stage circuit

by the equations:

$$\frac{1}{\omega} \frac{dv_n}{dt} + \tanh v_n = \tanh v_{n-1} \quad \text{for } n = 1, 2, 3, 4 \quad (2.2a)$$

$$v_0 = v_{in} - 4rv_4 \quad (2.2b)$$

We see that the linearized version of Eq. (2.2a) is given by:

$$\frac{1}{\omega} \frac{dv_n}{dt} + v_n = v_{n-1} \quad (2.3)$$

which corresponds to the equation of a RC filter where the resistance is induced by the transistors as $4V_T/I_c$.

The quantity $\omega/2\pi$ represents the cutoff frequency of the linearized filter, r is related to the resonance profile of the filter and v_{in} is related to the nominal input voltage and the

input stage gain of the module. Their typical values are then given by (Hélie 2010):

$$20\text{Hz} \leq \frac{\omega}{2\pi} \leq 10\text{kHz}, \quad 0 \leq r < 1, \quad |v_{in}| < 5 \quad (2.4)$$

2.2 Ring modulators

Ring modulator is another example of common module found on most existing synthesizers. This circuit is ideally supposed to perform a multiplication between the two input signals known as the modulator $m(t)$ and the carrier $c(t)$:

$$y(t) = m(t).c(t) \quad (2.5)$$

We then see that the ring modulator is intrinsically a nonlinear effect. However, in its ideal behaviour, this nonlinearity should be confined to the (1,1) order. The purpose of the nonlinear modelling in this case is to evaluate in what existing systems diverge from this ideal characteristic.

In terms of electronic design two schemes have been implemented using either diodes or transistors.

2.2.1 Diode-based ring modulator

This design is the first one developed using diodes. It was the one used by Bode (Bode 1984) on the ring modulator embedded in first Moog's synthesizers.

Circuit As presented in Fig. 2.5 the diode-based ring modulators consist of four germanium diodes and 2 centre-tapped transformers. The carrier signal is the tension u_C , the modulator signal is u_M , and the output signal is u_A . Hoffmann-Burchardi simplified the circuit (Hoffmann-Burchardi 2008) for modelling purpose, using a simple ideal model for the transformers as shown in Fig. 2.6. The capacitor C_p is introduced to regulate the model, R_M and R_i are source resistances, and R_A is the load resistance.

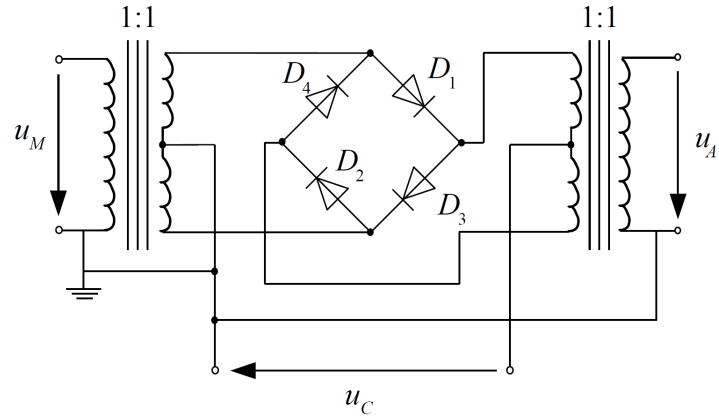


Fig. 2.5 Diode-based ring modulator (Hoffmann-Burchardi 2008)

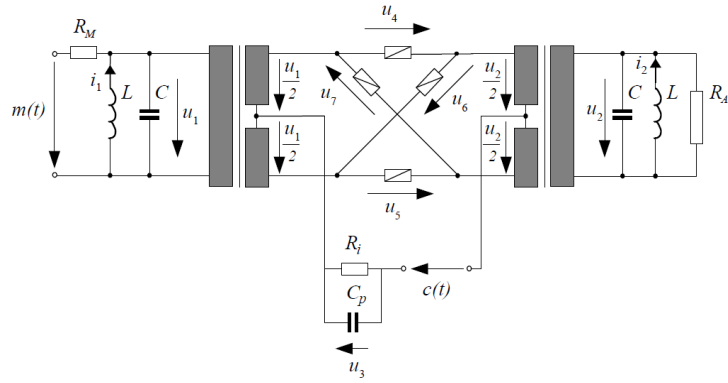


Fig. 2.6 Modified diode-based ring modulator (Hoffmann-Burchardi 2008)

Equations Using Kirchoff's current laws we can extract the five ordinary differential equations of order 1 (Hoffmann-Burchardi 2008):

$$C \frac{du_1}{dt} = i_1 - \frac{g(u_4)}{2} + \frac{g(u_5)}{2} - \frac{g(u_6)}{2} + \frac{g(u_7)}{2} - \frac{u_1 - m(t)}{R_M} \quad (2.6a)$$

$$C \frac{du_2}{dt} = i_2 + \frac{g(u_4)}{2} - \frac{g(u_5)}{2} - \frac{g(u_6)}{2} + \frac{g(u_7)}{2} - \frac{u_2}{R_A} \quad (2.6b)$$

$$C_p \frac{du_3}{dt} = g(u_4) + g(u_5) - g(u_6) - g(u_7) - \frac{u_3}{R_i} \quad (2.6c)$$

$$L \frac{di_1}{dt} = -u_1 \quad (2.6d)$$

$$L \frac{di_2}{dt} = -u_2 \quad (2.6e)$$

where g is the V-I characteristic of the diodes.

Kirchhoff voltage laws provide 4 more equations:

$$u_4 = \frac{u_1}{2} - u_3 - c(t) - \frac{u_2}{2} \quad (2.7a)$$

$$u_5 = -\frac{u_1}{2} - u_3 - c(t) + \frac{u_2}{2} \quad (2.7b)$$

$$u_6 = \frac{u_1}{2} + u_3 + c(t) + \frac{u_2}{2} \quad (2.7c)$$

$$u_7 = -\frac{u_1}{2} + u_3 + c(t) - \frac{u_2}{2} \quad (2.7d)$$

that completely characterize the system.

2.2.2 Transistor-based ring modulator

This design was introduced later in synthesizers when transistors became more popular and replaced diodes in electronic circuits. In particular, it corresponds to the ring modulator embedded in the Korg MS-50 using an RC4200 integrated circuit as can be seen on the schematics (B.8).

Circuit The circuit consists of three differential amplifier stages (Fig. 2.7) each composed of two transistors.

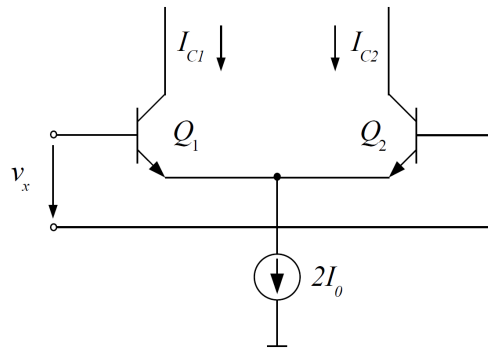


Fig. 2.7 Differential transistor-based amplifier stage (Hoffmann-Burchardi 2009)

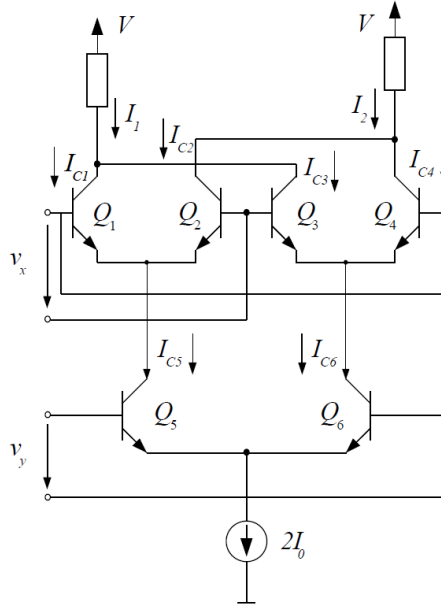


Fig. 2.8 Transistor-based ring modulator (Hoffmann-Burchardi 2009)

Equations Using the notations used by Hoffmann-Burchardi (Hoffmann-Burchardi 2009) the behaviour of the differential amplifier stage is expressed as follows:

$$I_{C1}(t) - I_{C2}(t) = 2I_0 \tanh \frac{v_x(t)}{2V_t} \quad (2.8)$$

Then the output can be written using the difference of the currents I_1 and I_2 as a function of the input voltages $v_x(t)$ (carrier) and $v_y(t)$ (modulator):

$$\Delta I(t) = I_1(t) - I_2(t) = 2I_0 \tanh \frac{v_x(t)}{2V_t} \tanh \frac{v_y(t)}{2V_t} \quad (2.9)$$

Furthermore, Hoffmann-Burchardi argues that linearizing resistors are commonly used at the emitter of the transistors Q5 and Q6 such that $\tanh \frac{v_y(t)}{2V_t} \rightarrow \frac{v_y(t)}{2V_t}$. Thus the behaviour of the system can be approximated by:

$$\Delta I(t) = I_1(t) - I_2(t) = 2 \frac{v_y(t)}{2V_t} \tanh \frac{v_x(t)}{2V_t} \quad (2.10)$$

2.3 Circuit asymmetries

2.3.1 Hoffmann-Burchardi's experiment

Experiment In a recent paper, Hoffmann-Burchardi noticed some unexpected distortion in the transistor-based ring modulators similar to the one present on the EMS VCS3 ring modulator and the Doepfer A-114 module (Hoffmann-Burchardi 2009).

In his experiment he applied two sinusoids at 100Hz and 1kHz to a Doepfer A-114. According to the ideal ring modulator equation (Eq. (2.5)), if one applies two sinusoids at f_m (modulator) and f_c (carrier) one should expect two peaks in the output signal spectrum at $f_m \pm f_c$ assuming the usual convention that $f_m > f_c$. While the frequency spectrum of the output signal (Fig. 2.9) exhibits large peaks at 900Hz ($f_m - f_c$) and 1100Hz ($f_m + f_c$), it also has at 100Hz (f_c), 200Hz ($2f_c$), 1kHz (f_m) and 2kHz ($2f_m$).

In case of the equations given by Hoffmann-Burchardi, we would have either Eq. (2.10) (circuit with linearizing resistors) and a spectrum with peaks located at $f_m \pm kf_c$ (with k odd) or Eq. (2.10) (circuit without linearizing resistors) with peaks located at $kf_m \pm lf_c$ (k and l odds).

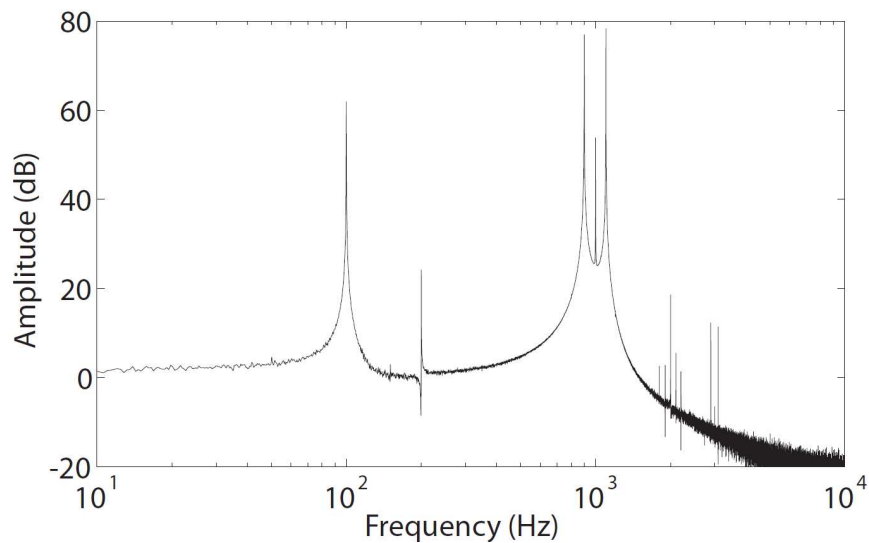


Fig. 2.9 Frequency spectrum of the output signal of a Doepfer A-114, applying two sinusoids at 100Hz and 1kHz (Hoffmann-Burchardi 2009)

Asymmetry hypothesis After these observations, Hoffmann-Burchardi drew the hypothesis that these non-expected peaks in the spectrum were due to asymmetries in the

behaviour of real circuits. Indeed, all the circuits discussed in this thesis are of symmetrical designs. This symmetry is made on the assumption that the electronic components are identical and the distribution of currents is balanced between the two symmetrical parts of the circuit.

Hoffmann-Burchardi tested that hypothesis by considering an unbalanced splitting of the current between the two branches of the modulator input stage (I_{C5} and I_{C6} in Fig. 2.8). This assumption changes the result found in Eq. (2.10) and leads to the output signal:

$$\Delta I(t) = I_1(t) - I_2(t) = 2\frac{v_y(t)}{2V_t} \tanh \frac{v_x(t)}{2V_t} + 2\delta I \tanh \frac{v_x(t)}{2V_t} \quad (2.11)$$

where δI is the small amount of current that goes in the left branch instead of the right one.

In the equation, we see that some of the carrier signal leaks to the output, even in the absence of a modulator signal. This leakage results in the presence of peaks at $k f_c$ (k odd) in the frequency spectrum of the output signal.

Hoffmann-Burchardi performed a circuit analysis on the ring modulator by slightly changing the saturation current of each transistor (see transistor's characteristics in Section A.3). The output frequency spectrum of the model as displayed in Fig. 2.10 exhibits peaks at 100Hz, 1kHz and 2kHz and $3\text{kHz} \pm 100\text{Hz}$. Thus, some of the peaks present on the measured signal appear on this spectrum. However, the intensities of these peaks are still inaccurate and major peaks such as the one at 200Hz are still missing.

Hoffmann-Burchardi suggests that the replacement of the ideal current source I_0 by the actual circuitry present on synthesizer's could be a significant improvement. He also suspects the presence of leakage currents in the modulator input stage that would add nonlinearities in the preprocessing of the input. He mentions that the design of the EMS VCS3 ring modulator is such that a portion of the carrier signal is added to the modulator signal and vice versa in an attempt to reduce the influence of such leakages.

2.3.2 Asymmetries in symmetric stages

As we saw earlier in this chapter, the effects studied in this thesis are composed of stacked stages with symmetrical designs (Figs. 2.2 and 2.8).

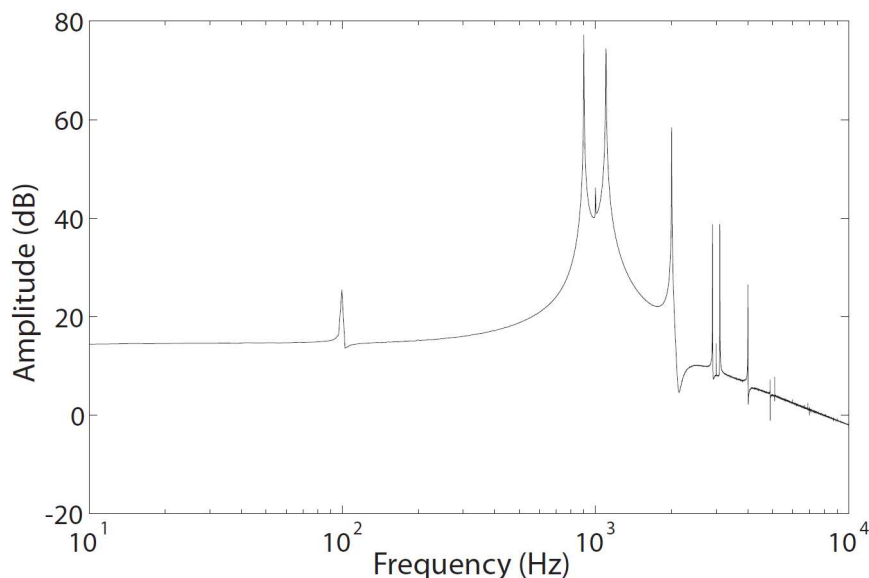


Fig. 2.10 Frequency spectrum of the output signal of an unbalanced model of transistor-based ring modulator, applying two sinusoids at 100Hz and 1kHz (Hoffmann-Burchardi 2009)

Non-ideal BJT Considering the model of the BJT presented in Appendix A, the main parameter we can change is the saturation current I_S . In this section, we consider the case where each BJT in the studied circuits has a saturation current equal to kI_S where I_S is the reference saturation current of the BJT model and k is a coefficient such that $k = 1 + \delta$ where δ is negligible compared to 1.

Differential amplifier stage This stage is used in the transistor-based ring modulator (Fig. 2.11) as well as in the driver stage of the Moog filter (Fig. 2.4). It is composed of two transistors Q1 and Q2 which coefficients are denoted k_1 and k_2 .

If we make the usual assumptions (no base current for each transistor, see Section 2.1.3), and we use the calculation scheme presented in H elie (2010), the following equations:

$$I_{C1} + I_{C2} = 2I_0 \quad (2.12)$$

$$I_{C1}/I_{C2} = e^{-v_x/V_T} \quad (2.13)$$

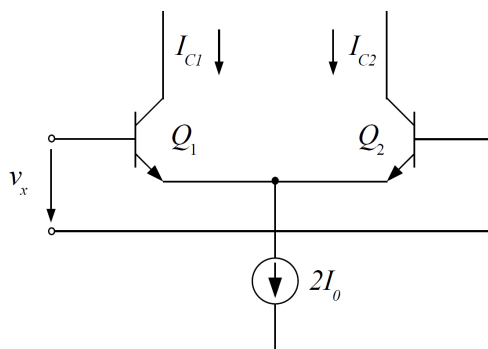


Fig. 2.11 Transistor-based differential amplifier (Hoffmann-Burchardi 2009)

are no longer valid. The asymmetries introduce imperfections such that Eq. (2.13) becomes:

$$I_{C1} + I_{C2} = 2I_0 \quad (2.14)$$

$$I_{C1}/I_{C2} = k_1/k_2 e^{-v_x/V_T} = e^{-v_x/V_T + \log k_1 - \log k_2} \quad (2.15)$$

which leads to the amplification relation:

$$\Delta I = I_{C1} - I_{C2} = 2I_0 \frac{I_{C1}/I_{C2} - 1}{I_{C1}/I_{C2} + 1} = 2I_0 \tanh \left(-\frac{v_x}{2V_T} + \beta \right) \quad (2.16)$$

where $\beta = \frac{1}{2} (\log k_1 - \log k_2)$.

We see that the only modification compared to the ideal relation $\Delta I = 2I_0 \tanh \left(-\frac{v_x}{2V_T} \right)$ is the shift β in the hyperbolic tangent expression, that introduces even-order distortion in the stage response.

Filtering stage A similar calculation in the case of the filtering stage used for the Moog (Fig. 2.3) changes the original relation found in Section 2.1.3:

$$2C \frac{dV_n}{dt} = -I_c \left[\tanh \frac{V_n}{2V_T} - \tanh \frac{V_{n-1}}{2V_T} \right] \quad (2.17)$$

to:

$$2C \frac{dV_n}{dt} = -I_c \left[\tanh \left(\frac{V_n}{2V_T} + \beta_n \right) - \tanh \left(\frac{V_{n-1}}{2V_T} + \beta_{n-1} \right) \right] \quad (2.18)$$

Here again, the presence of the shift coefficients β_n introduces even-order harmonics in the stage response.

2.4 Summary

The identification of nonlinearities from the characteristics of electronic components in the main processing unit of the effect can be extracted from the circuit diagrams of examples presented in this section. However, as shown in the last part, this analysis may be insufficient to explain all the distortion measured in the output signal.

The experiments that we report in the following section were designed to quantify nonlinearities in the available systems and, when possible, identify their sources.

Chapter 3

Experimental study

To study the nonlinearities in the behaviour of analog circuits, we made measurements on devices available in the Sound Processing and Control Laboratory (Figs. 3.1 and 3.2). In each one of them, we examined the influence of one specific parameter keeping the other parameters fixed.



Fig. 3.1 Experimental benchmark (1)

Unless stated otherwise, we assume that the input signal is a sound file sampled at 96kHz and coded with 24 bits and that the output measurements have the same characteristics.



Fig. 3.2 Experimental benchmark (2)

3.1 Remarks

Aliasing In this thesis, we are not interested in the influence of aliasing in the analog-to-digital conversion on the accuracy of the system modelling. Since the Nyquist frequency of our measurements is 48kHz and that more than 5 to 7 significant orders of nonlinearities in our systems are not expected, we will limit the range of the fundamental frequency of harmonic signals (e.g., sinusoids, chirps) to a maximum of 10kHz.

Audio range As electronic systems, the synthesizers' effects have a specific behaviour at any given frequency. However, these systems were designed and optimized to work with a target behaviour in the audio and/or audible frequency range. Thus, we do not examine the system response for frequencies below 20Hz.

Fundamental frequency range We limit our tests to fundamental frequencies in the range **50Hz–10kHz**. It roughly corresponds to the range of first interest for music purposes. Future work on the system could look at frequencies below and above this range to study its behaviour on the whole audio range.

AC power source We observed the common influence of the AC power source on the measured signals. This influence is visible as harmonic peaks related to the fundamental frequency at 60Hz. This signal is much lower in terms of amplitude than the main com-

ponent of the signals measured, however, it can be comparable to some of the harmonic distortion components.

3.2 Experiments on lowpass filters

Since we had access to the circuit board of the Moog 904A lowpass filter, we had the opportunity to perform measurements both at the outlets and directly on the board of that filter. These two setups are presented here.

3.2.1 Setup for measurements at the outlets

The setup for input/output measurements at the outlets of the filter follows the scheme displayed on Fig. 3.3.

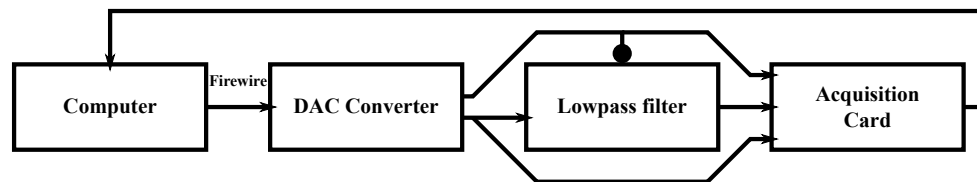


Fig. 3.3 Experimental setup for measurements at the outlets for lowpass filters

Signal generator The signal source used for our experiments is a computer generating a digital signal sampled at 96kHz and coded with 24 bits. This choice allows us to generate customized signals according to experimental needs. The signals generated through the computer has also been observed in our experiments as superior in quality to signals generated by an Agilent 33220A analog signal generators. For example, swept-sine signals produced by the analog generator contained harmonic components even though at a very weak power (-90dB). These components were not present in the output of the computer generated signal and they could interfere with our study of filter harmonic distortion.

Digital-to-analog conversion The digital signal generated by the computer is transmitted through a FireWire connection and then converted into an analog signal using a MOTU

828 as Digital-to-Analog Converter (DAC). This device is equipped with four outlets with a 0dB reference at about 4.5V.

Acquisition The acquisition of analog signals is done using a National Instruments NI-4472 card connected on a PCI bus to a computer equipped with Windows XP and Labview SignalExpress 2010. This card allows us to measure 8 simultaneous inputs at a sample rate of 96kHz in the range $\pm 10V$ and coded with 24 bits.

Control signal To generate the control signal, we use a combination of a digital computer-generated signal converted by the MOTU and a DC power source. Each of them is connected to a different control outlet of a device if possible (e.g., Moog 904A), or added before using the analog adder of a Korg MS-50. The control signal is most of the time recorded simultaneously to the other signals.

3.2.2 Setup for measurements on the circuit board

In case of measurements made directly on the circuit, we use oscilloscope probes that we plug directly to the circuit, following the scheme displayed on Fig. 3.4.

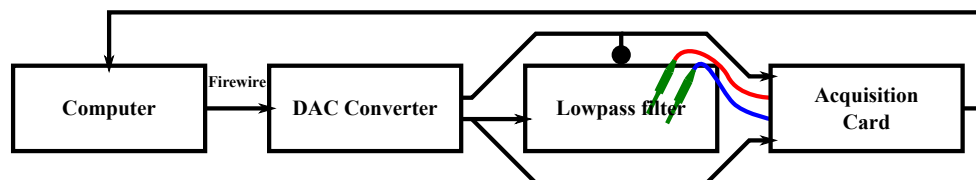


Fig. 3.4 Experimental setup for measurements on the circuit board for low-pass filters

On-board measurements The probe signals are acquired directly by the acquisition card described in the previous section.

3.2.3 Cutoff frequency extraction

To extract the cutoff frequency of filters we set the filter with maximal resonance to improve cutoff localization and then send a swept-sine signal to it. We then perform a spectrogram

analysis on the input and the output signals using a Blackman window of length 8192. From the input spectrogram, we locate the instantaneous frequency of the signal and we extract the magnitude of that component using a quadratic interpolation on the three adjacent bins around the spectrogram magnitude peak for each window. From the output spectrogram, we extract the magnitude of the same component. From this, we get a frequency response curve, the maximum of which gives us the cutoff frequency.

3.2.4 Distortion measurement

The extraction of the power of the distortion harmonics of the signal is also performed using quadratic interpolation around the peaks of the spectrogram. The power magnitude of the main component is then subtracted to get the relative magnitude of each order of distortion for each window.

3.3 Moog filter

3.3.1 Input-output behaviour for a DC input

Context In the case of a linear system, the presence of a DC component in the input is usually not a concern since this component will be processed independently of the other components of the signal and can be ignored or removed in a post-processing stage.

This observation does not apply in the case of a nonlinear system. It can even become critical in particular cases, such as the common example of a system with only nonlinearities of an odd order. If we take the example of a system where the output y is expressed as a function of the input x with the relation $y = x + x^3$, we can observe that this system should have only two output components at frequencies f and $3f$ when submitted to sinusoidal input at frequency f . However, the presence of a DC component α (e.g., different ground voltage levels) will result in the following output:

$$\begin{aligned} y(t) &= (x + \alpha) + (x + \alpha)^3 \\ &= \alpha + \alpha^3 + (3\alpha^2 + 1)x + 3\alpha x^2 + x^3 \end{aligned} \tag{3.1}$$

We see that this DC component would affect the intensity of the output component at frequency f creating an even-order component at $2f$.

The purpose of the following experiment is to study how DC components are processed by the filter and in particular if they are filtered either by the input buffer stage, the output buffer stage, or even both.

Experiment For this experiment, we sent a series of DC components of various voltages as input to the Moog filter. The resonance parameter of the filter was set to its minimum to avoid self-oscillation effects during the experiment. The voltages were measured both on the board, both at the input of the filter stage (see Appendix B.1.1) and at the output of the filter. The different set-ups are summarized in Appendix C on Tables C.1 and C.2.

To estimate the DC voltages from the measurements, we take the mean of the signal. The measurement noise is modelled as zero-mean Gaussian noise. Its power is estimated from the empirical standard deviation σ of the signal.

Results and discussion The measurements corresponding to the first experiments are displayed in Fig. 3.5. As we can see, the DC voltage at the input is transmitted to the input of the filter stage. The voltage at the base pin of the transistors Q7 and Q8 (see Fig. 3.5(a)) changes linearly with the DC voltage following the relations extracted by linear regression:

$$V_{Q7} = -13.01 \times 10^{-3} V_{in} + 3.5613 \quad 1 - R^2 < 0.01\% \quad (3.2)$$

$$V_{Q8} = 7.396 \times 10^{-3} V_{in} + 3.5595 \quad 1 - R^2 < 0.01\% \quad (3.3)$$

The differential voltage (see Fig. 3.5(b)) is thus given by:

$$V = -20.41 \times 10^{-3} V_{in} + 1.808 \times 10^{-3} \quad 1 - R^2 < 0.01\% \quad (3.4)$$

The measurements showed that the input signal of the filtering stage contains very low noise with $\sigma = 0.1\text{mV}$. One interesting observation is that *for a zero-input signal*, the differential voltage at *the input of the filtering stage has a DC component*.

Concerning the output signal (see Fig. 3.5(c)), we see that the DC component is completely filtered since the output voltage is flat and presents a very small constant DC value ($\sim 0.04\text{mV}$). This is likely introduced by the measuring equipment. The measurement noise is slightly higher than in the on-board measurement going up to $\sigma = 0.6\text{mV}$.

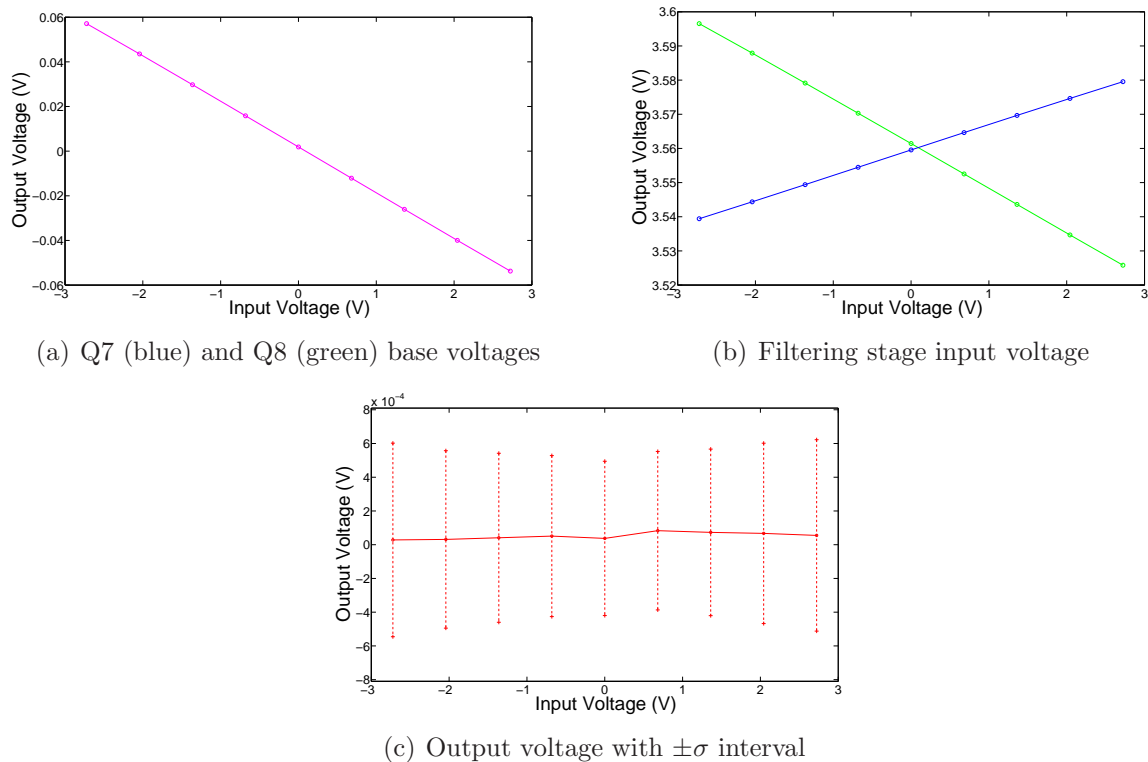


Fig. 3.5 Moog filter — Measured voltages in the case of a DC input

To confirm this observation, we conducted further experiments that examined the addition of a sinusoidal component to the input signal (Experiment 10-18). The results of these experiments are identical to those presented earlier since the signal at the input of the filtering stage was containing the sum of the attenuated input sinusoid and the offset found in the first experiments. Thus, we conclude that the signal transmitted at the input of the filtering stage is influenced by the presence of a DC component and that this component has to be eliminated later.

3.3.2 Cutoff frequency control

Context According to Moog's documentation, the control of the cutoff frequency of the filter is controlled exponentially through the control voltage such that an increment of 1V produces an increment of 1 octave on the cutoff frequency (see Appendix B.1.1). He also states that the 3 different frequency range positions shift the cutoff frequency range by 2 octaves (so the equivalent of 2V). Yet, Moog does not specify the starting value of the

cutoff frequency scale, so we cannot say what frequency would give a particular control voltage.

The purpose of the following experiment is, first, to measure the actual output voltage of the digital-to-analog converter for a given digital amplitude in the audio file containing the constant control signal and second, to verify the exponential relationship given by Moog and to parametrize the starting value for later experiments.

Experiment For this experiment, we sent as input in the Moog filter a series of identical swept sine signals. Each time, the control voltage was changed with a given increment. The resonance parameter of the filter was set to its maximum to improve the localization of the frequency response peak of the filter. The voltage was measured at the output of the filter. The different set-ups are summarized in Appendix C on Tables C.3 and C.4.

We perform measurements for 2 different positions of the frequency range switch (2nd and 3rd positions), but we add the corresponding voltage offset (2V) to the control voltage so that the filter cutoff frequency is theoretically the same according the filter documentation.

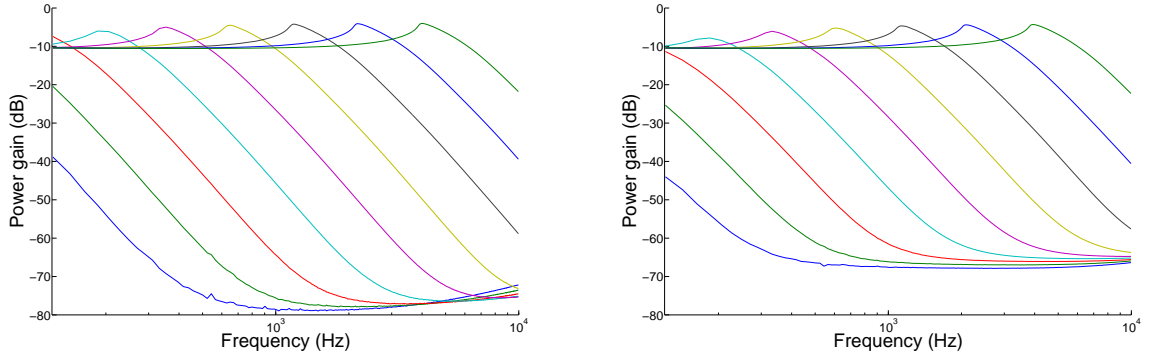
Results and discussion The estimated control voltage sent by the computer through the MOTU is given in Table 3.1. The estimated magnitude response curves are given in Fig. 3.6. We see that for the 3 first experiments, the cutoff frequency is not in the span of the swept-sine signal so we cannot extract it from our measurements.

Exp n°	19	20	21	22	23	24	25	26	27
Digital ampl.	-0.8	-0.6	-0.4	-0.2	0	0.2	0.4	0.6	0.8
Voltage (V)	-3.617	-2.713	-1.809	-0.905	-0.001	0.903	1.806	2.710	3.614

Table 3.1 Measurement of the control voltage coming from the DAC as a function of the amplitude in the control audio file

According to the filter documentation, the relationship between the control voltage and the frequency cutoff is exponential. Thus we perform a linear regression (see Fig. 3.7 on the logarithm of the estimated cutoff frequency as a function of the measured control voltage. From this, we observe that for the 2nd frequency range position:

$$\log_2(f_c) = 0.9769V_{\text{ctrl}} + 9.422 \quad 1 - R^2 < 0.1\% \quad (3.5)$$

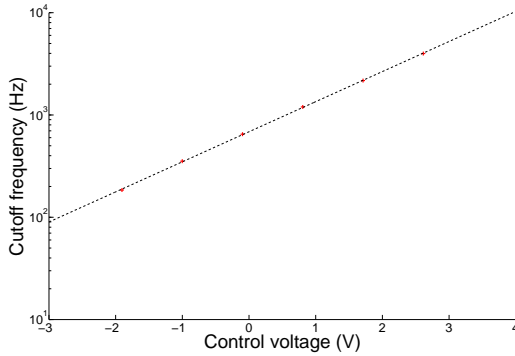


(a) 2nd frequency range position — Exp. 19 (left) to Exp. 27 (right) (b) 3rd frequency range position — Exp. 28 (left) to Exp. 36 (right)

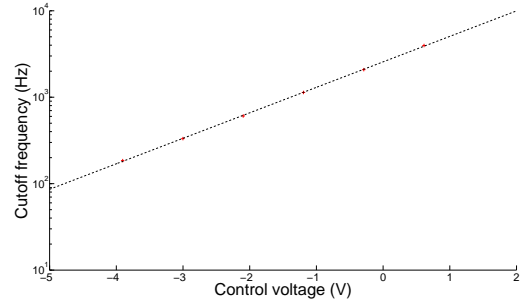
Fig. 3.6 Moog filter — Magnitude response of the filter for different control voltage values

and for the 3rd one:

$$\log_2(f_c) = 0.9793V_{\text{ctrl}} + 11.325 \quad 1 - R^2 < 0.1\% \quad (3.6)$$



(a) 2nd frequency range position



(b) 3rd frequency range position

Fig. 3.7 Moog filter — Cutoff frequency as function of the control voltage

As stated by the documentation, the slope of the relationship between the control voltage and the logarithm of the cutoff frequency is about 1V per octave. The gap between the two curves is 1.903V. If we consider the two extreme control voltages given by the documentation (-9V~6V), we get the cutoff frequency range given in Table 3.2.

The results also show that the filter gain is similar for both frequency range positions

Position	2	3
Minimal cutoff frequency	1.547Hz	5.699Hz
Maximal cutoff frequency	39.87kHz	150.6kHz

Table 3.2 Estimated frequency range values for the range switch

(\sim -10dB) at low frequencies while they are different at high frequencies (\sim -75dB for 2nd one, \sim -65dB for 3rd one).

3.3.3 Harmonic distortion of the Moog filter

As a preliminary experiment, we looked at the results of experiment 42 to observe the nonlinearities in the output signal spectrogram. The input and output signal spectrograms are displayed in Figs. 3.8 and 3.9.

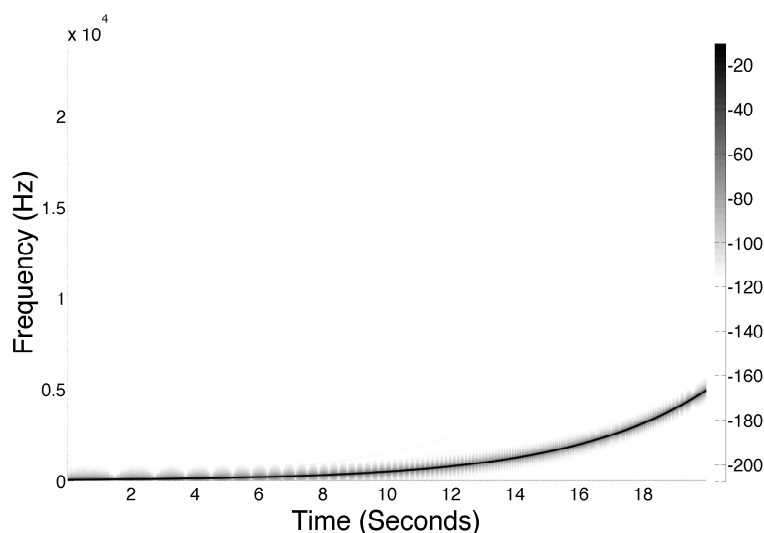


Fig. 3.8 Moog filter — Input signal spectrogram of the experiment 42

As can be seen on the output signal spectrogram, harmonic distortions of orders up to 7 are clearly visible. We also see that the magnitude of the distortion harmonics varies with the instantaneous frequency of the input signal.

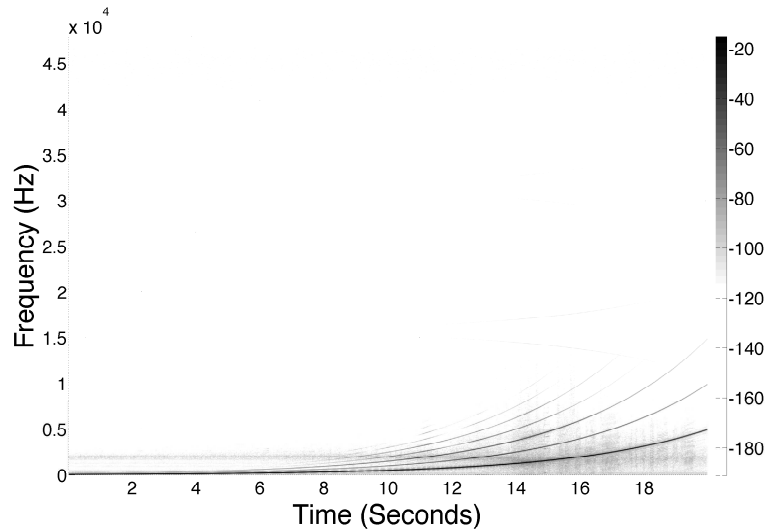


Fig. 3.9 Moog filter — Output signal spectrogram of the experiment 42

3.3.4 Influence of the frequency cutoff setting on the filter harmonic distortion

Context The filter response could be seen as subject to two contradictory behaviours when submitted to a single-component signal. On the one hand, the nonlinearities of the filter create harmonics in the signal. On the other hand, the linear behaviour of the filter is such that the original component but also its harmonics created by distortion will be filtered when going through each stage of the ladder filter, thus reducing the distortion effect since these harmonics are situated closer to or above the cutoff frequency of the filter.

The purpose of this experiment is to study this phenomenon and to quantify it.

Experiment For this study we use the same measurements we made in Section 3.3.2. We measure the distortion up to order 7 from the spectrogram analysis of the output signal.

Results and discussion On a single experiment, we can see the difference in the harmonic distortion depending on the relative location of the component of the signal and the cutoff frequency of the filter. If we look at Fig. 3.10 where there is no resonance, we can see that there is a similar behaviour between pairs of distortion (2nd and 3rd, 4th and 5th,...). For low frequencies, the odd-order distortion is the strongest, while for high frequencies, the even-order one becomes dominant. Also, if we consider that an audible component has to

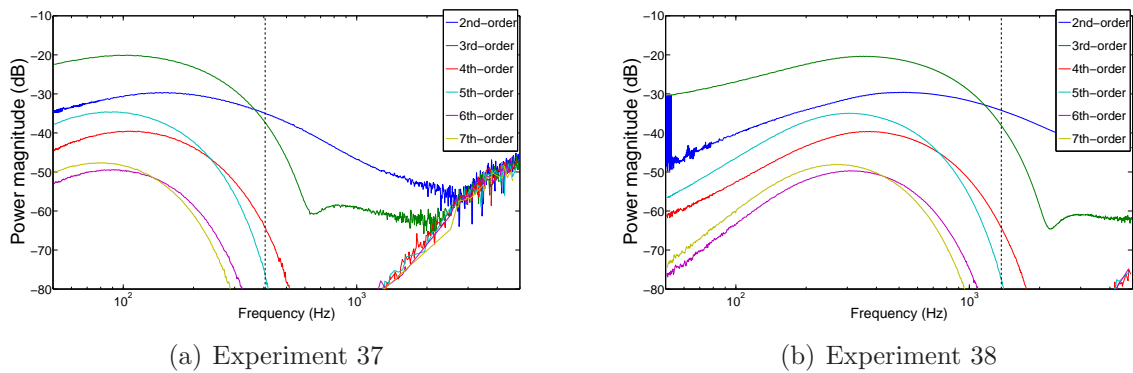


Fig. 3.10 Moog filter — Relative magnitude of the distortion orders at resonance 0 (the cutoff frequency is displayed with a black vertical line)

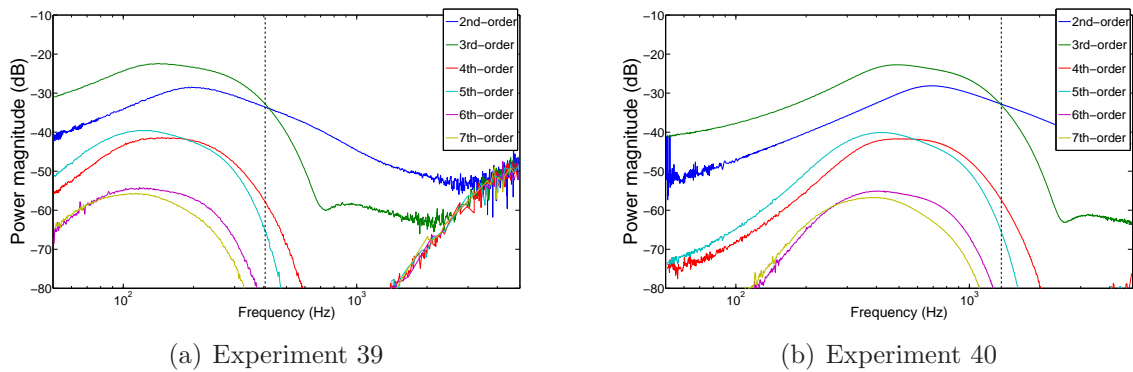


Fig. 3.11 Moog filter — Relative magnitude of the distortion orders at resonance ~ 7 (the cutoff frequency is displayed with a black vertical line)

be above a relative power magnitude of -60dB we see that the sound is richer around $f_c/4$ with 7 audible components, while at high frequencies, the sound contains only 3 audible components.

If we look at the curves for different frequency cutoff settings (Figs. 3.10(a) and 3.10(b)), we see that on the logarithmic frequency scale the distortion patterns are translated along with the cutoff frequency. Thus, up to a point, the behaviour of the system seems to be independent of that setting.

With an intermediate resonance (Fig. 3.11), the distortion patterns are very similar to the experiments without resonance, with only minor differences. Thus the behaviour of the system seems more or less invariant by translation when changing the cutoff frequency on the logarithmic frequency scale.

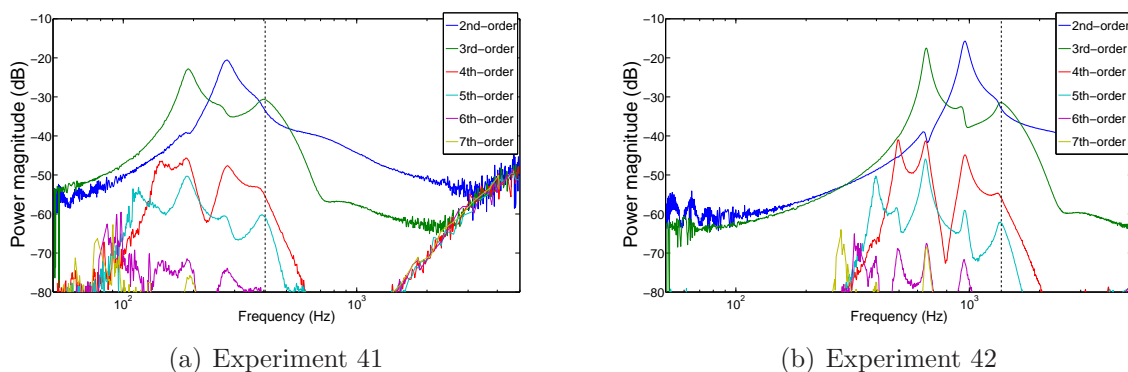


Fig. 3.12 Moog filter — Relative magnitude of the distortion orders at resonance 10 (the cutoff frequency is displayed with a black vertical line)

Finally, if we look at the filter behaviour with maximal resonance (Fig. 3.12) we see that the distortion pattern is much more complex with large variations of the components depending on the relative location of the component of the signal and the cutoff frequency of the filter. With this amount of resonance, analog filters are well-known for showing a phenomenon called *self-oscillation*, which means that due to the narrow-band strong amplification around the cutoff frequency, the filter will generate a self-amplified component at that frequency from very small perturbations (e.g., electronic noise). Here it seems that each distortion curve displays peaks when the frequency of the distortion order (nf) or one of its subharmonics (coming either from the input component f or one of its lower distortion order mf with $m < n$) falls in the resonance region. However, this general rule does not explain all the variations of the curves, and it is difficult to extract tendencies from the distortion of order greater than 3.

The previous remark about the translation invariance of the curves seems to apply here too, but we see that the curve evolution is much sharper for high cutoff frequencies (Fig. 3.12(b)) than for low ones (Fig. 3.12(a)).

3.3.5 Influence of the input amplitude on the filter harmonic distortion

Context Nonlinearities are usually very significantly influenced by the amplitude of the input. If we think about a simple saturation effect such as $y(t) = \tanh(x(t))$, the distortion at the different orders (see Table 3.3) varies visibly. The presence of the hyperbolic tangent function in the equations of the Moog filter (see Eq. (2.2)) implies that a similar

phenomenon will arise in this system.

Input ampl.	1st order	3rd order	5th order	7th order
0.01	10.0e-3 <i>0dB</i>	83.3e-9 <i>-102dB</i>	0.833e-12 <i>-202dB</i>	7.79e-18 <i>-302dB</i>
0.1	0.100 <i>0dB</i>	0.829e-3 <i>-62dB</i>	0.827e-6 <i>-122dB</i>	0.835e-9 <i>-182dB</i>
1	0.812 <i>0dB</i>	54.2e-3 <i>-24dB</i>	4.52e-3 <i>-45dB</i>	0.382e-3 <i>-67dB</i>

Table 3.3 Amplitudes and relative magnitudes of odd-order distortion of a nonlinear system $y(t) = \tanh(x(t))$

The purpose of this experiment is to observe this distortion effect and to quantify it.

Experiment For this experiment (Experiment 43), we sent a series of sinusoidal signals as input in the Moog filter. These signals had an amplitude that varied exponentially. The sinusoids had different frequencies below and above the cutoff frequency of the filter. The set-up is summarized on Tables C.5 and C.6.

The voltages were measured at the input, at the output, at the input of the filter stage, and at the computer-driven control input.

Results and discussion As expected, we observe an increasing distortion in the output the signal while the amplitude of the signal is rising. Furthermore, this increase seems to be linearly dependent on the gain of the input signal (in the log-log scale).

As we observed in the experiments of Section 3.3.4, it seems to be separate tendencies for even and odd-order distortions, the latter increase more than the former

3.4 Experiments on ring modulators

The setup for input/output measurements on the ring modulators follows the scheme displayed in Fig. 3.14.

The equipment used is mostly similar to the one already detailed in Section 3.2 for the experiments on the lowpass filters. The main change is that the control channel is

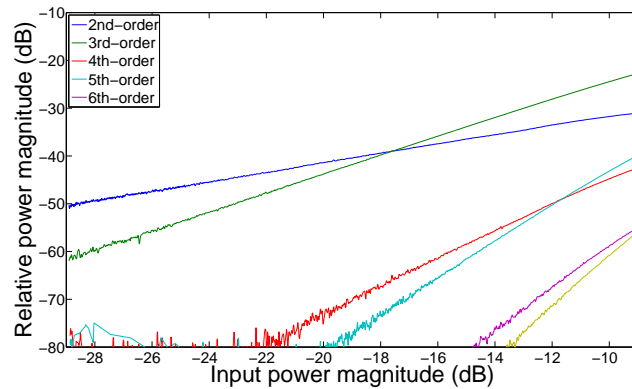


Fig. 3.13 Moog 904A — Variation of the distortion orders for different input amplitudes

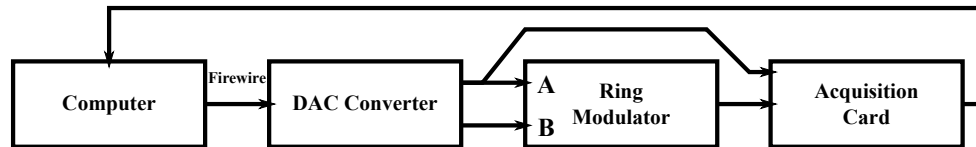


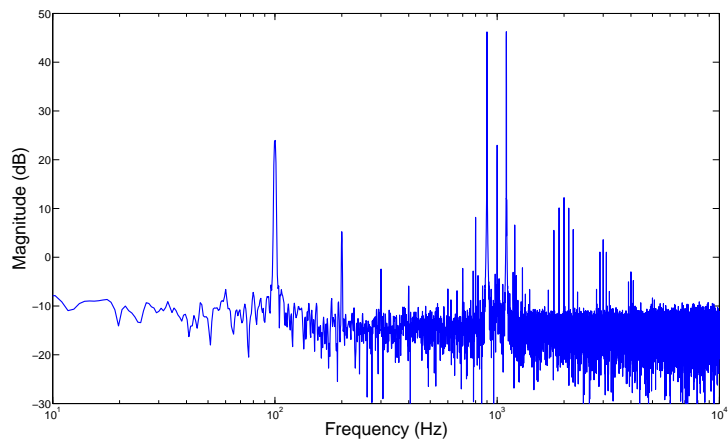
Fig. 3.14 Experimental setup for measurements at the outlets for ring modulators

replaced by the second input channel. The limited number of outputs in the digital-to-analog converter does not allow us to record this second input yet, since we perform symmetrical experiments, we will assume that the signal measured on the first input channel corresponds to the one on the second one.

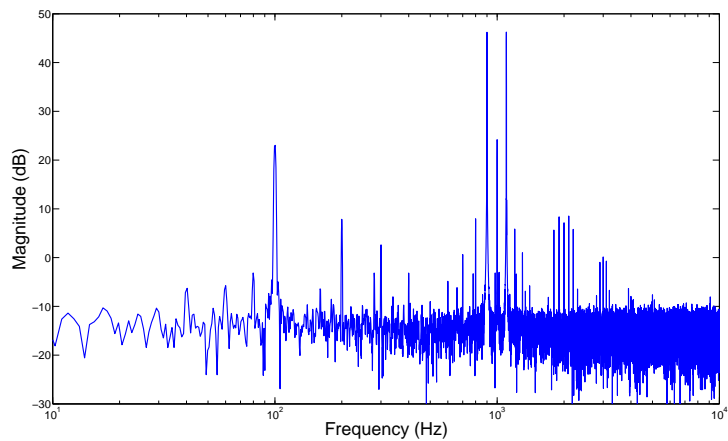
3.5 Korg MS-50 ring modulator

In this section, we reproduce the experiment of Hoffmann-Burchardi (see Section 2.3.1) on the Korg ring modulator. We send sinusoidal signals at 100Hz and 1kHz to the Audio and Carrier inputs of the effect (Experiment 45, see Tables 3.4 and 3.5). In a second experiment, we swap the two input signals to test the asymmetry between the two inputs (Experiment 46).

First Experiment We extracted the spectrum of the output signal (windowed using a Blackman window). This spectrum is displayed in Fig. 3.15(a). As we can see the number of peaks is much larger than it should be in the case of an ideal multiplier (see Section 2.3).



(a) 1st Experiment



(b) 2nd Experiment

Fig. 3.15 Korg ring modulator — Output signal spectrum

We see that, similar to the Hoffmann-Burchardi experiment, the input signal frequencies are significant as well as numerous distortion peaks.

Second Experiment After swaping of the inputs, we extracted the spectrum of the output signal. This spectrum is displayed in Fig. 3.15(b).

Frequency (Hz)	Relative power magnitude
1100 $f_m + f_c$	0.0dB
900 $f_m - f_c$	-0.0dB
1000 f_c	-22.1dB
100 f_m	-23.2dB

Table 3.4 Korg ring modulator — Strongest peaks in the output signal spectrum (1st experiment)

The peaks above -30dB are given in Table 3.5.

Frequency (Hz)	Relative power magnitude
1100 $f_m + f_c$	0.0dB
900 $f_m - f_c$	-0.0dB
100 f_c	-22.3dB
1000 f_m	-23.3dB

Table 3.5 Korg ring modulator — Strongest peaks in the output signal spectrum (2nd Experiment)

We can see that the order of the strongest peaks is not affected by the inversion and the distortion of these peaks is very similar in both experiments (see Table C.9). However, the distortion pattern is slightly different demonstrating that the two inputs are not symmetrical. This is expected since the effect circuitry is not symmetrical.

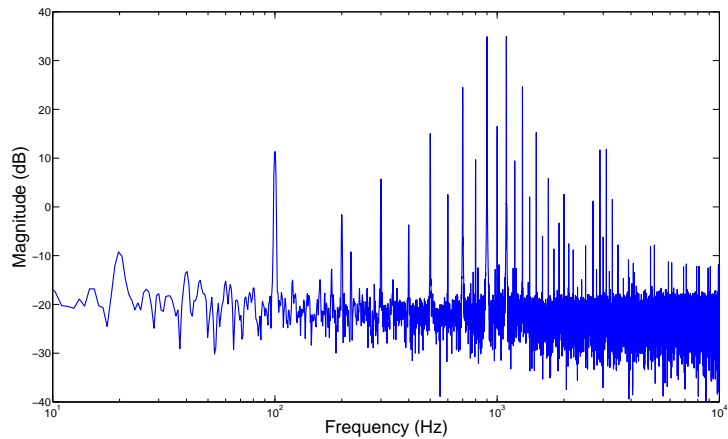
Frequency	Magnitude (Exp. 1)	Magnitude (Exp. 2)
$f_m + f_c$	46.3dB	46.3dB
$f_m - f_c$	46.2dB	46.2dB
f_c	24.0dB	24.2dB
f_m	23.0dB	23.0dB

Table 3.6 Comparison of the two output signal spectra of the Korg

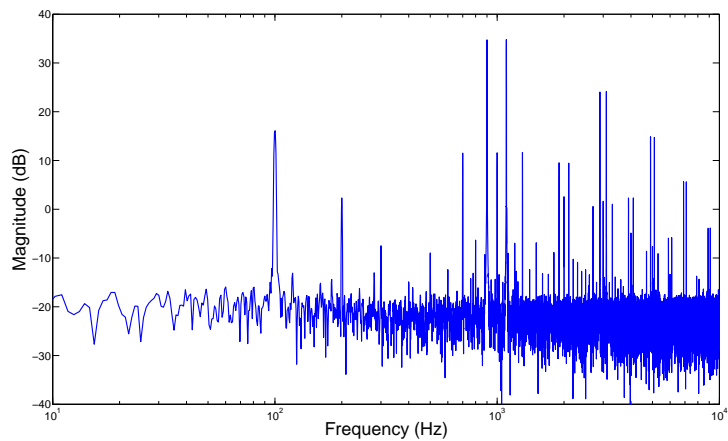
3.6 Moogerfooger ring modulator

We reproduce the same experiment on the Moogerfooger ring modulator. We sent sinusoidal signals at 100Hz and 1kHz to the Audio and Carrier inputs of the effect (Experiment 47, see Table C.10). In a second experiment, we swap the two input signals to test the asymmetry between the two inputs (Experiment 48).

First Experiment We extracted the spectrum of the output signal (windowed using a Blackman window). This spectrum is displayed in Fig. 3.16(a). As we can see, the number of peaks is much larger than it should be in the case of an ideal multiplier.



(a) 1st Experiment



(b) 2nd Experiment

Fig. 3.16 MF-102 ring modulator — Output signal spectrum

The peaks above -30dB are given in Table 3.8. The power difference between the 1st and the 14th peaks is 29dB. We observe the presence of mostly odd-order distortion as we would expect from such circuit.

Frequency (Hz)	Relative power magnitude
1100 $f_m + f_c$	0.0dB
900 $f_m - f_c$	-0.0dB
1300 $f_m + 3f_c$	-10.3dB
700 $f_m - 3f_c$	-10.4dB
1000 f_m	-18.5dB
1500 $f_m + 5f_c$	-19.7dB
500 $f_m - 5f_c$	-19.9dB
3100 $3f_m + f_c$	-23.1dB
2900 $3f_m - f_c$	-23.3dB
100 f_c	-23.6dB
800 $f_m - 2f_c$	-25.3dB
1200 $f_m + 2f_c$	-25.5dB
1700 $f_m + 7f_c$	-29.1dB
300 $f_m - 7f_c$	-29.2dB

Table 3.7 MF-102 ring modulator — Strongest peaks in the output signal spectrum (1st Experiment)

Second Experiment After swaping of the inputs we extracted the spectrum of the output signal. This spectrum is displayed in Fig. 3.16(b).

The peaks above -30dB are given in Table 3.8. The magnitude difference between the 1st and the 14th peaks is again of 29dB. Again, we see that the effect is not symmetrical.

Again, the order of the strongest peaks is not affected by the inversion and the distortion of these peaks is very similar in both experiments (see Table 3.9). However, the distortion pattern is slightly different, which demonstrates that for the Moogerfooger the two inputs are not symmetrical.

Discussion

In the four experiments on ring modulators, we observed results corresponding to the experiments of Hoffmann-Burchardi. The spectral output is much richer than for an ideal multiplier and, in the case of the Korg, most of these peaks were inaudible. Increasing the input amplitudes and the distortion could bring several additional components to the resulting sound.

Another result we have from these measurements is the contrast between the nonlinearities of the Moogerfooger and the Korg. One could expect the Korg, a much older design, to have a stronger distortion. But the experiments show that the modern MF-102 produces a richer sound with numerous audible distortion peaks.

Frequency (Hz)	Relative magnitude
1100 $f_m + f_c$	0.0dB
900 $f_m - f_c$	-0.0dB
3100 $f_m + 3f_c$	-10.6dB
2900 $f_m - 3f_c$	-10.7dB
100 f_m	-18.7dB
4900 $f_m + 5f_c$	-20.0dB
5100 $f_m - 5f_c$	-20.1dB
1300 $3f_m + f_c$	-23.2dB
700 $3f_m - f_c$	-23.3dB
1000 f_c	-23.2dB
1900 $f_m - 2f_c$	-25.3dB
2100 $f_m + 2f_c$	-25.3dB
6900 $f_m + 7f_c$	-29.2dB
7100 $f_m - 7f_c$	-29.2dB

Table 3.8 MF-102 ring modulator — Strongest peaks in the output signal spectrum

Frequency	Power magnitude (Exp. 1)	Power magnitude (Exp. 2)
$f_m + f_c$	35.0dB	34.8dB
$f_m - f_c$	34.9dB	34.7dB
$f_m + 3f_c$	24.6dB	24.2dB
$f_m - 3f_c$	24.5dB	24.0dB
f_m	16.5dB	16.1dB
$f_m + 5f_c$	15.2dB	14.8dB
$f_m - 5f_c$	15.0dB	14.7dB
$3f_m + f_c$	11.8dB	11.6dB
$3f_m - f_c$	11.7dB	11.5dB
f_c	11.3dB	11.6dB
$f_m - 2f_c$	9.7dB	9.5dB
$f_m + 2f_c$	9.4dB	9.4dB
$f_m + 7f_c$	5.8dB	5.6dB
$f_m - 7f_c$	5.7dB	5.6dB

Table 3.9 Comparison of the two output signal spectra of the MF-102

Finally, we saw that both systems are not symmetric and the choice of which signal will be the carrier or the modulator changes the system response. This was to be expected since the electronic designs are not symmetric either relatively to the inputs.

3.7 Summary

The results of our experiments show the complexity of the influence of the various parameters available to control the effects on their nonlinear behaviour. In the case of the filter, there are opportunities to add a very particular colouration to the output signal by choosing a given set of parameters. We observed that the sound spectrum characteristics vary greatly depending on its frequency adding a new complex control dimension.

The second remark that we can make on these results is that, as reported by Hoffmann-Burchardi (see Section 2.3), the contribution of the input and output circuitry of the effects has to be taken into account to fully identify the sources of distortion. The introduction of a relatively large DC component in the input signal of the filtering stage certainly influences the characteristics of the outgoing sound.

In the following chapters, we will evaluate the ability of nonlinear modelling techniques to integrate these observations and accurately reproduce the sound characteristics of the devices.

Chapter 4

Nonlinear modelling using black-box approach

As mentioned in the introduction, research into nonlinear modelling tools has been ongoing since the 1950's. A large number of approaches have been explored, with the derivation of models adapted to a set of objectives in terms of, for example, complexity, accuracy or adequacy. A large class of models obeys to the black-box approach what consists in building a model without any prior information on the system underlying structure. In this case, the objective is to fit the system response as close as possible.

4.1 Linear theory

Linear systems are systems whose functional is characterized by two properties:

- Additivity: $F[X + Y](t) = F[X](t) + F[Y](t)$
- Scalability: $F[\lambda X](t) = \lambda F[X](t)$

The theory of such systems has been thoroughly explored during the last century and numerous references can be found to have a complete overview of this class of systems (Oppenheim et al. 1999).

Non-parametric representation Linear time-invariant (LTI) systems have the well-known property of being completely characterized in the time domain by their *impulse*

response $h(t)$, which is defined as the response of the system to a *Dirac impulse* $\delta(t)$.

$$h(t) = F[\delta](t) \quad (4.1)$$

Alternatively, it can be characterized in the frequency domain with the Fourier transform of the impulse response $H(j\omega)$:

$$H(j\omega) = \mathcal{FT}(F[\delta](t)) \quad (4.2)$$

Then, the output $y(t)$ of the system when excited by a signal $x(t)$ can be expressed in the time-domain by the convolution:

$$y(t) = (h * x)(t) = \int_{-\infty}^{+\infty} h(\tau)x(t - \tau)d\tau \quad (4.3)$$

and in the frequency domain by the multiplication:

$$Y(j\omega) = H(j\omega)X(j\omega) \quad (4.4)$$

The property of causality is verified if and only if $\forall t < 0, h(t) = 0$. The stability is verified when the impulse response verifies $\int_{-\infty}^{+\infty} |h(t)|dt < \infty$.

Continuous-time parametric model LTI systems can be represented as well using differential equations of the form (Westwick and Kearney 2003):

$$\frac{d^l y}{dt^l}(t) + a_{l-1} \frac{d^{l-1} y}{dt^{l-1}}(t) + \dots + a_0 y(t) = b_m \frac{d^m x}{dt^m}(t) + \dots + b_0 x(t) \quad (4.5)$$

where $l \leq m$ to have a causal system.

Using the Laplace transform, this relation becomes:

$$(s^l + a_{l+1}s^{l-1} + \dots + a_0) Y(s) = (b_m s^m + \dots + b_0) X(s) \quad (4.6)$$

This equation gives us the Laplace transform of the impulse response of such system, given by:

$$H(s) = \frac{Y(s)}{X(s)} = \frac{b_m s^m + \dots + b_0}{s^l + a_{l+1}s^{l-1} + \dots + a_0} = \frac{B(s)}{A(s)} \quad (4.7)$$

Then, the system can also be characterized by the roots of the polynomials B (zeros of the system) and A (poles of the system).

Discrete-time parametric model By analogy to the case of continuous-time (Eq. (4.6)), we can model a discrete-time system using the backward discrete shift operator z^{-1} , which is such that $z^{-1}x[n] = x[n-1]$. The system is described by the discrete difference equation:

$$A(z^{-1})y[n] = B(z^{-1})x[n] \quad (4.8)$$

The transformation from continuous to discrete time is achieved using different techniques such as bilinear transform and the impulse invariant transform.

Modelling the measured output $u[n]$ of the system by adding a white noise component $w[n]$ to the Eq. (4.8) gives the relation:

$$u[n] = \frac{B(z^{-1})}{A(z^{-1})}x[n] + w[n] \quad (4.9)$$

The model is often referred to as an auto-regressive moving average (ARMA) model.

4.2 Volterra series

4.2.1 SISO model

The Volterra series is a well-known example of kernel-based model in the literature on nonlinear modelling. First nonlinear modelling approaches were derived from the work of Vito Volterra in 1887. He studied analytic functionals and proved that they could be described using the expansion:

$$y(t) = F[x](t) = \sum_{m=0}^{+\infty} F_m[x](t) \quad (4.10)$$

where F_m are functionals defined as:

$$\begin{aligned}
F_0[x](t) &= h_0 \\
F_m[x](t) &= \int_{\tau_1} \cdots \int_{\tau_m} h_m(\tau_1, \dots, \tau_m) x(t - \tau_1) \cdots x(t - \tau_m) d\tau_1 \cdots d\tau_m \quad m > 0
\end{aligned} \tag{4.11}$$

$h_m : (\tau_1, \dots, \tau_m) \mapsto h_m(\tau_1, \dots, \tau_m)$ is a m -variable function called m th-order *Volterra kernel*. These expansion is usually denoted as *Volterra series* or *expansion* in the literature.

We can see this expansion as:

- A generalization of the description of linear systems using their impulse response h :

$$y(t) = F[x](t) = \int_{\tau} h(\tau) x(t - \tau) d\tau \tag{4.12}$$

- The introduction of the idea of memory in the Taylor expansion;

$$y(t) = F[x](t) = \sum_{m=0}^{\infty} h_m x^m(t) \tag{4.13}$$

To get a more general expression working for both discrete-time and continuous-time functionals, we can rewrite the expression of the kernels:

$$\begin{aligned}
F_0[x] &= h_0 \\
F_m[x] &= ((h_m *_{\tau_1} x) \cdots *_{\tau_m} x) \quad m > 0
\end{aligned} \tag{4.14}$$

where $*_a$ is the convolution corresponding the variable a . For example, in the case of 2-variable functions, the a -convolution would be defined as:

$$\begin{aligned}
f(b, X) &= g *_a h = \int_a g(a, X) h(b - a, X) da \quad \text{in continuous time} \\
f[b, X] &= g *_a h = \sum_a g[a, X] h[b - a, X] \quad \text{in discrete time}
\end{aligned} \tag{4.15}$$

This expansion describes a decomposition of the nonlinearities of the SISO system on an infinite polynomial basis. Different expressions of this expansion were studied, in

particular by Wiener (Wiener 1958), using different orthogonal polynomial basis for the system description. The truncated Volterra series describe the system as a superposition of one linear, one bilinear, ..., and one m -linear system(s).

4.2.2 Laplace transform and Z-transform of the expansion

Laplace transform: If we extend the definition of the Laplace transform to the multi-dimensional functions, we can define it as:

$$H_m(s_1, \dots, s_m) = \int_0^{+\infty} \dots \int_0^{+\infty} h_m(t_1, \dots, t_m) e^{-s_1 t_1} \dots e^{-s_m t_m} dt_1 \dots dt_m \quad (4.16)$$

Thus, in the case of the continuous-time expansion truncated at order M , its Laplace transform is written as:

$$Y(s_1, \dots, s_M) = \sum_{m=0}^M H_m(s_1, \dots, s_m) X(s_1) \dots X(s_m) \quad (4.17)$$

Laplace transform: The equivalent formulation for the discrete-time expansion is given by generalizing the Z-transform:

$$H_m(z_1, \dots, z_m) = \sum_{k_1, \dots, k_m=0}^{+\infty} h_m[k_1, \dots, k_m] z_1^{-k_1} \dots z_m^{-k_m} \quad (4.18)$$

For an expansion truncated at order M , its Z-transform is written as:

$$Y(z_1, \dots, z_M) = \sum_{m=0}^M H_m(z_1, \dots, z_m) X(z_1) \dots X(z_m) \quad (4.19)$$

4.2.3 MISO model

The expansion can directly be generalized in the case of k multiple inputs, introducing polynomial terms for each input as well as cross-terms:

$$y(t) = \sum_{m_1=0}^{+\infty} \dots \sum_{m_k=0}^{+\infty} F_{m_1, \dots, m_k}[x](t) \quad (4.20)$$

with

$$\begin{aligned}
F_{m_1, \dots, m_k}[x](t) &= \int \cdots \int h_{m_1, \dots, m_k}(\tau_{11}, \dots, \tau_{1m_1}, \dots, \tau_{k1}, \dots, \tau_{km_k}) \\
&\quad \times x_1(t - \tau_{11}) \cdots x_1(t - \tau_{1m_1}) \cdots x_k(t - \tau_{k1}) \cdots \\
&\quad \times x_k(t - \tau_{km_k}) \cdots d\tau_{11} \cdots d\tau_{1m_1} \cdots d\tau_{k1} \cdots d\tau_{km_k}
\end{aligned} \tag{4.21}$$

4.2.4 Mathematical properties

The expansion and its kernels have the following properties:

Convergence Similarly to the case of the Taylor expansion for functions, the convergence of the Volterra series is not guaranteed for all functionals. A sufficient condition exists in the case of bounded inputs. The k -input Volterra expansion will converge if:

$$\int \cdots \int |h_{m_1, \dots, m_k}(\tau_{11}, \dots, \tau_{1m_1}, \dots, \tau_{k1}, \dots, \tau_{km_k})| d\tau_{11} \cdots d\tau_{1m_1} \cdots d\tau_{k1} \cdots d\tau_{km_k} \leq A_{m_1, \dots, m_k} \tag{4.22}$$

and

$$\sum_{m_1=0}^{+\infty} \cdots \sum_{m_k=0}^{+\infty} A_{m_1, \dots, m_k} B_1^{m_1} \cdots B_k^{m_k} < \infty \tag{4.23}$$

where B_1, \dots, B_k are respectively the absolute bounds of the inputs x_1, \dots, x_k (ie. $B_i = \|x_i\|_\infty$)

Causality To follow the causality condition, the kernels have to be such that if $\exists i \in \{1, \dots, k\}$ and $\exists j \in \{1, \dots, m_k\}$ such as $\tau_{ij} < 0$ then $h_{m_1, \dots, m_k}(\dots, \tau_{ij}, \dots) = 0$

Kernel limits The convergence condition implies that $\forall m \in \{1, \dots, p\}$, we have the limit $\lim_{\tau_m \rightarrow \pm\infty} h_p(\dots, \tau_m, \dots) = 0$. We find the usual assumption made for the modelling of physical systems that the influence of far-field past is neglected.

Unicity The kernels as defined by the theory of Volterra are not unique. It is possible to replace any given kernel $h_p(\tau_1, \dots, \tau_p)$ by $h_p(\tau_{\sigma(1)}, \dots, \tau_{\sigma(p)})$ where σ is a permutation of $1, 2, \dots, p$, without changing the behaviour of the system (Hennequin 2008).

To ensure unicity, several types of kernel structure can be chosen, like symmetrical kernels such as $\forall \sigma$, we have $h_p(\tau_1, \dots, \tau_p) = h_p(\tau_{\sigma(1)}, \dots, \tau_{\sigma(p)})$, or triangular kernels such as if and only if $\tau_1 \leq \dots \leq \tau_p$, we have $h_p(\tau_1, \dots, \tau_p) = 0$. Imposing these structures have the benefit to lower the number of coefficients to compute for each kernel.

Linear systems and Volterra kernels While it is intuitive to see that a linear system would have only the first-order kernel as non-zero kernel, it is wrong to think that this kernel corresponds to the linear part since the kernels may not be orthogonal. In particular, this problem has been studied by Wiener who has rewritten the series in order to have orthogonal kernels considering the distribution of the input signal.

4.2.5 Practical use

Implementation While the original Volterra series formulation describes systems in continuous time, the estimation is usually done in the discrete domain. In practice, the Volterra expansion describing the behaviour of a causal system will be limited to an order M , and all kernels will be measured only up to a certain lag N :

$$y[n] = \sum_{m_1=0}^M \cdots \sum_{m_k}^M \sum_{\tau_{11}=0}^N \cdots \sum_{\tau_{1m_1}=0}^N \cdots \sum_{\tau_{km_k}=0}^N h_{m_1, \dots, m_k}(\tau_{11}, \dots, \tau_{1m_1}, \dots, \tau_{km_k}) \quad (4.24)$$

$$\times x_1[n - \tau_{11}] \cdots x_1[n - \tau_{1m_1}] \cdots x_k[n - \tau_{km_k}]$$

Number of coefficients The Volterra representation is not very used in practical applications due to the number of parameters needed to characterize a system, even for low-order nonlinearity. In the SISO case, if we want to evaluate for each kernels with a memory of N up to order M , the number of parameters needed for one input is given by:

$$1 + M + M^2 + M^3 + \dots + M^N \approx O(M^N) \quad (4.25)$$

If we use one of the hypotheses presented earlier to ensure the unicity of the kernels

(either symmetrical or triangular), the number of coefficients for $N \leq M$ is reduced to (Hennequin 2008):

$$\sum_{n=1}^N \binom{M-n+1}{n} \quad (4.26)$$

In applications of Volterra models, the maximal order used is mostly 3, sometimes 5, what is enough to model accurately weakly nonlinear systems, such as analog lowpass filters. For strongly nonlinear systems, models with fewer parameters would be considered.

4.3 Block-based models

4.3.1 SISO models

To model nonlinear models with a more compact representation, the models have to be simplified. One way to do so is using block-based models. Block-based models are structured using cascades and sums of:

- linear filters (L), also referred to as memory linear blocks;
- nonlinear static functions (N), also referred to as memoryless nonlinear blocks.

We would consider only models without feedback loops. Depending on the number and the layout of the blocks, the SISO models have been named in literature as follows:

- Wiener models: cascade of a linear and a nonlinear blocks (LN);
- Hammerstein: cascade of a nonlinear and a linear block (NL);
- Wiener-Hammerstein: cascade of a linear, a nonlinear and a linear block (LNL);
- Polynomial (or generalized) Wiener model: sum of several parallel Wiener models with typically nonlinear blocks being powers of the input signal;
- Polynomial (or generalized) Hammerstein model: sum of several parallel Hammerstein models with typically nonlinear blocks being powers of the input signal.

Of course, the possibilities of combination are infinite but most applications focus on these five types of models.

Equivalence with Volterra kernels The block-based models can be related to a Volterra expansion with specific kernel structure. This relation are given in Table 4.1. In the table, we suppose that the general nonlinear static block $y(t) = F(x(t))$ can be expanded such as $y(t) = \sum_{n=0}^{+\infty} f_n x(t)^n$

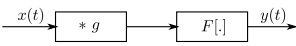
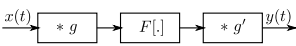
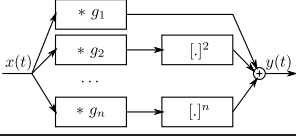
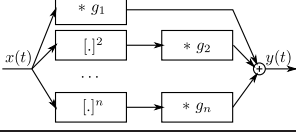
Model	Schematic	Expression	Equivalent kernels $h_n(\tau_1, \dots, \tau_n)$
Wiener		$y(t) = F((g * x)(t))$	$f_p g(\tau_1) \dots g(\tau_n)$
Hammerstein		$y(t) = (g * F(x(\cdot)))(t)$	$f_p g(\tau_1) \delta(\tau_2 - \tau_1) \dots g(\tau_n - \tau_1)$
Wiener-Hammerstein		$y(t) = (g' * F((g * x)(\cdot)))(t)$	$f_p \sum_m g'(m) g(\tau_1 - m) \dots g(\tau_n - m)$
Polynomial Wiener		$y(t) = \sum_k (g_k * x)^k(t)$	$g_n(\tau_1) \dots g_n(\tau_n)$
Polynomial Hammerstein		$y(t) = \sum_k (g * x^k)(t)$	$g_n(\tau_1) \delta(\tau_2 - \tau_1) \dots g(\tau_n - \tau_1)$

Table 4.1 Examples of SISO nonlinear block-based models (after Hennequin 2008)

4.3.2 MISO Hammerstein models

The extension of the block-based models to multiple-input systems is achieved by using multiple-input nonlinear blocks. In the case of Wiener models, or any single-input model where the input goes into a linear block, there is no unique way to extend the model. The extension of the Hammerstein model is achieved by considering a block as nonlinear static function of all the inputs. In the case of the polynomial Hammerstein model, we add the power terms corresponding to each input plus the polynomial cross-terms. These extensions are presented in Table 4.2.

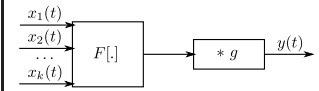
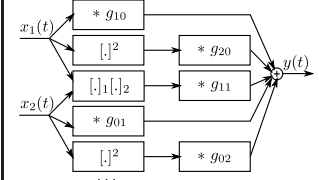
Model	Schematic	Expression
Hammerstein		$y(t) = (g * (F(x_1(\cdot), \dots, x_k(\cdot))))(t)$
Polynomial Hammerstein		$y(t) = \sum_{k_1, \dots, k_l} (g_{k_1 \dots k_l} * x_1^{k_1} \dots x_l^{k_l})(t)$

Table 4.2 Examples of MISO nonlinear block-based models (after Hennequin 2008)

4.3.3 Number of coefficients

The simple structure of the block-based structure allow to build high-order models with fewer parameters than in the case of Volterra series. The number of parameters required for a system of order M and of memory N is presented in Table 4.3. We assume that the nonlinear function are known either analytically or by polynomial expansion.

Model	Analytic nonlinear function	Polynomial nonlinear function
Hammerstein	M	$M + N$
Wiener- Hammerstein	$2M$	$2M + N$
Polynomial Wiener	/	NM
Polynomial Hammerstein	/	NM

Table 4.3 Computational complexity of SISO nonlinear block-based models

4.4 Summary

These two categories of models are the more common encountered in nonlinear modelling. The reasons of this are that, in the case of the Volterra series, virtually any nonlinear

systems can be modelled if enough orders of distortion are calculated. In the case where the systems is too strongly nonlinear, and the number of coefficients to extract is too large, the block-based models are a simple alternative that still can model accurately a wide class of physical systems. The block representation is also suited to represent nonlinear phenomena where subsystems can be identified. Furthermore, the equivalence between Volterra kernels and block-based parameters allows to use the same identification techniques.

Other models exists such as the NARMAX models (Leontaritis and Billings 1985a,b), neural networks (Chen et al. 1990), adaptive polynomial filtering (Mathews 1991). As in the case of the models described in this chapter, they are extension of linear representations.

Following the choice of a model, we have to choose one among the various identification methods present in literature in order to extract the system parameters, what is the subject of the next chapter.

Chapter 5

Identification methods

In this chapter, we explain some of the existing methods for identifying the parameters of nonlinear models based on Volterra kernels or simple block representations (Wiener, Hammerstein and polynomial Hammerstein).

5.1 Excitation signals

To evaluate the response of nonlinear methods, several methods have been reported in the literature, using three main types of excitation signals:

- Dirac impulse train;
- Sinusoids and swept-sines;
- Pseudo-random and random signals.

We will only discuss here the two last ones.

5.1.1 Sinusoids and swept-sines

For extracting the response of a system over the whole spectrum, it is possible to use sinusoids with frequencies sampling the frequency domain. Theoretically, the number of sinusoids necessary in the discrete-time domain is finite and equal to $f_s/2$. Examples of identification of Volterra kernels by designing multisine signals that cover the kernel delay domain exist in literature (Evans et al. 1996), designing the signals so that it covers the kernel delay domain.

Another way to span the whole frequency domain is to use a swept-sine signals (often called chirps). This category of signal can be represented as a frequency-varying sinusoidal signal. It is written as:

$$x(t) = \sin(\Phi(t)) \quad (5.1)$$

where the instantaneous frequency is given by:

$$f_i(t) = \frac{1}{2\pi} \frac{d\Phi}{dt}(t) \quad (5.2)$$

Two main types of swept-sine signals are used in practice: the linear swept-sine, which means that the instantaneous frequency changes linearly ($\Phi(t) = 2\pi[\alpha t^2/2 + \beta t]$ and $f_i = \alpha t + \beta$), and the logarithmic swept-sine, which means that the instantaneous frequency changes exponentially ($\Phi(t) = 2\pi\alpha\beta[\exp(t/\beta) - 1]$ and $f_i = \alpha \exp(t/\beta)$).

5.1.2 Pseudo-random and random signals

A more common type of signal used for system identification is a random signal. This class of signals exhibits very interesting properties that can be used in the context of identification. This is particularly true in the case of white Gaussian noise.

White noise A white noise has the property of having its samples uncorrelated with each other. This property is related to the flatness of its power spectrum:

$$\forall \tau_1, \tau_2 \quad \text{Cov}(x(t - \tau_1)x(t - \tau_2)) = R_{xx}(\tau_1, \tau_2) = \sigma_x^2 \delta(\tau_2 - \tau_1) \Leftrightarrow \forall \omega \quad S_x(\omega) = \sigma_x^2 \quad (5.3)$$

Furthermore, white noise is a stationary and ergodic process. Due to his flat power spectrum, a white noise has the advantage of exciting the whole frequency domain.

Gaussian noise A Gaussian noise is such that each sample follows a Gaussian law, whose probability density function is given by:

$$p(x) = \frac{1}{\sqrt{2\pi\sigma_x^2}} \exp\left(-\frac{x^2}{2\sigma_x^2}\right) \quad (5.4)$$

Maximum Length Sequence Maximum length sequence (MLS) is a pseudo-random binary sequence that was developed for digital systems using registers. The signal consists

of all the binary sequences that the system can generate, and it has the property of having a flat spectrum, except around 0Hz. We will not use this category of signals in this thesis, however MLS has been used for the identification of linear systems (Rife 1989) and Volterra series (Reed and Hawksford 1996).

5.2 LTI system identification

The material in this section is based on Westwick and Kearney (2003), Chapter 5.

Direct impulse response measurement The straightforward way to calculate the impulse response of a system would be to measure the response of the system to an impulse signal, then deconvolve it from the output signal. Problems arise from the fact that:

- In practice, it is complicated to generate a good approximation of a Dirac function by using a finite impulse of large amplitude staying in the linear range of the system;
- Deconvolving the input signal from the system response emphasizes high frequency noise;
- Pulse inputs have very little energy due to their time localization. Consequently, the signal-to-noise ratio will be very low except for usual levels of measurement noise.

Techniques exist to minimize those drawbacks, for example by averaging over system response to several pulses.

Frequency response identification Direct frequency response of the system could be measured by extracting its parameters from the system output using the formula:

$$F[\sin(\omega \cdot)](t) = |F(j\omega)| \sin(\omega t + \angle F(j\omega)) \quad (5.5)$$

However, the evaluation of the full spectrum is limited by the number of measurements. The rest of the curve would have to be interpolated. Another way to measure all the frequencies in one pass is to use swept-sine signals (Müller 2001).

Correlation-based method This class of method relies on the response of the system to noise inputs that will excite the whole spectrum in a single measurement. In the case of a white noise signal, we know that the auto-correlation of the input $x[n]$ is $\phi_{xx}[\tau] = \sigma_x^2 \delta[\tau]$, and that the input-output cross-correlation of the system $\phi_{xy}[\tau]$ whose output is $y[n]$ equals:

$$\begin{aligned}
 \phi_{xy}[\tau] &= E(x[n - \tau]y[n]) = E(x(t - \tau)(h * x)[n]) \\
 &= E(\bar{x}[\tau - n](h * x)[n]) = E((\bar{x} * (h * x))[\tau]) \\
 &= (h * E((x * \bar{x})))[\tau] = (h * E[\phi_{xx}])[\tau] \\
 &= (h * E[\sigma_x^2 \delta])[\tau] = \sigma_x^2 h[\tau]
 \end{aligned} \tag{5.6}$$

where \bar{x} is the time-reversed version of x .

In the case of a non-white noise input, a decorrelation algorithm can be used to achieve the estimation of the impulse response (Westwick and Kearney 2003) using:

$$\hat{h} = \Phi_{xx}^{-1} \phi_{xy} \text{ where } \Phi_{xx}[i, j] = \phi_{xx}[i - j] \tag{5.7}$$

Westwick also provides an algorithm designed to reduce the influence of noise in the impulse response estimation using the Akaike information criterion (Akaike 1974) to get the number of most significant samples of the estimate to take into account.

Stochastic frequency response The cross-correlation method has its alternative in the frequency domain. We know from the previous paragraph that:

$$\phi_{xy} = h * \phi_{xx} \tag{5.8}$$

which is equivalent in the frequency domain to:

$$S_{xy}(f) = H(f)S_{xx}(f) \tag{5.9}$$

where $S_{xy} = \mathcal{FT}(\phi_{xy})$ and $S_{xx} = \mathcal{FT}(\phi_{xx})$. S_{xx} is also referred to as the input power spectral density, and S_{xy} as the input-output cross-power spectral density. In the case of a white noise, we have the property that $S_{xx}(f) = \sigma_x^2$.

The frequency response of the system is estimated from estimates of the input power

and the input-output cross-power spectra:

$$\hat{H}(f) = \frac{\hat{S}_{xy}(f)}{\hat{S}_{xx}(f)} \quad (5.10)$$

In practice, issues arise from the fact that this quantity is not a good estimator of the power spectrum, and so the input power spectrum exhibits large magnitude dips. To deal with that problem, the estimate has to be averaged over several measurements. This is generally considered a time-consuming technique, particularly in comparison with swept-sine-based techniques (Müller 2001).

Least-squares regression Another way to write the input-output relation is of the form:

$$\begin{pmatrix} y(1) \\ y(2) \\ y(3) \\ \vdots \\ y(N) \end{pmatrix} = \begin{pmatrix} x(1) & 0 & 0 & \cdots & 0 \\ x(2) & x(1) & 0 & \cdots & 0 \\ x(3) & x(2) & x(1) & \cdots & 0 \\ \vdots & \vdots & \vdots & \ddots & \vdots \\ x(N) & x(N-1) & x(N-2) & \cdots & x(N-T+1) \end{pmatrix} \begin{pmatrix} h(1) \\ h(2) \\ h(3) \\ \vdots \\ h(T) \end{pmatrix} \quad (5.11)$$

or equivalently:

$$\mathbf{y} = \mathbf{X}\mathbf{h} \quad (5.12)$$

which is a suitable formulation for applying usual least-squares regression.

Assuming the measured output z is sum of the system output y and measurement noise n assumed independent of the input, the least-squares solution is given by the usual formula:

$$\hat{\mathbf{h}} = (\mathbf{X}^T \mathbf{X})^{-1} \mathbf{X}^T \mathbf{z} \quad (5.13)$$

Extension to nonlinear analysis As we will see later in this section, most of the techniques that were developed for identification of nonlinear systems are based on the identification methods we developed in this section.

5.3 Order separation

The presence of parallel subsystems of different orders in nonlinear models is complex to identify as a mixture. One possible preprocessing is called order separation, and it consists of extracting separately the response of each order before performing parameter identification on each channel.

5.3.1 Method

This method is described in Haber and Unbehauen (1990). In the case of discrete-time Volterra series, we can write it as sum of functionals:

$$y(t) = \sum_{n=0}^{+\infty} F_n[x](t) \quad (5.14)$$

where

$$F_n[x](t) = ((h_m *_{\tau_1} x) .. *_{\tau_m} x)(t) \quad (5.15)$$

In the case of other nonlinear models as the block-based ones, the definition of these functionals can vary but it is still possible to identify those channels of different order.

The channel of order n will have the property that, if we send through the system a scaled version of the input signal, we have the relation:

$$F_n[\alpha x](t) = \alpha^n F_n[x](t) \quad (5.16)$$

By using different scalings of the same signal, we get a set of equations:

$$y_i(t) = \sum_{n=0}^{+\infty} \alpha_i^n F_n[x](t) + e_i(t) \quad (5.17)$$

where $e_i(t)$ represents the noise introduced by the measurement of the system and not included in the model.

If we use M different scaling factors, and we evaluate the functionals up to order N , assuming that higher orders are negligible and are included in the system noise e_i , we get

an equation system with a Vandermonde matrix:

$$\begin{pmatrix} y_1(t) \\ \vdots \\ y_M(t) \end{pmatrix} = \begin{pmatrix} \alpha_1 & \cdots & \alpha_1^N \\ \vdots & \cdots & \vdots \\ \alpha_M & \cdots & \alpha_M^N \end{pmatrix} \begin{pmatrix} F_1[x](t) \\ \vdots \\ F_N[x](t) \end{pmatrix} + \begin{pmatrix} e_1(t) \\ \vdots \\ e_N(t) \end{pmatrix} \quad (5.18)$$

The separation is achieved by a least-mean square estimation of the functionals with a sufficient number of scaling factors ($M > N$). The estimates of each order is given by:

$$\begin{pmatrix} F_1[x](t) \\ \vdots \\ F_N[x](t) \end{pmatrix} = A^\dagger \begin{pmatrix} y_1(t) \\ \vdots \\ y_M(t) \end{pmatrix} \quad (5.19)$$

where A^\dagger is the pseudo-inverse of the Vandermonde matrix of the equation.

5.3.2 Use

Orders and pseudo-inverse conditioning When the number of orders increases for amplitudes in a given interval, the matrix quickly becomes ill-conditioned. One way to improve the conditioning is to use positive and negative scaling factors (Hennequin 2008).

Separation of even and odd orders The use of positive and negative scaling factors enables separation of perfectly even and odd orders (Haber and Keviczky 1999).

Scaling factors and pseudo-inverse conditioning The minimal conditioning at fixed N has been measured by Hennequin (Hennequin 2008) for scaling factors α spaced by 1.2dB (scaling factor 1.32).

5.4 Correlation-based methods

This class of methods was the first one to be developed for the identification of nonlinear systems. The material in this section is based on Westwick and Kearney (2003), Chapter 6.

5.4.1 Functional expansions

Volterra kernel orthogonalization These methods have been developed following the works of Wiener on the identification of continuous-time Volterra kernels (Wiener 1958) and of Lee and Schetzen for the discrete-time case (Lee and Schetzen 1965). The main idea of these techniques is that the identification of each separate Volterra kernel is made difficult by the fact that they are not orthogonal for any input signal. They have to be orthogonalized conditionally to the chosen input, usually a white noise. This is usually achieved using the Gram–Schmidt orthogonalization method.

In the case of a white Gaussian noise input of unit variance, it has been demonstrated in literature that the orthogonalization of the discrete-time kernels leads to an infinite sum of multi-input Hermite polynomials as follows (Westwick and Kearney 2003):

$$y[n] = \sum_{q=0}^{\infty} \sum_{\tau_1=0}^{\infty} \dots \sum_{\tau_q=0}^{\infty} \gamma_{\tau_1, \dots, \tau_q}^{(q)} \mathcal{H}^{(q)}(x[n - \tau_1], \dots, x[n - \tau_q]) \quad (5.20)$$

In case of a non-unit variance, the orthogonality can be established by the substitution (Westwick and Kearney 2003):

$$\mathcal{H}^{(q)}(x[n - \tau_1], \dots, x[n - \tau_q]) \rightarrow \mathcal{H}_{\mathcal{N}}^{(q)}(x[n - \tau_1], \dots, x[n - \tau_q]) \quad (5.21)$$

where $\mathcal{H}_{\mathcal{N}}^{(q)}$ is the normalized form of the Hermite polynomials. For example, the second-order Hermite polynomial $\mathcal{H}^{(2)}(u) = u^2 - 1$ becomes the second-order normalized Hermite polynomial $\mathcal{H}_{\mathcal{N}}^{(2)}(u) = u^2 - \sigma_u^2$ (see Appendix D).

Then, for a white Gaussian noise of variance σ_u^2 , the orthogonalized expansion is:

$$y[n] = \sum_{q=0}^{\infty} \sum_{\tau_1=0}^{\infty} \dots \sum_{\tau_q=0}^{\infty} \gamma_{\tau_1, \dots, \tau_q}^{(q)} \mathcal{H}_{\mathcal{N}}^{(q)}(x[n - \tau_1], \dots, x[n - \tau_q]) \quad (5.22)$$

Coefficient identification For the estimation of the system kernels, we have to truncate the orthogonalized expansion:

$$y[n] = \sum_{q=0}^Q \sum_{\tau_1=0}^{T-1} \dots \sum_{\tau_q=1}^{T-1} \gamma_{\tau_1, \dots, \tau_q}^{(q)} \mathcal{H}_{\mathcal{N}}^{(q)}(x[n - \tau_1], \dots, x[n - \tau_q]) \quad (5.23)$$

For the particular example of $Q = 2$, we can derive the relationship between the symmetrical kernels and the coefficients γ :

$$h_0 = \gamma^{(0)} \quad (5.24)$$

$$h_1(\tau) = \gamma_\tau^{(1)} \quad \text{for } 0 \leq \tau < T \quad (5.25)$$

$$h_2(\tau, \tau) = \gamma_{\tau, \tau}^{(2)} \quad \text{for } 0 \leq \tau < T \quad (5.26)$$

$$h_2(\tau_1, \tau_2) = \gamma_{\tau_1, \tau_2}^{(2)} / 2 \quad \text{for } 0 \leq \tau_1 < \tau_2 < T \quad (5.27)$$

Kernel values for $\tau_2 < \tau_1$ are obtained by symmetry $h_2(\tau_1, \tau_2) = h_2(\tau_2, \tau_1)$.

We identify the coefficients by estimating the regression matrix \mathbf{X} :

$$\mathbf{X}[n, :] = \left[\mathcal{H}_{\mathcal{N}}^{(0)} \quad \mathcal{H}_{\mathcal{N}}^{(1)}(x[n]) \dots \mathcal{H}_{\mathcal{N}}^{(1)}(x[n - T + 1]) \right. \\ \left. \mathcal{H}_{\mathcal{N}}^{(2)}(x[n], x[n]) \quad \mathcal{H}_{\mathcal{N}}^{(2)}(x[n], x[n - 1]) \dots \right] \quad (5.28)$$

If we denote the vector:

$$\theta = \left[\gamma^{(0)} \gamma_0^{(1)} \dots \gamma_{T-1}^{(1)} \gamma_{0,0}^{(2)} \gamma_{0,1}^{(2)} \dots \gamma_{0,T-1}^{(2)} \gamma_{1,1}^{(2)} \dots \gamma_{T-1,T-1}^{(2)} \right]^T \quad (5.29)$$

The input-output relationship becomes:

$$\mathbf{y} = \mathbf{X}\theta \quad (5.30)$$

Solving this equation is:

$$\hat{\theta} = (\mathbf{X}^T \mathbf{X})^{-1} \mathbf{X}^T \mathbf{y} \quad (5.31)$$

Due to the orthogonality of the polynomials, the Hessian $\mathbf{X}^T \mathbf{X}$ will be diagonal for infinite long records and can be inverted by inverting the diagonal elements. The k -th coefficient of θ is:

$$\hat{\theta}_k = \frac{\mathbf{X}[:, k]^T \mathbf{y}}{\mathbf{X}[:, k]^T \mathbf{X}[:, k]} \quad (5.32)$$

The first kernels can be extracted from the characteristics of the output signal (mean μ_y and standard deviation σ_y) (Westwick and Kearney 2003):

$$\hat{h}_0 = \hat{\theta}_1 = \mu_y \quad (5.33)$$

and

$$\hat{h}_1(\tau) = \left[\hat{\theta}_2 \dots \hat{\theta}_{T+1} \right] = \frac{1}{\sigma_x^2} \hat{\phi}_{xy}(\tau) \quad (5.34)$$

where $\hat{\phi}_{xy}$ is the estimate of the cross-correlation between the input and the output signals.

Due to the finite length of the recording, the columns of the matrix \mathbf{X} are not exactly orthogonal. To eliminate the projection error, it is possible to correct the estimation by subtracting the output of the zero-kernel (μ_y) from the output signal before computing the correlation:

$$\hat{h}_1(\tau) = \frac{1}{\sigma_x^2} \hat{\phi}_{xv_0}(\tau) \quad (5.35)$$

where $v_0 = y - \hat{h}_0 = y - \mu_y$.

This expression can also be written in the frequency domain:

$$\hat{H}_1(f) = \frac{1}{N\sigma_x^2} X^*(f) V_0(f) \quad (5.36)$$

Similar observations lead to the estimate of the second-order kernel:

$$\hat{h}_2(\tau, \tau) = \frac{1}{2\sigma_x^4} \phi_{xxv_1}(\tau, \tau) \quad (5.37)$$

$$\hat{h}_2(\tau_1, \tau_2) = \frac{1}{2\sigma_x^4} \phi_{xxv_1}(\tau_1, \tau_2) \quad (5.38)$$

where $\phi_{uvw}(\tau_1, \tau_2) = E[u(t - \tau_1)v(t - \tau_2)w(t)]$ and $v_1 = v_0 - (\hat{h}_1) * x$.

As for order 1, this relation has a frequency-domain equivalent:

$$\hat{H}_2(f_1, f_2) = \frac{1}{2N\sigma_x^4} X^*(f_1) X^*(f_2) V_1(f_1 + f_2) \quad (5.39)$$

The Lee-Schetzen algorithm Based on the previous equations, Lee and Schetzen (Lee and Schetzen 1965) developed an algorithm for kernel estimates detailed in Westwick and Kearney (2003):

1. Estimate the zero-order kernel:

$$\hat{h}_0 = \mu_y \quad (5.40)$$

2. Subtract \hat{h}_0 from the output signal to get the zero-order residue:

$$v_0[n] = y[n] - \hat{h}_0 \quad (5.41)$$

3. Estimate the first-order Wiener kernel:

$$\hat{h}_1[\tau] = \frac{1}{\sigma_x^2} \phi_{xv_0} \quad (5.42)$$

4. Compute the output of the first-order Wiener kernel:

$$\hat{y}_1[n] = \left(\hat{k}_1 * x \right) [n] \quad (5.43)$$

5. Compute the first-order residue:

$$\hat{v}_1[n] = \hat{v}_0[n] - \hat{y}_1[n] \quad (5.44)$$

6. Estimate the second-order Wiener kernel:

$$\hat{h}_2[\tau_1, \tau_2] = \frac{1}{2\sigma_x^4} \phi_{xxv_1} \quad (5.45)$$

7. Estimate the higher-order kernels similarly. The order q is obtained using the q th-order cross-correlation $\phi_{x^q v_{q-1}}$, with the residue v_{q-1} such that $v_{q-1} = v_{q-2} - \hat{y}_{q-1}$

$$\hat{h}_q[\tau_1, \dots, \tau_q] = \frac{1}{q! \sigma_x^{2q}} \phi_{x^q v_{q-1}}[\tau_1, \dots, \tau_q] \quad (5.46)$$

As showed earlier, it is also possible to compute that algorithm in the frequency domain.

As said in Westwick and Kearney (2003), this algorithm is correct only in the case where the input is actually a white Gaussian noise so its performance is as good as the input correctly approximates this ideal signal.

5.4.2 Hammerstein model

Correlation-based methods can be simplified for the case of block-based models, such as the Hammerstein model (Westwick and Kearney 2003).

In this case, the input-output relation is:

$$y[n] = h * \sum_{m=0}^M \kappa_m x^m[n] = \sum_{\tau=0}^T h[\tau] \sum_{m=0}^M \kappa_m x^m[n - \tau] \quad (5.47)$$

We rewrite the sum using Hermite polynomials:

$$y[n] = \sum_{\tau=0}^T h[\tau] \sum_{m=0}^M \gamma_m \mathcal{H}_{\mathcal{N}}^{(m)}(x[n - \tau]) \quad (5.48)$$

So then, when we calculate the input-output first-order cross-correlation, we get:

$$\begin{aligned} \phi_{xy}[k] &= \sum_{\tau=0}^T h[\tau] \sum_{m=0}^M \gamma_m E \left[x[n - k] \mathcal{H}_{\mathcal{N}}^{(m)}(x[n - \tau]) \right] \\ &= \sum_{\tau=0}^T h[\tau] \sum_{m=0}^M \gamma_m \sigma_x^m E \left[x[n - k] \mathcal{H}^{(m)} \left(\frac{x[n - \tau]}{\sigma_x} \right) \right] \end{aligned} \quad (5.49)$$

Using the fact that $\mathcal{H}^{(1)}(x) = x$, we know from the orthogonality property of the Hermite polynomials that:

$$E \left[x[n - k] \mathcal{H}_{\mathcal{N}}^{(m)}(x[n - \tau]) \right] = \begin{cases} \sigma_x^2 E[x[n - k]x[n - \tau]] & \text{if } m = 1 \\ 0 & \text{otherwise} \end{cases} \quad (5.50)$$

Then, we get from Eq. (5.49):

$$\phi_{xy}[k] = \sum_{\tau=0}^T h[\tau] \gamma_1 \sigma_x^2 \Phi_{xx}[k, \tau] \quad (5.51)$$

which can be written vectorially:

$$\phi_{xy} = \gamma_1 \sigma_x^2 \Phi_{xx} \mathbf{h} \quad (5.52)$$

where we can decide arbitrarily that $\gamma_1 = 1/\sigma_x^2$ by rescaling the filter \mathbf{h} . One should notice that in the case of systems with only even-order nonlinearities, γ_1 is 0 and so an alternative method would have to be used. However, none of the systems studied in this thesis fall in that case.

Once the filter is known, the polynomial coefficients γ can be extracted by linear regression:

$$\mathbf{y} = \mathbf{W}\gamma + \epsilon \quad (5.53)$$

where $\mathbf{X}[n, q] = \mathcal{H}^{(q-1)}(x(t))$ and \mathbf{W} is the matrix formed by filtering each column of \mathbf{X} with h (ie. $\mathbf{W}[n, q] = \sum_{\tau} h[\tau]\mathbf{X}[n - \tau, q]$). The use of the Hermite polynomials is preferable to improve the estimation due to their particular orthogonality property but any other polynomial base could be used.

5.4.3 Wiener model

Using similar calculations as in the previous section, Westwick (Westwick and Kearney 2003) explains that for a system such that:

$$y[n] = \sum_{m=0}^M \kappa_m (h * x)^m[n] = \sum_{m=0}^M \left(\sum_{\tau=0}^T h[\tau]x[n - \tau] \right)^m \quad (5.54)$$

the filter \mathbf{h} can be extracted with the same relation (assuming that the system has a odd-order nonlinearities):

$$\phi_{xy} = \sigma_x^2 \Phi_{xx} \mathbf{h} \quad (5.55)$$

Here, again, if we write the nonlinearity polynomial as $\sum_m \kappa_m x^m = \sum_m \gamma_m \mathcal{H}_{\mathcal{N}}^{(m)}(x)$, we can extract these coefficients by linear regression:

$$\mathbf{y} = \mathbf{U}\gamma + \epsilon \quad (5.56)$$

where \mathbf{U} has columns such that $u = h * x$ and $\mathbf{U}[n, :] = [1 \ \mathcal{H}_{\mathcal{N}}^{(1)}(x[n]) \dots \mathcal{H}_{\mathcal{N}}^{(M)}(x[n])]$. Once again, the normalized Hermite polynomials $\mathcal{H}_{\mathcal{N}}^{(m)}$ are chosen for their particular orthogonality property which improves the estimation, but again, other polynomial bases could be used.

5.4.4 Polynomial Hammerstein model

We look here at the polynomial Hammerstein model which has the advantage of having a reasonable level of complexity while reducing significantly the number of parameters compared to Volterra series. We follow the methodology given by Westwick for block-based models (Westwick and Kearney 2003).

In that model, the output of the system is given by:

$$y[n] = \sum_{m=0}^M (h_m * x^m)[n] = \sum_{m=0}^M \sum_{\tau=0}^T h_m[\tau] x^m[n - \tau] \quad (5.57)$$

Here again, this relation can be rewritten using the normalized Hermite polynomial. We consider a new set of filters L_n such that:

$$\begin{aligned} y[n] &= \sum_{m=0}^M \sum_{\tau=0}^T L_m[\tau] \mathcal{H}_{\mathcal{N}}^{(m)}(x[n - \tau]) \\ &= \sum_{m=0}^M \sum_{\tau=0}^T \sigma_x^m L_m[\tau] \mathcal{H}^{(m)}\left(\frac{x[n - \tau]}{\sigma_x}\right) \end{aligned} \quad (5.58)$$

In this case, the first-order cross-correlation between the residue v_p and $x_p = \mathcal{H}_{\mathcal{N}}^{(p)}(x)$ is given by:

$$\phi_{x_p v_p}[k] = \sum_{m=0}^M \sum_{\tau=0}^T L_m[\tau] E \left[x_p[n - k] \mathcal{H}_{\mathcal{N}}^{(m)}(x[n - \tau]) \right] \quad (5.59)$$

Due to the stationarity of the signal, we have:

$$E \left[x_p[n - k] \mathcal{H}_{\mathcal{N}}^{(m)}(x[n - \tau]) \right] = \begin{cases} \sigma_x^{p+m} E \left[\mathcal{H}^{(p)}\left(\frac{x[n-k]}{\sigma_x}\right) \mathcal{H}^{(m)}\left(\frac{x[n-k]}{\sigma_x}\right) \right] & \text{if } \tau = k \\ \sigma_x^{p+m} E \left[\mathcal{H}^{(p)}\left(\frac{x[n-k]}{\sigma_x}\right) \right] E \left[\mathcal{H}^{(m)}\left(\frac{x[n-\tau]}{\sigma_x}\right) \right] & \text{otherwise} \end{cases} \quad (5.60)$$

and then, due to Hermite polynomials orthogonality:

$$E \left[\mathcal{H}^{(p)}\left(\frac{x[n-k]}{\sigma_x}\right) \mathcal{H}^{(m)}\left(\frac{x[n-k]}{\sigma_x}\right) \right] = \begin{cases} p! & \text{if } m = p \\ 0 & \text{otherwise} \end{cases} \quad (5.61)$$

and:

$$E \left[\mathcal{H}^{(p)} \left(\frac{x[n-k]}{\sigma_x} \right) \right] E \left[\mathcal{H}^{(m)} \left(\frac{x[n-\tau]}{\sigma_x} \right) \right] = 0 \quad (5.62)$$

since all Hermite polynomials have zero-mean for a white Gaussian noise of variance 1 ($E [\mathcal{H}^{(m)}(x)] = E [\mathcal{H}^{(m)}(x)\mathcal{H}^{(0)}(x)]$)

That means that Eq. (5.59) becomes:

$$\phi_{x_p v_p}[k] = \sum_{\tau=0}^T L_p[\tau] E \left[x_p[n-k] \mathcal{H}_{\mathcal{N}}^{(p)}(x[n-\tau]) \right] \quad (5.63)$$

and:

$$\phi_{x_p v_p}[k] = \sigma_x^{2p} p! L_p[k] \quad (5.64)$$

So we see that the coefficients can be extracted straightforwardly, assuming that the actual involved signals are close to an ideal white Gaussian noise.

We can also extract directly from Eq. (5.63) the relation:

$$\phi_{x_p v_p}[k] = \sum_{\tau=0}^T L_p[\tau] \phi_{x_p x_p}[k-\tau] \quad (5.65)$$

which means in the frequency domain that:

$$\mathcal{FT}(L_p)(f) = \frac{S_{x_p v_p}(f)}{S_{x_p x_p}(f)} \quad (5.66)$$

where $S_{x_p v_p}$ is the cross-spectral density function between x_p and v_p . This method to the contrary of the one coming from Eq. (5.64) is using the measured power spectral density of x_p rather than the ideal one, assuming that the input x would be an infinitely-long ideal white Gaussian noise.

Finally, we have to transform the filters L_m ($1 < m < M$) to get the filters h_m using the fact that:

$$\begin{pmatrix} \mathcal{H}_{\mathcal{N}}^{(0)}(x) \\ \mathcal{H}_{\mathcal{N}}^{(1)}(x) \\ \vdots \\ \mathcal{H}_{\mathcal{N}}^{(M)}(x) \end{pmatrix} = \mathbf{B} \begin{pmatrix} 1 \\ x \\ \vdots \\ x^M \end{pmatrix} \quad (5.67)$$

where \mathbf{B} is such that:

$$\mathbf{B}[n, q] = \begin{cases} n! \frac{(-1)^k}{k! 2^k (n-2k)!} & q = n - 2k \text{ and } n > q \\ 0 & \text{otherwise} \end{cases} \quad (5.68)$$

we get that:

$$\begin{aligned} y(t) &= \sum_{m=0}^M L_m * \mathcal{H}_{\mathcal{N}}^{(m)}(x) \\ &= \sum_{m=0}^M \sigma_x^m L_m * \mathcal{H}^{(m)}\left(\frac{x}{\sigma_x}\right) \\ &= \sum_{m=0}^M \sigma_x^m L_m * \sum_{k=0}^M \mathbf{B}[m, k] x^k \\ &= \sum_{k=0}^M \left(\sum_{m=0}^M \sigma_x^m \mathbf{B}[m, k] L_m \right) * x^k \\ &= \sum_{k=0}^M h_k * x^k \end{aligned} \quad (5.69)$$

which means that:

$$\mathbf{h} = \mathbf{B}^T \mathbf{L} \quad (5.70)$$

5.4.5 Extension to two-input systems

In the case where we have a two-input/one-output system (such as ring modulators), we can extend the methods presented earlier. Indeed, we can start the calculation by considering now all the orders of two-variable polynomials and using the fact that we are sending two independent signals, x_1 and x_2 , to the two inputs of the system so that the cross-correlation of any power and any time-translation of one signal with a power of the other will follow:

$$E [x_1^k[n - \tau] x_2^l[n]] = E [x_1^k[n]] E [x_2^l[n]] \quad (5.71)$$

which will bring us back to the expression we gave for the expectations related to white Gaussian noise signals and their powers in the previous sections.

Two-input polynomial Hammerstein model

In this model, the output can be written as:

$$y[n] = \sum_{m=0}^{+\infty} \sum_{m'=0}^{+\infty} \left(h_{mm'} * \left(x_1^m[n] x_2^{m'}[n] \right) \right) [n] \quad (5.72)$$

what can be rewritten, if we denote $x_{mm'} = \mathcal{H}_{\mathcal{N}}^{(m,m')}(x_1, x_2)$, using $\mathcal{H}_{\mathcal{N}}^{(m,m')}$ as the two-variable Hermite polynomial of order (m, m') as given in Appendix D:

$$y[n] = \sum_{m=0}^{+\infty} \sum_{m'=0}^{+\infty} (L_{mm'} * x_{mm'}) [n] \quad (5.73)$$

The extraction of the coefficient of order (m, m') :

$$\begin{aligned} \phi_{x_{pp'}y}[k] &= E \left[x_{pp'}[n-k] \sum_{m=0}^{+\infty} \sum_{m'=0}^{+\infty} (L_{mm'} * x_{mm'}) [n] \right] \\ &= \sum_{m=0}^{+\infty} \sum_{m'=0}^{+\infty} \sum_{\tau=0}^{+\infty} L_{mm'}[\tau] E [x_{pp'}[n-k] x_{mm'}[n-\tau]] \\ &= \sum_{\tau=0}^{+\infty} L_{pp'}[\tau] \phi_{x_{pp'}x_{pp'}}[k-\tau] \\ &= p!p'!L_{pp'}[k] \end{aligned} \quad (5.74)$$

Thus, as in the case of a single input, the filter coefficients can be extracted directly from the ideal autocorrelation of a WGN signal:

$$L_{pp'}[k] = \frac{1}{p!p'!} \phi_{x_{pp'}y}[k] \quad (5.75)$$

or from decorrelation, for example in the spectral domain:

$$\mathcal{FT}(L_{pp'}) = \frac{S_{x_{pp'}y}}{S_{x_{pp'}x_{pp'}}} \quad (5.76)$$

5.5 Explicit least-squares method

In this section, we look at the explicit least-squares methods for model identification referred to as Hunter-Korenberg algorithm in Westwick and Kearney (2003). The algorithm has been primarily developed for identification of Volterra kernels, and the results can be extended for block-based models. This method is equivalent to the one in the previous section assuming that the input signals are ideal WGN signals. However, when this hypothesis is not fulfilled, this method will solve explicitly the least-squares regression of the output signal on the polynomial expansion (Eq. (5.30)), making no hypothesis on the structure of the input noise signals, thus having the Hessian $\mathbf{X}^T \mathbf{X}$ no longer with orthogonal columns.

5.5.1 Kernel orthogonalization

With this technique, the orthogonalization of the different kernels (e.g., using Hermite polynomials for white Gaussian noises) is no longer necessary since the regression is solved explicitly. However, in order to get Hessian matrices with better characteristics such as having the highest coefficients mostly located around the matrix diagonal, we will still use the orthogonalization method associated with the idealized signal.

5.5.2 Functional expansions

Westwick provides the equations necessary for the identification of the two first orders of functional expansions, with optimizations to minimize computation and memory space needs. However, it states that the identification of higher order would require an excessive amount of resources. For this reason, we would extend the results of the book to block-based models in order to work with higher-order models.

5.5.3 Polynomial Hammerstein model

We change the matrix \mathbf{X} to remove unnecessary (zero) coefficients. We build it such that:

$$\mathbf{X} = [\mathbf{X}_0 \ \mathbf{X}_1 \ \dots \ \mathbf{X}_N] \quad (5.77)$$

where \mathbf{X}_m are matrices such that:

$$\begin{aligned}\mathbf{X}_0[n] &= \mathcal{H}_{\mathcal{N}}^{(0)} \\ \mathbf{X}_1[n, :] &= \left[\mathcal{H}_{\mathcal{N}}^{(1)}(x[n]) \dots \mathcal{H}_{\mathcal{N}}^{(1)}(x[n - T + 1]) \right] \\ \mathbf{X}_2[n, :] &= \left[\mathcal{H}_{\mathcal{N}}^{(2)}(x[n], x[n]) \dots \mathcal{H}_{\mathcal{N}}^{(2)}(x[n - T + 1], x[n - T + 1]) \right] \\ &\dots\end{aligned}\tag{5.78}$$

We do the same modification on the θ vector such that:

$$\theta = \left[\gamma^{(0)} \quad \gamma_0^{(1)} \quad \dots \quad \gamma_{T-1}^{(1)} \quad \gamma_0^{(2)} \quad \dots \right]\tag{5.79}$$

We then need to solve the least-squares regression:

$$(\mathbf{X}^T \mathbf{X})\theta = \mathbf{X}^T \mathbf{y}\tag{5.80}$$

As explained by Westwick, Korenberg (Korenberg 1988) optimized the solving of that regression by using the internal structure of the matrices involved.

Hessian computation

The Hessian $\mathbf{H} = \mathbf{X}^T \mathbf{X}$ can be computed more efficiently by taking into account the block structure of the regression matrix \mathbf{X} . It is then possible to partition the computation as:

$$\mathbf{H} = \begin{bmatrix} \mathbf{X}_0^T \mathbf{X}_0 & \mathbf{X}_0^T \mathbf{X}_1 & \mathbf{X}_0^T \mathbf{X}_2 & \dots \\ \mathbf{X}_1^T \mathbf{X}_0 & \mathbf{X}_1^T \mathbf{X}_1 & \mathbf{X}_1^T \mathbf{X}_2 & \ddots \\ \mathbf{X}_2^T \mathbf{X}_0 & \mathbf{X}_2^T \mathbf{X}_1 & \ddots & \ddots \\ \dots & \ddots & \ddots & \ddots \end{bmatrix} = \begin{bmatrix} \mathbf{H}_{0,0} & \mathbf{H}_{0,1} & \mathbf{H}_{0,2} & \dots \\ \mathbf{H}_{1,0} & \mathbf{H}_{1,1} & \mathbf{H}_{1,2} & \ddots \\ \mathbf{H}_{2,0} & \mathbf{H}_{2,1} & \ddots & \ddots \\ \dots & \ddots & \ddots & \ddots \end{bmatrix}\tag{5.81}$$

with $\mathbf{H}_{n,q} = \mathbf{H}_{q,n}^T$

According to Westwick, the 1x1 matrix $\mathbf{H}_{0,0}$, the 1xT matrix $\mathbf{H}_{0,1}$ and the T x T matrix

$\mathbf{H}_{1,1}$ are such that:

$$\begin{aligned}
\mathbf{H}_{0,0} &= N \\
\mathbf{H}_{0,1}[1, 1] &= N\mu_x \\
\mathbf{H}_{0,1}[1, k+1] &= \mathbf{H}_{1,0}[k] - x[N-k+1] \\
\mathbf{H}_{1,1}[n, q] &= \mathbf{X}_1[:, p]^T \mathbf{X}_1[:, q] \\
\mathbf{H}_{1,1}[l+1, 1] &= N\phi_{uu}(l) \\
\mathbf{H}_{1,1}[l+k+2, k+1] &= \mathbf{H}_{1,1}[l+k+1, k] - u[N-k+1]u[N-k-l+1]
\end{aligned} \tag{5.82}$$

with μ_x the mean of the input signal x .

The other matrices are different than the ones for Volterra kernels. For example, we will have $\mathbf{H}_{0,2}$ as a $1 \times T$ matrix such that:

$$\begin{aligned}
\mathbf{H}_{0,2}[1, 1] &= \sum_{n=0}^{T-1} u[n]^2 \\
&= N\phi_{uu}(0) \\
\mathbf{H}_{0,2}[1, k+1] &= \sum_{n=k}^{T-1} u[n]^2 \\
&= \mathbf{H}_{0,2}[1, k] - \mathcal{H}_{\mathcal{N}}^{(2)}(u[N-k+1])
\end{aligned} \tag{5.83}$$

and $\mathbf{H}_{1,2}$ as a $T \times T$ matrix such that:

$$\begin{aligned}
\mathbf{H}_{1,2}[n, q] &= \mathbf{X}_1[:, p]^T \mathbf{X}_1[:, q] \\
\mathbf{H}_{1,2}[l+1, 1] &= N\phi_{uu^2}(l) \\
\mathbf{H}_{1,2}[l+k+2, k+1] &= \mathbf{H}_{1,2}[l+k+1, k] - \mathcal{H}_{\mathcal{N}}^{(2)}(u[N-k+1])\mathcal{H}_{\mathcal{N}}^{(2)}(u[N-k-l+1])
\end{aligned} \tag{5.84}$$

Other blocks can be computed on a similar way, using higher-order auto-correlations of the input signal.

Right member computation

The right member of the equation corresponds to $\mathbf{O} = \mathbf{X}^T \mathbf{y}$ that can also be decomposed as:

$$\mathbf{O} = \begin{bmatrix} \mathbf{X}_0^T \mathbf{y} \\ \mathbf{X}_1^T \mathbf{y} \\ \mathbf{X}_2^T \mathbf{y} \\ \dots \end{bmatrix} = \begin{bmatrix} \mathbf{O}_0 \\ \mathbf{O}_1 \\ \mathbf{O}_2 \\ \dots \end{bmatrix} \quad (5.85)$$

with \mathbf{O}_0 a 1x1 vector and \mathbf{O}_l , for $l > 0$, $T \times 1$ vectors. This gives block by block:

$$\mathbf{O}_0 = N\mu_z \quad (5.86)$$

where μ_z is the average of the output signal, and:

$$\begin{aligned} \mathbf{O}_1[k] &= \mathbf{X}_1[:, k]^T \mathbf{y} \\ &= \sum_{n=0}^{T-1} x[n-k+1]z[n] \\ &= N\phi_{uz}(k-1) \end{aligned} \quad (5.87)$$

and:

$$\begin{aligned} \mathbf{O}_2[k] &= \mathbf{X}_2[:, k]^T \mathbf{y} \\ &= \sum_{n=0}^{T-1} \mathcal{H}_{\mathcal{N}}^{(2)}(x[n-k+1])z[n] \\ &= N\phi_{\mathcal{H}_{\mathcal{N}}^{(2)}(u)z}(k-1) \end{aligned} \quad (5.88)$$

and so on.

The computation of the high-order correlation can be optimized by choosing carefully the loop order to compute all the coefficients. Furthermore, in the case of the polynomial Hammerstein model, only 1st-order correlations are involved, so they can be computed efficiently in the frequency domain. Then, the regression solution is extracted using Cholesky factorization.

5.5.4 Extension to two-input systems

As in the case of the correlation-based methods, the extension of the method to two-input systems is solved by adding more terms in the regression. Thus, we will add in vector \mathbf{X} terms relative to the polynomial signals related to the second input signal, as well as the polynomial cross-terms between the two. The computation and the inversion of the Hessian stay the same.

5.5.5 Computation cost

Despite several optimization, this algorithm stays significantly more costly than the previous one. In terms of computation time, the computation of all the Hessian terms and the factorization are significantly longer than correlation calculations. In terms of memory, the Hessian is usually a very large matrix as soon as the desired number of orders and filter length become significant, requiring a large amount of computer memory.

5.6 Swept-sine-based method

This method, first introduced by Farina (Farina and Farina 2000), has been recently developed using logarithmic swept-sine excitation and deconvolution to extract the impulse responses of each distortion order of a nonlinear system. This method is implicitly related to the polynomial Hammerstein model due to its output composed of n impulse responses related to n filters, respectively corresponding to n -th distortion order.

5.6.1 Excitation signal

A swept-sine (see Section 5.1.1) of length T starting at f_1 ($f_i(0) = f_1$) and ending at f_2 ($f_i(T) = f_2$) has a phase Φ such that:

$$\Phi(t) = 2\pi \frac{f_1 T}{\ln(f_2/f_1)} (e^{(t/T)\ln(f_2/f_1)} - 1) \quad (5.89)$$

However, as demonstrated in Rébillat et al. (2011), the phase properties make it necessary to limit ourselves to some duration T_m such that $T_m = (2m\pi - \pi/2) \ln(f_2/f_1)$. In this

particular case:

$$\cos(k\Phi(t)) = \cos(\Phi(t + \Delta t_k)) \quad \text{with } \Delta t_k = \frac{T_m \ln k}{\ln(f_2/f_1)} \quad (5.90)$$

which means that rescaling the time scale is equivalent to translate the time origin.

5.6.2 Inverse signal

The construction of an inverse signal \hat{x} defined such that $\hat{x} * x(t) = \delta(t)$ is not always mathematically possible (Rébillat et al. 2011) due to the band-limited property of the signal. However, an approximate inverse exists and it is given as the time-inverse of the swept-sine with a decreasing exponential envelope such that:

$$\hat{x}(t) = \frac{f_1 \ln(f_2/f_1)}{T} \exp\left(\frac{t \ln(f_2/f_1)}{T}\right) s(-t) \quad (5.91)$$

To model properly the nonlinear behaviour of the system up to order N , since the N -th distortion produces components up to frequency $f_3 = Nf_2$, the inverse signal has to be defined up to T_{inv} such that $\hat{x}(T_{\text{inv}}) = f_3$.

5.6.3 Extraction of the impulse responses

After deconvolution of the response $y(t)$ of the system from the input $x(t)$, we get a signal $s(t) = y * \hat{x}(t)$ where the m -th order impulse response of length K is such that:

$$L_m[n] = s[\Delta t_m - n] \quad \text{for } 0 \leq n < K \quad (5.92)$$

A last step is required to get the expression of the filters in the polynomial Hammerstein expansion. Indeed, the filters $L_m(f)$ correspond to an expansion with Chebyshev polynomials (which are such that $\mathcal{T}^{(m)}(\sin(t)) = \sin(mt)$). A linear transform can then convert the filter family L into the desired filters H as explained in Novak (2009).

5.6.4 Extension to two-input systems

The extension of this method to the case of two-input systems is not straightforward. If the swept-sine signal can cover the whole frequency range along one dimension, it is not

possible to get the same property on a two-dimension frequency domain.

5.7 Summary

In this section, we reviewed some of the more common nonlinear model identification techniques, in order to extract the parameters of a system in few of the model examples we saw in Chapter 4, and we extended these methods to the case of multi-input systems. The methods based on correlation are the most widespread nowadays Westwick and Kearney (2003), but they suffer from the intrinsic drawbacks of the power spectral density and cross-spectral density estimation (Oppenheim et al. 1999). It is possible to improve those estimations using explicit resolution of the least-squares equation but with significantly higher computation costs. A new method using a swept-sine signal excitation does not have these flaws, but it is not suitable for the identification of multi-input systems which is problematic in our scope since several synthesizer effects have more than one input.

The next step is then to apply the techniques presented here to our systems (see Appendix B) and test their performance compared to the expected result (see Chapter 3) and simulation techniques based on circuit modelling. This will be the purpose of the next chapter.

Chapter 6

Applications to synthesizer circuits

This section is organized in two main parts. First, we test the identification methods presented in the previous chapter on numerical implementations of the Moog ladder filter as well as on measurements made on the system. Next, we test the two-input extension of these methods to the two ring modulators presented in Appendix B, the Korg MS-50 and the Moogerfooger MF-102.

6.1 Implementation of the identification methods

We implemented the methods based on cross-correlation using the frequency-domain expressions for the identification of Wiener, Hammerstein and polynomial Hammerstein models. In order to improve the estimation of the cross-power spectral density and the power spectral density, we apply the algorithm on signal segments of length sixteen times the desired filter length in the model. Then, the final estimation is made by averaging all these results, performing the inverse Fourier transform and truncating the resulting filter to its expected length.

Computation time Our estimations were performed on a Mac Pro (2x2.26GHz Quad-core, 12GB of RAM) using Matlab. The estimations on the three block models were usually quite quick ($< 10s$).

Estimation error To evaluate the accuracy of our modelling, we use the criterion introduced in Kearney and Hunter (1983) called *variance accounted for* (VAF) which is equal

to:

$$VAF = \frac{\text{var}(y - \hat{y})}{\text{var}(y)} \quad (6.1)$$

6.2 Moog ladder filter numerical models

6.2.1 Circuit modelling

In cases where the electronic structure of the system is known, there are alternatives to the black-box approach developed in Chapter 4. Knowing the characteristics of the nonlinear components used in the circuits that we saw in the Chapter 2, we can use different strategies to model the behaviour of the system. Examples are:

- Backward finite difference;
- Truncated Volterra series.

6.2.2 Backward finite difference

Theory

This method is a well-known technique of discretization for differential equations. The discretization is achieved by using the approximation:

$$\frac{df}{dt}(t) \approx \frac{f(t) - f(t - \Delta t)}{\Delta t} \quad (6.2)$$

what gives in discrete time:

$$\frac{df}{dt}[n] \approx \frac{f[n] - f[n - 1]}{T_s} \quad (6.3)$$

where T_s is the sampling period.

Advantages The backward finite difference has the advantages of being simple to calculate and to implement. That is why this method is often used for preliminary simulation of behaviour of the system.

Disadvantages This method has both poor convergence and poor stability properties as soon as the sampling period increases. Furthermore, the energy conservation is usually not verified.

Finite difference model of the Moog filter

Since the equations of the filter are only first order, the stability properties of the discretized model are identical to those of the original continuous-time system (Huovilainen 2004). The discretization of the equations of one stage (Eq. (2.2)) gives:

$$v_n[m] = v_n[m - 1] + \omega T_s (\tanh(v_{n-1}[m]) - \tanh(v_n[m - 1])) \quad \text{for } n = 1, 2, 3, 4 \quad (6.4a)$$

$$v_0[m] = v_{in}[m] - 4rv_4[m - 1] \quad (6.4b)$$

This model unfortunately doesn't correctly reproduce the phase shift of the Moog filter. Methods to compensate this shift can be found in papers by Stilson (Stilson and Smith 1996) and Huovilainen (Huovilainen 2004).

6.2.3 Truncated Volterra series

An original use of the Volterra series was introduced for solving weakly nonlinear partial differential equations (Hélie and Hasler 2004). In the particular case of electronics, this method could be summarized as a two-step process:

- Calculation of the Volterra expansion of small sub-circuits up to a desired, rather small order (usually 3), using the differential equations relative to input and output voltages and the composition laws;
- Calculation of the Volterra expansion of the whole system using the equations relative to composition of subsystems which Volterra kernels are known up to a certain order.

In this method, the calculations are performed in the Laplace domain.

Composition laws

The three types of composition studied here are the sum, the product and the cascade of 2 subsystems f and g whose kernels are denoted $\{f_n\}$ and $\{g_n\}$ (Fig. 6.1). The composition

laws that give the global system h ($\{h_n\}$) are given by (Hélie 2006):

$$H_n(s_1, \dots, s_n) = F_n(s_1, \dots, s_n) + G_n(s_1, \dots, s_n) \quad (6.5)$$

$$H_n(s_1, \dots, s_n) = \sum_{p=1}^{n-1} F_p(s_1, \dots, s_p) G_{n-p}(s_{p+1}, \dots, s_n) \quad (6.6)$$

$$H_n(s_1, \dots, s_n) = \sum_{p=1}^n \sum_{(i_1, \dots, i_p) \in \mathbb{I}_n^p} F_{i_1}(s_1, \dots, s_{i_1}) \dots F_{i_p}(s_{i_1+\dots+i_{p-1}+1}, \dots, s_n) \cdot G_{n-p}(s_1 + \dots + s_{i_1}, \dots, s_{i_1+\dots+i_{p-1}+1} + \dots + s_n) \quad (6.7)$$

where $\mathbb{I}_n^p = \{(i_1, \dots, i_p) > 0 \text{ such that } i_1 + \dots + i_p = n\}$.

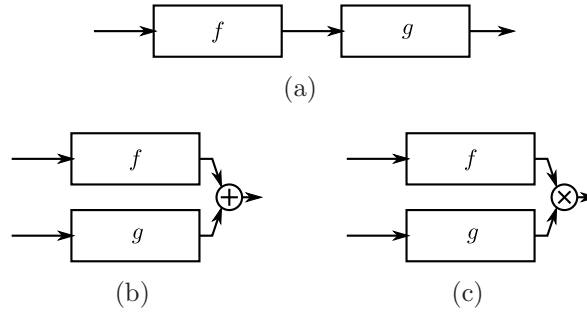


Fig. 6.1 Types of subsystem composition: (a) cascade, (b) sum, (c) product (after Hélie 2010)

Volterra model expression for the Moog filter

This model is developed by Hélie (Hélie 2006). Using the composition laws demonstrated in (Hélie 2010), we can derive the kernels of one stage up to order 5:

$$F_1(s_1) = c_1 Q_F(s_1) \quad (6.8a)$$

$$F_3(s_1, s_2, s_3) = c_3 Q_F(s_1 + s_2 + s_3) \cdot [1 - F_1(s_1)F_1(s_2)F_1(s_3)] \quad (6.8b)$$

$$F_5(s_1, s_2, s_3, s_4, s_5) = Q_F(s_1 + \dots + s_5) \cdot \left[c_5 - c_5 \prod_{k=1}^5 F_1(s_k) - c_3 \cdot (F_1(s_1)F_1(s_2)F_3(s_3, s_4, s_5) + F_1(s_1)F_3(s_2, s_3, s_4)F_1(s_5) + F_3(s_1, s_2, s_3)F_1(s_4)F_1(s_5)) \right] \quad (6.8c)$$

where $\tanh x \approx c_1x + c_3x^3 + c_5x^5$, with $\{c_1 = 1, c_3 = -1/3, c_5 = 2/15\}$, and $Q_F(s) = [c_3 + s/\omega]^{-1}$

The kernels F_m^4 for the complete filter without feedback are deduced from the formulas for cascaded systems (Eq. (6.7)) applied twice (first to get the kernels F_m^2 of a two-stage filter, then to get the kernels of a four-stage filter):

$$F_1^2(s_1) = [F_1(s_1)]^2 \quad (6.9a)$$

$$F_3^2(s_1, s_2, s_3) = F_1(s_1)F_1(s_2)F_1(s_3)F_3(s_1, s_2, s_3) + F_1(s_1 + s_2 + s_3)F_3(s_1, s_2, s_3) \quad (6.9b)$$

$$\begin{aligned} F_5^2(s_1, s_2, s_3, s_4, s_5) = & F_1(s_1)F_1(s_2)F_1(s_3)F_1(s_4)F_1(s_5)F_5(s_1, s_2, s_3, s_4, s_5) + \dots \\ & F_1(s_1 + s_2 + s_3 + s_4 + s_5)F_5(s_1, s_2, s_3, s_4, s_5) + \dots \\ & F_3(s_1, s_2, s_3 + s_4 + s_5)F_1(s_1)F_1(s_2)F_3(s_3, s_4, s_5) + \dots \end{aligned} \quad (6.9c)$$

$$\begin{aligned} & F_3(s_1, s_2 + s_3 + s_4, s_5)F_1(s_1)F_3(s_2, s_3, s_4)F_1(s_5) + \dots \\ & F_3(s_1 + s_2 + s_3, s_4, s_5)F_3(s_1, s_2, s_3)F_1(s_4)F_1(s_5) \end{aligned} \quad (6.9d)$$

and then the same expressions replacing F_m^2 by F_m^4 and F_m by F_m^2 .

Two techniques to extract the kernels for the filter with feedback are presented in two papers by Hélie (Hélie 2006, 2010).

Practical implementation The formulation in the Laplace domain implies the use of techniques to numerically compute the multidimensional inverse Laplace transform. An alternative is suggested by Hélie in building a block based computation scheme based on the basic block F_1 and polynomial function blocks to reproduce the expression in the kernel equations (Eqs. 6.8 and 6.9).

6.3 Finite difference model study

We first try to use the finite difference model of Huovilainen as a reference to study the identification techniques. The model contains in its equation some nonlinear functions (the hyperbolic tangent functions) that should lead to a distorted output signal similar to the actual Moog filter.

6.3.1 Sinusoidal excitation

We feed the model with a sinusoidal signal, and, based on the relationship we found in Section 3.3.1, we set the amplitude at 60mV (amplitude of ~ 3 and scaling factor of ~ 0.02). We set the model with a control current at 390mA and a resonance coefficient at 0 and the sinusoid at a frequency of 400Hz (1st test), and 2kHz (2nd test).

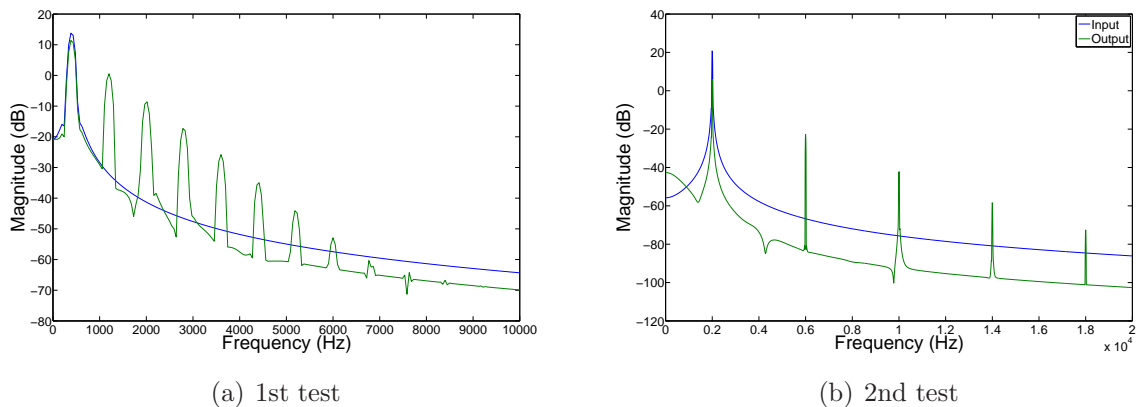


Fig. 6.2 Huovilainen model — Input and output spectra for sinusoidal excitation

We see that the results (Fig. 6.2) correspond qualitatively to the one found in Chapter 3 with high-order distortions before the cutoff frequency and only low-order distortion above it.

6.3.2 Even-order distortion

If we look at the previous experiment, we see that the sinusoidal excitation produces only odd-order distortion in the output signal. Thus, it does not correspond to our measurements in Chapter 3 where significant even-order distortions were present. Observations made previously in this report provide us with two possible explanations: circuit asymmetries and DC offset.

Asymmetries As shown in Section 2.3, asymmetries in the filtering stage modify quite simply the equations. To test this model, we can unbalance the transistor saturation current

I_S to $\pm 1\%$. This leads to a factor β (see Section 2.3) such that:

$$\beta = \frac{1}{2} (\log(1.01) - \log(0.99)) \approx 0.01 \quad (6.10)$$

If we modify accordingly the finite difference model in the case of the 1st experiment of sinusoidal excitation, we get the output spectrum displayed in Fig. 6.3.

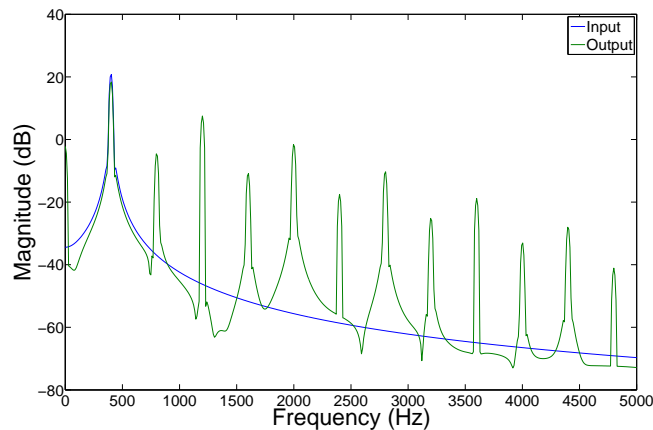


Fig. 6.3 Huovilainen model — Input and output spectra for asymmetric stages

We see that with asymmetric properties, even-order peaks are clearly visible on the spectrum, suggesting the importance of component symmetry in the circuit to achieve a particular nonlinear behaviour.

Input DC offset If we take the equation found in Section 3.3.1 which suggests the presence of an offset of 1.8mV at the input of the filtering stage, we test the model response when a signal composed of the sum of a sinusoid and this offset is sent. We get the output spectrum shown in Fig. 6.4.

In this case too, we notice the presence of even-order components as in the measurements on the actual system. That means that the presence of the offset could be one of the main factors responsible for the even distortions we observed on the filter.

Output DC offset In both cases, the output signal of the model has a strong DC component. That means that the output buffer circuit of the Moog filter would have to

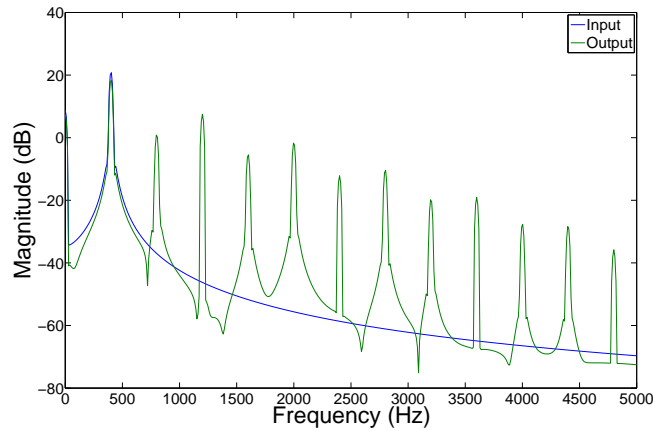


Fig. 6.4 Huovilainen model — Input and output spectra for input signal with DC offset

act as a highpass filter in order to remove that offset from the actual output signal of the Moog filter.

6.3.3 Distortion

We used the signal that we measured at the entrance of the filtering stage on the Moog filter when we were sending as input a swept-sine signal (Experiment 37). The distortion curves were then extracted from the output signal of the model; they are presented in Fig. 6.5.

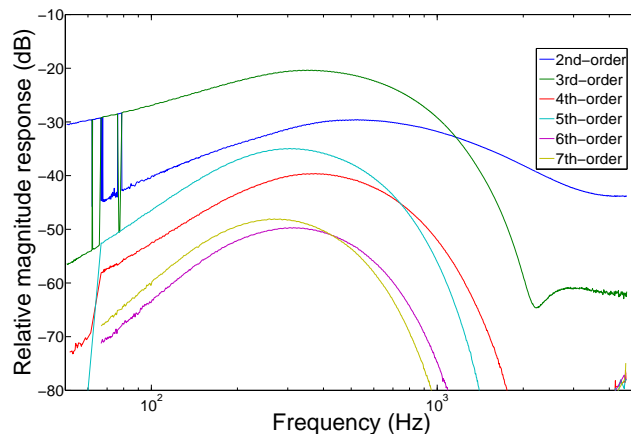


Fig. 6.5 Huovilainen model — Distortion

As we can see in the figure, the results are very similar to what was observed in Chap-

ter 3 on the filter output, which means that this discrete model is a quite accurate model concerning the nonlinear properties of the Moog filter.

6.3.4 Nonlinear identification

Considering the similarity between the distortion behaviour of the numerical model and the one of the actual Moog filter, we decided to test the identification methods we presented.

Wiener model

We applied the correlation-based identification method for Wiener models. We used a WGN signal with a standard deviation of 100mV in order to cover the usual sinusoidal excitation range of the filtering stage. The polynomial coefficients are displayed in Table. 6.1 and the associated filter in Fig. 6.6.

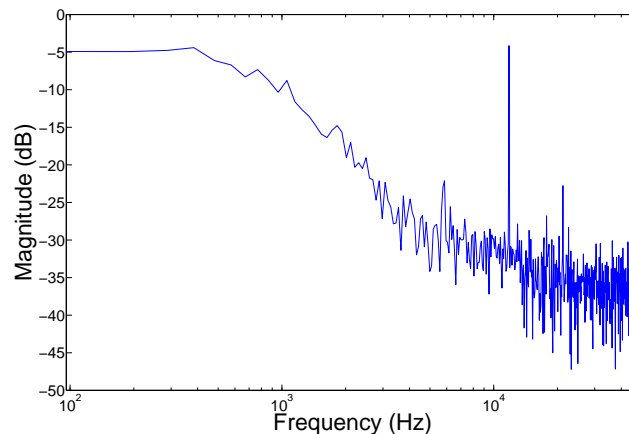


Fig. 6.6 Huovilainen model — filter of the Wiener and the Hammerstein models

As expected for a weakly nonlinear model, most of the behaviour of the system is extracted from the 1st-order coefficient. However, we see that the error stays constant and quite high for all identification orders, suggesting that the Wiener structure is not appropriate for modelling the nonlinearities of the filter.

Coefficients	1st-order	2nd-order	3rd-order	4-order	5th-order	6th-order	7th-order	Error
Model								
Order 1	1.0035	-	-	-	-	-	-	15.73%
Order 2	1.0037	-1.5787	-	-	-	-	-	15.72%
Order 3	1.0017	-1.6129	44.7992	-	-	-	-	15.72%
Order 4	1.0042	-3.2576	-17.6636	18206.3842	-	-	-	15.72%
Order 5	1.0042	-3.2576	-17.6636	18206.3842	0	-	-	15.72%
Order 6	1.0042	-3.2576	-17.6636	18206.3842	0	0	-	15.72%
Order 7	1.0042	-3.2576	-17.6636	18206.3842	0	0	0	15.72%

Table 6.1 Huovilainen model — Polynomial coefficients of the Wiener model

Hammerstein model

We performed the identification algorithm for Hammerstein models on the same signals as for the Wiener model. Results are presented in Table. 6.2 and the associated filter in Fig. 6.6. It is identical to the filter of the Wiener model since their estimation method is the same (see Section 5.4).

Coefficients	1st-order	2nd-order	3rd-order	4-order	5th-order	6th-order	7th-order	Error
Model								
Order 1	1.0034	-	-	-	-	-	-	15.73%
Order 2	1.0026	0.1007	-	-	-	-	-	15.73%
Order 3	1.4107	0.0121	-13.7847	-	-	-	-	15.73%
Order 4	1.4110	0.0711	-13.7850	-1.0085	-	-	-	15.73%
Order 5	1.6797	-0.0519	-32.1936	0.5394	185.0463	-	-	15.73%
Order 6	1.6796	-0.2314	-32.1914	6.6542	185.2601	-41.3837	-	15.73%
Order 7	1.8887	0.0361	-53.5071	-1.8582	628.1667	16.7949	-2209.1729	15.73%

Table 6.2 Huovilainen model — Polynomial coefficients of the Hammerstein model

Here again, the extraction of high-order coefficients does not improve the identification of the system suggesting that the Hammerstein model is also not appropriate for this system.

Polynomial Hammerstein model

Finally, we tested the method for polynomial Hammerstein models. Results are presented in Table. 6.3 and the associated filter in Fig. 6.7.

In this case, the addition of higher-order components to the model results in significantly lowering the estimation error. That suggests that the complexity of this model better fits the behaviour of the system.

Model	Error
Order 1	15.80%
Order 2	15.66%
Order 3	6.19%
Order 4	6.09%
Order 5	3.38%
Order 6	3.36%
Order 7	1.91%

Table 6.3 Huovilainen model — Estimation error of the polynomial Hammerstein model

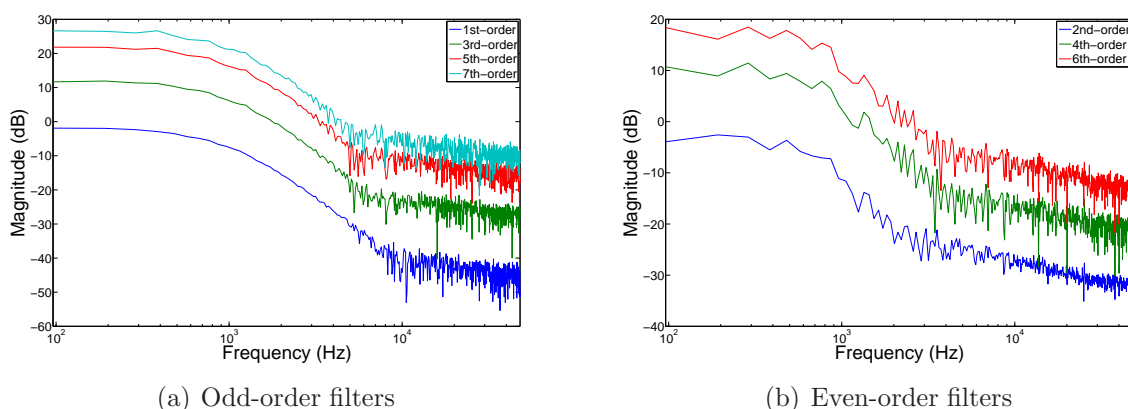


Fig. 6.7 Huovilainen model — filters of the polynomial Hammerstein model

Distortion To test the accuracy of the identified model, we ran the same test that we did earlier (see Section 6.3.3), sending the measured signal to the input of the extracted system model. The distortion curves are displayed in Fig. 6.8

We can see that except for the noisy behaviour introduced by the error in the estimation of the cross-spectral density and the power spectral density, the general behaviour of the nonlinear components of the signal fits quite well with what we observed in Fig. 6.5. This result supports the idea that the complexity of the polynomial Hammerstein model associated with better identification methods could model quite accurately the Moog filter.

6.4 Nonlinear identification of the Moog ladder filter

After having tested the methods on the numerical model, we made measurements on the Moog filter using a white Gaussian noise in order to estimate its parameters.

The parameters of the models in this section were identified from the measurements of

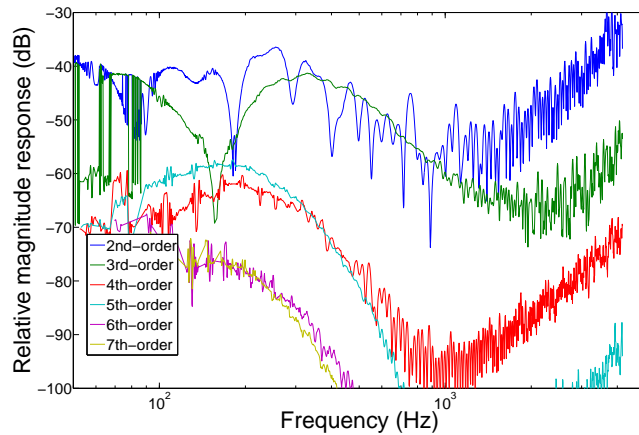


Fig. 6.8 Huovilainen model — Distortion of the polynomial Hammerstein model

the experiment 44 (see Appendix C).

Input signal The input signal was generated numerically using Matlab and then converted by the DAC. It appears that it is not exactly a Dirac function when we calculate the autocorrelation of the signal measured at the output of the DAC as it would be for ideal white Gaussian noise. However, since our methods use an estimated power spectral density rather than an ideal one, we expect this imperfection not to introduce too significant a bias.

Order separation It was not possible in our experiments to manage to measure the output of the filter for different scaled versions of the same noise signal. Indeed, the inaccurate synchronization between the input emission and the output acquisition (the acquisition is triggered using an impulse sent on a parallel channel of the DAC), from generating a scaled version of the signal on the computer did not result in an exactly scaled output.

Wiener model

We first tested the Wiener model. The identification results are displayed in Table. 6.4 and the associated filter in Fig. 6.9.

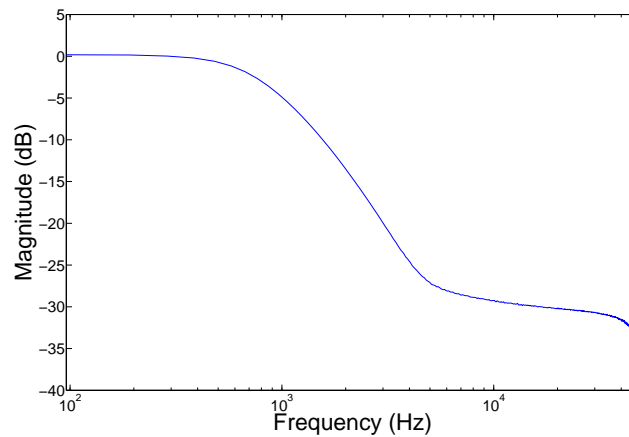


Fig. 6.9 Moog filter — filter of the Wiener and the Hammerstein models

Coefficients	1st-order	2nd-order	3rd-order	4-order	5th-order	6th-order	7th-order	Error
Model								
Order 1	0.9999	0.9999	0.9999	1.0000	1.0006	1.0006	0.9999	0.9501%
Order 2	-	0.0045	0.0045	0.0245	0.0234	0.0196	0.0223	0.9501%
Order 3	-	-	-0.0013	-0.0158	-0.4319	-0.4272	0.2949	0.9501%
Order 4	-	-	-	-3.1132	-2.8909	-1.7074	-2.6511	0.9500%
Order 5	-	-	-	-	38.6443	38.1482	-102.4051	0.9500%
Order 6	-	-	-	-	-	-73.8571	-10.1192	0.9500%
Order 7	-	-	-	-	-	-	6524.8667	0.9500%

Table 6.4 Moog filter — Polynomial coefficients of the Wiener model

As we can see, the estimation error is very low. Especially it is much lower than what we had for the numerical model of the filtering stage.

Hammerstein model

The Hammerstein model of the Moog was derived from the same experiment. The parameters of the model are displayed in Table. 6.5 and in Fig. 6.9.

Here again, the identification error was surprisingly much lower than for the numerical model, and very close to the error found for the Wiener model.

Polynomial Hammerstein model

To improve the complexity of the model, we performed the identification of the polynomial Hammerstein filters. The filters are displayed in Fig. 6.10 and the error in Table 6.6.

Coefficients	1st-order	2nd-order	3rd-order	4-order	5th-order	6th-order	7th-order	Error
Model								
Order 1	0.9999	0.9999	1.0083	1.0083	1.0090	1.0090	1.0091	0.9501%
Order 2	-	-0.0207	-0.0208	-0.0191	-0.0192	-0.0156	-0.0156	0.9444%
Order 3	-	-	-0.0389	-0.0389	-0.0447	-0.0450	-0.0465	0.9402%
Order 4	-	-	-	-0.0037	-0.0037	-0.0205	-0.0204	0.9402%
Order 5	-	-	-	-	0.0081	0.0085	0.0129	0.9402%
Order 6	-	-	-	-	-	0.0161	0.0159	0.9401%
Order 7	-	-	-	-	-	-	-0.0031	0.9401%

Table 6.5 Moog filter — Polynomial coefficients of the Hammerstein model

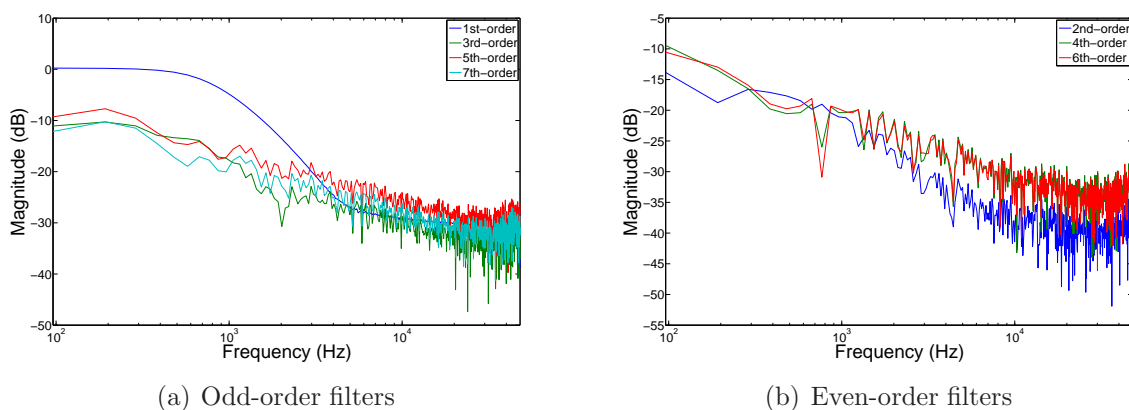


Fig. 6.10 Moog filter — filters of the polynomial Hammerstein model

In this case too, we find a very low estimation error. However, the polynomial Hammerstein model seems to improve as we use higher-order model which was not the case for the previous models. It corresponds to what we already observed on the numerical model, in the sense that the polynomial Hammerstein model is probably capable of estimating a large part of the behaviour of the system.

Distortion We test the response of the system to harmonic signals. For this purpose, the nonlinear behaviour of the model at order 7 for the 2nd- and 3rd-order components was extracted when we send as input a swept-sine of amplitude σ (Fig 6.11).

We see that the nonlinear behaviour does not fit very well with the real distortion of the Moog filter. This suggests that the identification method is not robust enough to approach the weak nonlinearities of the ladder filters with a background measurement noise. However, we can see that the level of the distortion at low frequencies is very similar. While the overall identification error is much lower than for the numerical model, we actually lost

Model	Error
Order 1	0.9486%
Order 2	0.9425%
Order 3	0.9377%
Order 4	0.9372%
Order 5	0.9367%
Order 6	0.9366%
Order 7	0.9366%

Table 6.6 Moog filter — Estimation error of the polynomial Hammerstein model

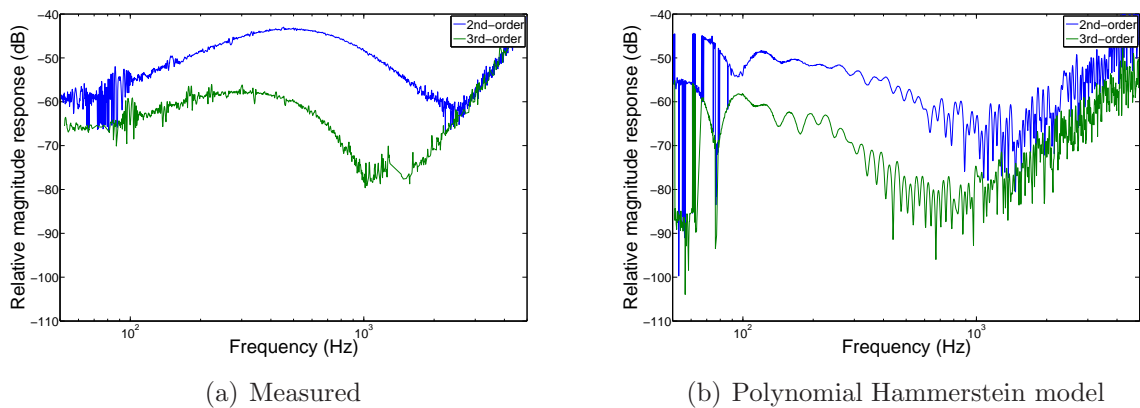


Fig. 6.11 Moog filter — Distortion curves of the polynomial Hammerstein model (2nd- and 3rd-order)

accuracy related to approximating the nonlinear behaviour that we had for the Huovilainen model.

Explicit least-squares method

We tested the explicit least-squares method for the polynomial Hammerstein model as explained in Section. 5.5. The estimation was performed for a system of order 5. The filters are displayed in Fig. 6.12 and the error in Table 6.7.

Model	Error
Order 5	0.9360%

Table 6.7 Moog filter — Estimation error of the polynomial Hammerstein model using explicit least-squares

We can see on the results that this method shows actual improvement compared to

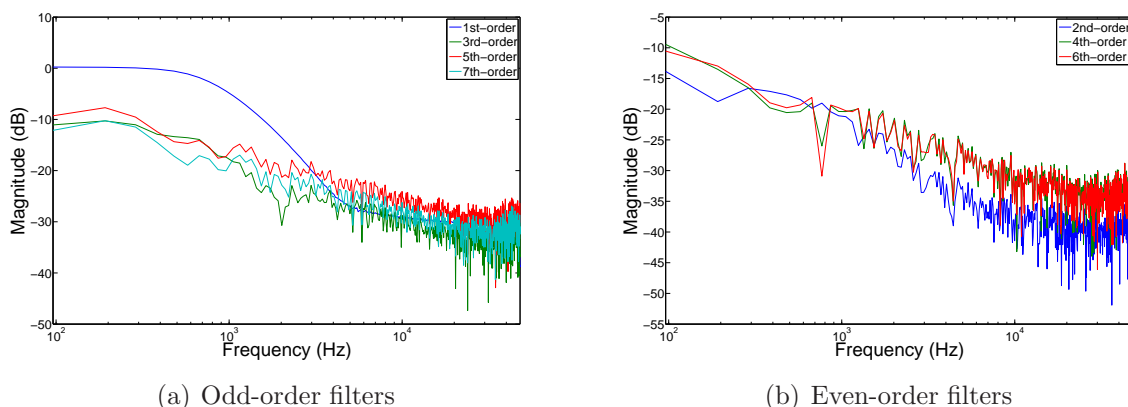


Fig. 6.12 Moog filter — filters of the polynomial Hammerstein model

the correlation-based method. Moreover, the filter estimations seem smoother than in the previous technique. However, there is still a lot of noise on those estimations compared to the measured distortion curves. Considering that this estimation is almost 300 times slower in this experiment and requires significantly more memory, the slight improvement it provides has to be weighted with these constraints.

Remarks on 1-input model identification

Estimation error As we saw in this section, the identification in the case of the actual filter has much lower estimation errors. The probable source of this phenomenon is that the filter was tested at a lower input signal level, resulting in a less significant nonlinear behaviour. In this case, the estimation of the linear part was enough to fit the filter response very closely.

Validity range and input voltage range We noticed in our tests using the models that the estimated parameters can only be considered as valid in a range close to the interval $\pm\sigma V$ (σ being the noise standard deviation), while the high-order coefficients will strongly degrade the model output for larger signals. The problem is then that using as input a noise signal which has a standard deviation comparable to the possible limit voltage (according to the filter characteristics) at the input of the filter would mean having a significant number of samples outside that range resulting in undesirable nonlinear effects due to the saturation of the different components of our experimental benchmark (digital-to-analog converter,

filter, acquisition card). Thus, we have to limit ourselves to limits that correspond to quite low signal level compared to the actual available range on the effect.

High-frequency response The behaviour of the models for high frequencies and for higher orders of distortion is usually less satisfactory. Possible causes of this behaviour are the imperfections of the input signal, which is not perfectly white and Gaussian which leads to accumulated bias as we go up in orders, aliasing, since we are extracting the behaviour of the system on the whole spectral range (0-48kHz) which means that distortions can fall above the Nyquist frequency, and problems due to the very small amplitude of the high powers of a signal of amplitude around 10mV.

6.5 Nonlinear identification of ring modulators

As examples to test the identification methods for 2-input polynomial Hammerstein models, we tested the algorithms on the two ring modulators presented in Appendix B, the Korg MS-50 and the Moogerfooger MF-102.

Korg MS-50

Correlation-based method The extraction of the model filters using the correlation-based method up to order 6 (ie. with polynomial terms of added power lower or equal to 6) has been tested. The filters are displayed in Fig. 6.13 and the error in Table 6.8.

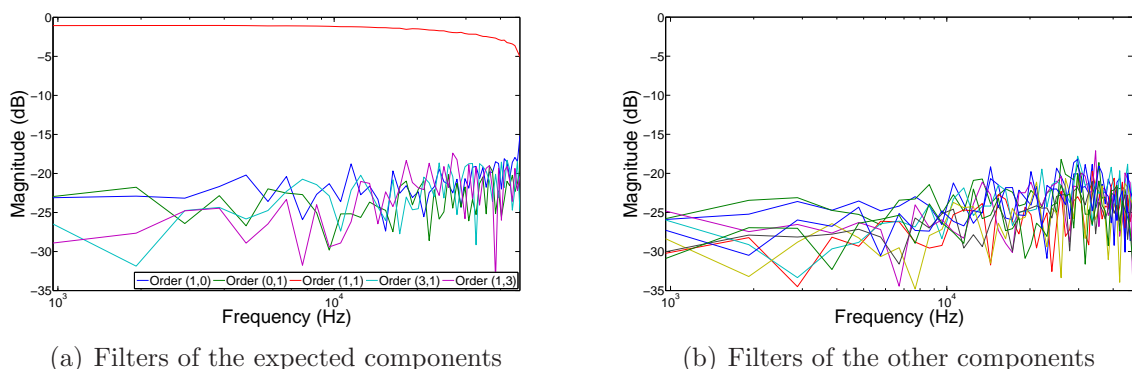


Fig. 6.13 Korg MS-50 ring modulator — filters of the polynomial Hammerstein model

Model	Error
Order 1	99.9277%
Order 2	18.2514%
Order 3	18.2464%
Order 4	18.1817%
Order 5	18.1760%
Order 6	18.1553%

Table 6.8 Korg MS-50 ring modulator — Estimation error of the polynomial Hammerstein model

As expected, the main term of the ring modulator (ie. order (1,1)) corresponds to an extracted flat filter in the musical spectral range. Moreover, the addition of distortion orders in the model visibly improves the accuracy of the modelling, especially when expected orders are added (ie. when we add a new even order). However, this experiment reveals that this method extracts poorly the low-amplitude terms expected from the experiments presented in Chapter 3, probably due to the imperfect non-correlation of the involved signals (e.g. inputs, measurement noise) as well as the low level of the noise input signals.

Explicit least-squares method The explicit least-squares method was tested for order 4. The filters are displayed in Fig. 6.14 and the error in Table 6.9.

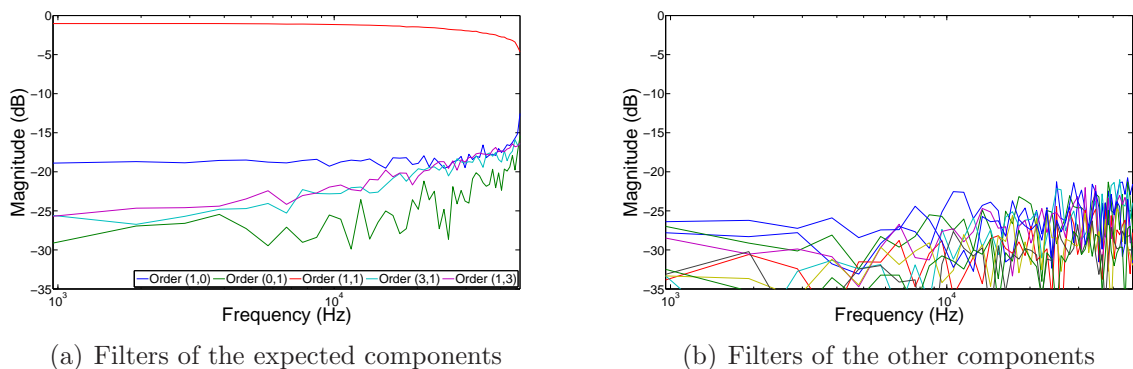


Fig. 6.14 Korg MS-50 ring modulator — filters of the polynomial Hammerstein model using explicit least-squares

As in the case of 1-input systems, this method is an improvement compared to the previous one. In particular, the filters related to the orders (1,0), (0,1) and (3,1) are clearly above the other low-magnitude filters. Furthermore, the filter magnitudes are smoother. This accuracy improvement is confirmed by the error measurement. However, the esti-

Model	Error
Order 4	18.1239%

Table 6.9 Korg MS-50 ring modulator — Estimation error of the polynomial Hammerstein model using explicit least-squares

mation of low-magnitude terms stays very noisy and is comparable to the estimations of polynomial members that should be negligible according to the system equations. Here again, the computation cost of this method is significantly higher than for the previous case with a computation time multiplied by 100.

Moogerfooger MF-102

The same experiments were performed on the Moogerfooger MF-102. The results for the correlation-based method are displayed in Fig. 6.15 and in Table 6.10, and for the explicit least-squares method in Fig. 6.16 and in Table 6.11.

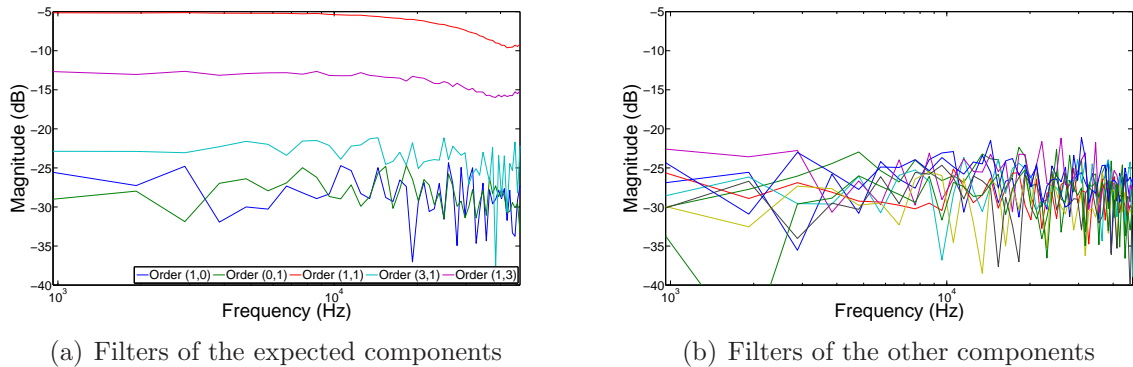


Fig. 6.15 MF-102 ring modulator — filters of the polynomial Hammerstein model

Model	Error
Order 1	99.9871%
Order 2	31.5870%
Order 3	31.5798%
Order 4	30.1895%
Order 5	30.1788%
Order 6	30.0919%

Table 6.10 MF-102 ring modulator — Estimation error of the polynomial Hammerstein model

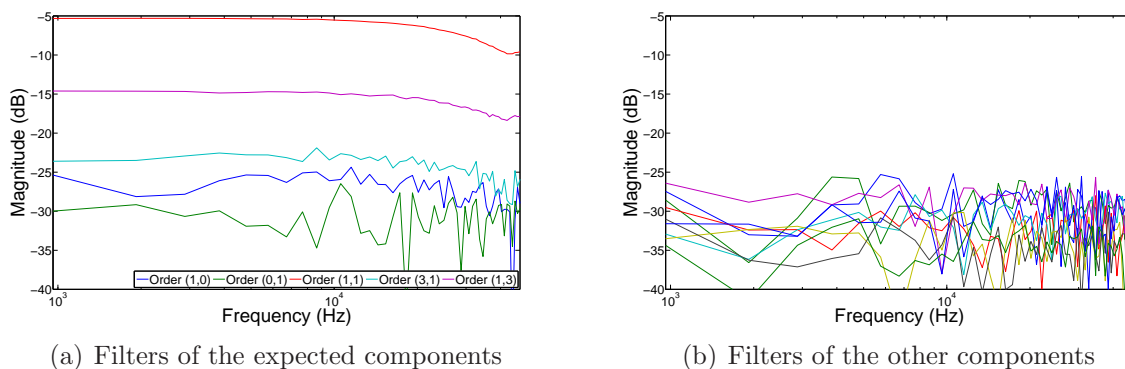


Fig. 6.16 MF-102 ring modulator — filters of the polynomial Hammerstein model using explicit least-squares

Model	Error
Order 4	30.1474%

Table 6.11 MF-102 ring modulator — Estimation error of the polynomial Hammerstein model using explicit least-squares

In the experiments (see Chapter 3), the Moogerfooger seemed to add much more distortion to the output signal. This is confirmed here with much stronger distortion filters for the order (3,1) and (1,3) than for the Korg MS-50.

Otherwise, the observations made for the Korg stays the same, with the filters from the expected orders only slightly above or in the middle of the other ones. The smoothing and the accuracy improvement of the explicit least-squares method is again quite visible.

Remarks on 2-input model identification

Low-magnitude distortion measurement We saw in the measurements made in Section 3.4 that the distortion peaks at maximum input amplitude are only about 30 dB above the measurement noise level at input maximal amplitude. As said before for the Moog filter, in order to avoid distortion due to the saturation of the different audio systems involved in the measurement benchmark, the standard deviation of the Gaussian noise is chosen far below the maximal amplitude allowance, which leads to a much lower distortion level in the output signal of the actual audio effect. This means that some of the distortion peaks will fall below the noise level of the system which will constitute a possible source of inaccuracy in the model identification.

System asymmetries The filter extraction displays the expected asymmetry that exists between the two inputs (modulator and carrier) since the filter of order (n, m) is very different from the one of order (m, n) .

Estimation error In this section, even after the extraction of the main component of the effect (order $(1,1)$), the error stays quite high (15% for the Korg, 30% for the Moogerfooger). The reasons of this error are unclear. Possible explanations, other than simple estimation inaccuracy, include a dependency of the error measurement from the output signal level, a high signal-to-noise ratio in the experiments and an insufficient number of orders in the model.

Number of modelled components As we saw in the measurements, only few significant distortion components below a given order are expected. Then, the algorithm is extracting numerous orders that are not predicted by either the numerical models or our measurements. The tradeoff between the added accuracy by these components (demonstrated by the slightly lower estimation error for models of odd order) and the necessary computation time required for their extraction needs to be taken into account, choosing either a complete polynomial model with very large computation costs or a simplified one with only the few expected components.

6.6 Summary

In this part, we saw that when the electronic circuit drawing of the effect is available, simple models such as finite difference can already achieve a quite accurate reproduction of the system distortion for weakly nonlinear systems. However, hypotheses such as linear input circuitry or perfect characteristics of the electronic components can lead to inaccurate output simulation.

The single-input identification methods presented in Chapter 3 were tested quite successfully on the numerical model of Huovilainen. The results showed that for a system as complex as the Moog filter, simple models are too inaccurate and we would have to use parallel or cascade block-based models to extract the nonlinear characteristics of the system. The estimations on the actual Moog system were promising. Additional measurements using stronger signals could lead to very good modelling of the filter behaviour if we

use enough complex models such as the polynomial Hammerstein approach. It would be also interesting to try to model only the transfer function of the input circuitry in order to get a proper input model for the filtering stage numerical models presented here.

The two-input methods were less successful, but they managed to extract the main distortion components of the two tested ring modulators. Different options exist to improve these results and model the complexity of the behaviour of these systems.

Chapter 7

Conclusion and Future Work

7.1 Summary

This thesis is meant as a preliminary work in the identification of the source of nonlinearities in common analog synthesizers' effects and an investigation on the methods available in literature to approximate the nonlinear behaviour of those systems.

Circuit and nonlinearities The nonlinearities due to the presence of strongly nonlinear components, such as transistors and diodes, in the electronic circuits has been identified for a long time as the main source of distortion in analog audio effects (see Chapter 2). However, as the work of Hoffmann-Burchardi and the experiments presented in Chapter 3 suggest, other audible sources of distortion exist. One could cite the asymmetries present in circuits due to components which characteristics diverge slightly from their reference value, or the distortion introduced by pre- and post-processing units in the effects, which are often ignored in previous studies of those effects.

Nonlinear modelling Two approaches were presented in this thesis, related to two different approaches of the modelling of a system. The black-box approach (Chapter. 4), which use very little or no information from the system, has the drawback to require a large number of parameters that are not always computable in a reasonable amount of time for strongly nonlinear systems, as we saw in Chapter 5. Yet, this class of methods is capable of indiscriminately capturing all nonlinearities.

Circuit modelling (Section 6.2) considers the problem from the circuit of the system and

attempts to extract its behaviour from component models. This method is theoretically very good since it uses a minimal number of parameters. The drawbacks are the reliance on component models that are always approximations of the actual transfer functions of the components, the hypothesis that the components have exactly the reference characteristics provided by manufacturers, and the approximations necessary to compute the system response in a reasonable amount of time.

Multi-input systems

Several opportunities to extend the single-input nonlinear analysis to two- and multi-input systems were presented here, using models such as the polynomial Hammerstein and correlation-based or least-squares methods. Using the multi-variable Hermite polynomial family presented in Appendix D, we were able to write the algorithms of this generalized case. Then, they were tested on two ring modulators with promising results (Section 6.5).

Preliminary comparison results Our preliminary results in Chapter 6 show that it was possible to qualitatively approach the behaviour of the Moog filter using block-based models. However, an accurate reproduction of the distortion trajectories that we saw in the experiments was achieved only in the case of a numerical model, while measurement noise led to unsatisfactory results for the nonlinear identification on the actual effect. The two-input methods met similar limitations to extract distortion from the measurements made on ring modulators.

7.2 Future work

The results presented in this report bring multiple opportunities for improving the understanding and the modelling of nonlinear audio circuits.

Distortion factors

We pointed out several important sources of distortion and their qualitative effect in our experiments and our model testing. A more detailed study of these (such as the influence of self-oscillation for filters) and other factors (such as the choice of the frequency range on

the Moog or the influence of the input and output stages on the ring modulators) would bring a better insight on the system nonlinearities.

Phase and resonance

In this report, we did not study the phase behaviour of the systems and of the different models explored. It will be necessary to consider these aspects if we want to have a deeper understanding of the response of filters when there is a non-zero resonance factor since the phase will affect the position of the resonance peak relative to the filter cutoff frequency.

Identification methods

The cross-correlation-based methods seemed too sensitive to background noise for properly extracting parameters of the Moog system. The explicit resolution of the least-squares equation leads to some improvement but requires a significant amount of additional resources. Other methods such as optimized least-square-based methods (Westwick and Kearney 2003) could lead to better results, and in particular smoother estimated filter, while having the possibility to extend it to multi-input systems. One could also consider the use of different types of noise signals with better ratio amplitude/power than the white Gaussian noise (large amplitude — theoretically infinite — for a relatively limited signal power).

Alternative models

Only a few models were actually tested on our systems. As we saw, the representations we chose were not leading to promising results. Alternative solutions could be tested, such as other block layouts. In particular, it could be interesting to integrate some knowledge that we have of the circuits in these layout such as separately modelling the input, output and processing circuits.

7.3 Conclusion

In this thesis, we had a large overview of the different aspects of studying nonlinear audio effects, from experiments to system modelling and analysis. In this process, we approached very interesting questions related to this topic.

Data collection

The literature lacks of experimental studies on such systems. Knowledge about some particular circuitry behaviour, and the discovery of potential factors such as asymmetric components could lead to a much better understanding of some features of these systems that circuit modelling does not approximate correctly. The collection of data on these systems is a desirable process since less and less of these effects can be found and their maintenance could become problematic due to component ageing and missing replacement parts. In particular, a high-quality measurement database of the system output when using swept-sine and noise input signals could be used as reference for testing the performances of nonlinear models and identification methods.

Nonlinear modelling

Modelling of the electronic systems using circuit modelling is limited by the access to the circuitry of effects, and it requires a customized model for each model. Complex nonlinear black-box models and accurate identification methods are desirable in order to achieve a more systematic study of available systems. Examples from other fields of research which are very advanced on the questions of nonlinear modelling, such as the field of biological systems, could bring a new insight on the available solutions.

Audio effects' modelling

This thesis fully demonstrated that the tools for accurate reproduction of the nonlinear characteristics of nonlinear audio effects are available. The recent development and commercialization of numerous virtual analog products proves the interest of the music community to have access to these vintage sounds. There is no doubt that the domain of study will keep growing in the upcoming decade, taking advantage of the most recent technical and scientific progress.

Appendix A

Electronic components

A.1 Linear elements

Resistor A resistor is characterized by its **resistance** R (in ohms [Ω]) and the equation

$$V = R \times I \quad (\text{A.1})$$

Capacitor A capacitor is characterized by its **capacitance** C (in farads [F]) and the equation

$$C \frac{dV}{dt} = I \quad (\text{A.2})$$

Inductor An inductor is characterized by its **inductance** L (in henries [H]) and the equation

$$L \frac{dI}{dt} = V \quad (\text{A.3})$$

A.2 Diode

A very common nonlinear element in analog synthesizer is the diode. It was widely used before the popularization of transistors for electronics.

Description A diode is a two-terminal electronic components (Fig. A.1). Its two terminals are called *anode* (A) and *cathode* (K). Voltages and currents used in equations are shown on Fig. A.1.

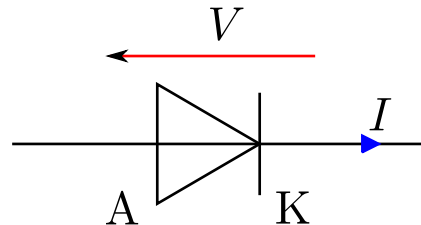


Fig. A.1 Diode symbol and notations

Characteristics Detailed descriptions of the characteristics of these components can be found in literature (Sedra and Smith 1997; Tietze and Schenk 2008) (Fig. A.2). For the purpose of this thesis, we only consider the equation in the *forward* region (positive v) (Sedra and Smith 1997):

$$I = I_S \left(e^{\frac{v}{nV_T}} - 1 \right) \quad (\text{A.4})$$

where I_S is the *saturation current*, V_T is the *temperature voltage*, and n is a constant value depending on the structure of the diode. We assume $n = 1$.

Since the thermal voltage is quite small (few millivolts), the Eq. (A.4) is often approximated as $I \approx I_S e^{\frac{v}{nV_T}}$

Materials Today, most of the diodes on the market are made of silicon, but in the 1950's and the 1960's, many diodes were made of germanium, another semiconductor. The main difference between these two elements appears in the forward voltage V_F . It is around 0.7V for silicon-based diodes while it is more around 0.3V for germanium-based ones.

Remark on temperature influence As we can see in Eq. (A.4), the diode behaviour depends on the temperature voltage, which is a function of the temperature (Tietze and Schenk 2008). A common value used in circuit analysis is $V_T = 26$ mV to room temperatures. Therefore, this value will be considered as a constant only if the temperature of the circuit has been stabilized.

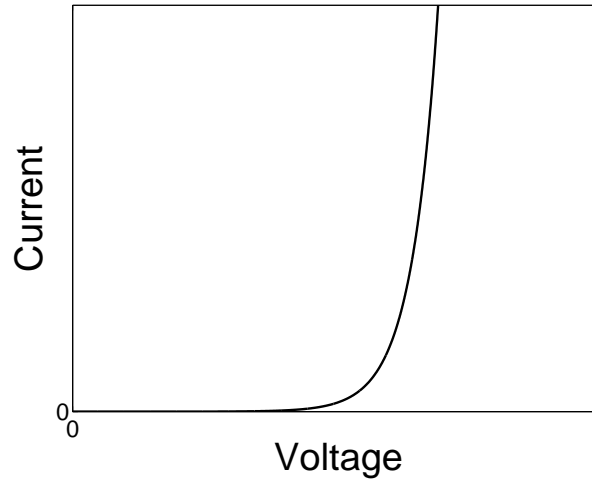


Fig. A.2 Diode I-V relationship in the forward region

A.3 Transistor

Another very common nonlinear element in analog synthesizers is the transistor. They usually are NPN *bipolar junction transistors* (BJTs).

Description A BJT is a three-terminal electronic component (Fig. A.3). Its three terminals are called *base* (B), *collector* (C) and *emitter* (E). Voltages and currents used in equations are shown on Fig. A.3.

Characteristics Detailed descriptions of the characteristics of these components can be found in literature (Sedra and Smith 1997; Tietze and Schenk 2008). For the purpose of this thesis, we only consider the *large-signal* equations (Tietze and Schenk 2008):

$$I_C = I_S e^{\frac{V_{BE}}{V_T}} \left(1 + \frac{V_{CE}}{V_A} \right) \quad (\text{A.5})$$

$$I_B = \frac{I_S}{B_0} e^{\frac{V_{BE}}{V_T}} \quad (\text{A.6})$$

where I_S is the *saturation reverse current*, V_T is the *temperature voltage*, V_A is the *early voltage* and B_0 is the extrapolated current gain (I_C/I_B) for $V_{CE} = 0$.

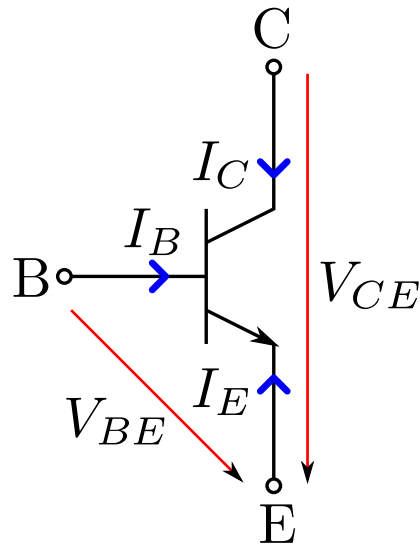


Fig. A.3 NPN bipolar junction transistor (BJT) symbol and notations

Remark on temperature influence Here again, we have the presence of the temperature voltage so the remark made for the diode still applies.

A.4 Operational amplifier

The operational voltage amplifier is the most common type of operational amplifier, and so it is often referred to as simply operational amplifier (OPA). Circuits often make use of operational voltage amplifiers especially for amplification tasks.

Description An OPA is a three-terminal electronic component. Its three terminals are called the *non-inverting input terminal* (P or +), the *inverting input terminal* (N or -) and the output (O). Voltages and currents used in equations are shown on Fig. A.4. It also uses two additional terminals as power supply on a parallel supply circuit that we omit for convenience.

Characteristics Detailed descriptions of the characteristics of these components can be found in literature (Sedra and Smith 1997; Tietze and Schenk 2008). For the purpose of this thesis, we consider that the OPAs are working in their ideal (linear) mode in which (Sedra and Smith 1997):

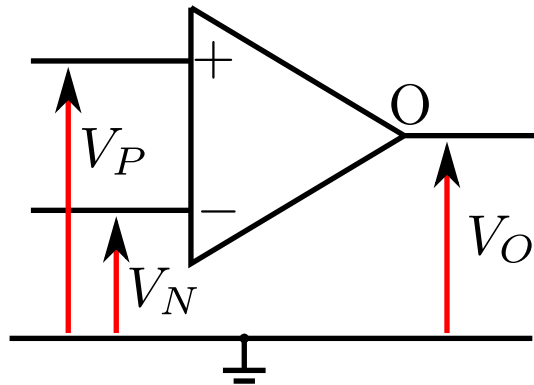


Fig. A.4 Operational amplifier symbol and notations

$$V_O = A(V_+ - V_-) \quad (\text{A.7})$$

where A is the *differential gain* or *open-loop gain*.

Nonlinear behaviour Operational amplifiers are not linear devices. In particular, when the differential voltage between the P-input and the N-input goes above a specific level, the component *saturates* and the output voltage stays at a defined voltage called the *saturation voltage*, which is a strongly nonlinear behaviour. This behaviour can be avoided by using the operational amplifiers with differential voltages staying in the linear zone.

Appendix B

Studied synthesizers' effects

B.1 Moog effects

Moog is a well-known name in the field of analog synthesizers. Since the commercial success of the Moog modular synthesizer in the late 1960's, a large family of synthesizers have been released following this early design and, recently, the Moogerfooger modules have been released as modernized versions of the first modules. In this appendix, we describe some of the features of the Moog effects on which we performed our experiments.

B.1.1 Moog 904A Lowpass filter

We briefly present the complete circuit of the Moog 904A Lowpass Filter as it is provided in the documentation and the circuit drawings (Wyman 1981).

Characteristics

According to Moog documentation (Wyman 1981), the characteristics of the device are:

- Input: impedance $9.2\text{k}\Omega$, nominal level 0dBm (voltage 3.03V), max level 10dBm
- Output: impedance 680Ω , gain 0dB
- Controls: impedance $100\text{k}\Omega$

The control of the filter parameters is done through:

- The control inputs;

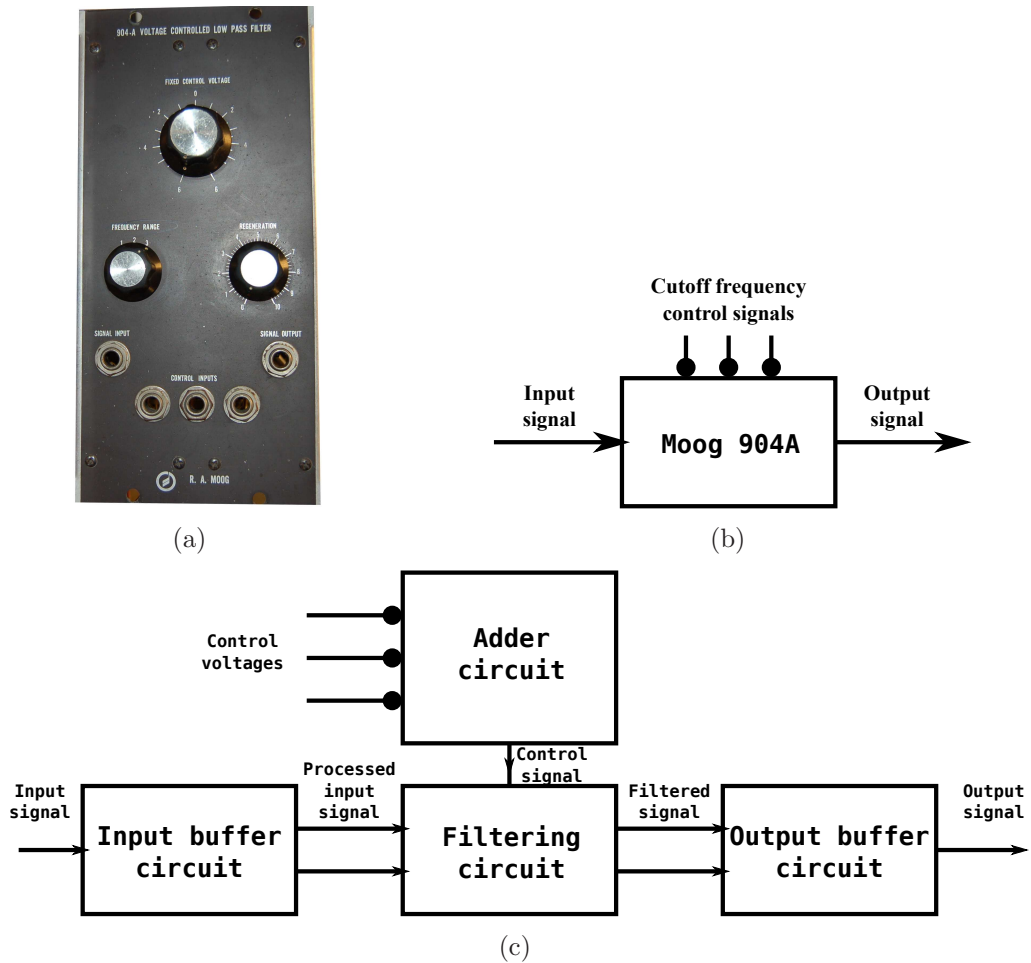


Fig. B.1 Moog ladder filter 904A — (a) Interface, (b) Simplified diagram, (c) Block diagram

- The fixed control voltage knob;
- The frequency range switch;
- the regeneration knob.

The characteristics of the filter are the following:

- Cutoff frequency:

– Range: $1\text{Hz} < f_c < 80\text{kHz}$

- Range switch: 3 positions spaced by 2-octave steps (equivalent to 2V in the control voltage). Range values according to documentation are given in Table B.1
 - Response to control inputs: 1 octave/V
 - Fixed Control Voltage knob: Adjusts the cutoff over 12-octave span
 - Value: $f_{pos} 2^{V_{FCV}+V_{c_1}+V_{c_2}+V_{c_3}}$
- Resonance: peak value depending on input level (stronger for low-level inputs)

Position	1	2	3
Minimal cutoff frequency	1Hz	4Hz	16 Hz
Maximal cutoff frequency	5kHz	20kHz	80kHz

Table B.1 Frequency range values for the range switch

Circuit

General structure The Moog filter is composed of 4 main units, the *adder circuit*, the input buffer, the output buffer and the ladder filter circuit. The components are put on a two-layer board. On the first side (Fig. B.2(a)), we find mainly the filtering circuit, and on the other one (Fig. B.2(b)), the rest of the filter.

Adder circuit The adder circuit (Fig. B.3) performs the adding operation on the three control input voltages to get a single value of voltage control.

Input buffer The input buffer circuit (Fig. B.4) performs the conditioning of the input signal. An offset voltage is introduced in the signal sent to the filter stage.

Output buffer The output buffer circuit (Fig. B.5) performs the conditioning of the output signal, removing the offset voltage.

Filter circuit The filter circuit (Fig. B.6) performs the filtering operation presented in Section 2.1.3.

B.1.2 Moogerfooger MF-102 ring modulator

The Moogerfooger MF-102 (Fig. B.7) was released in 1998 too as a two-effect device, consisting of a low frequency oscillator (LFO) and a ring modulator. The ring modulator subsection is providing a carrier signal. In this thesis, we have an interest in the two-input ring modulator subsection so we ignore the features associated with the rest of the device (LFO and carrier generator). This system is marketed as a descendant of the Moog ring modulator module.

Characteristics

As in previous subsection, the characteristics of this effect are quite different of the original module. Indeed, to adapt the change in musical system standards where the reference voltage at 0dBm ($0.775V_{RMS}$) has replaced the former reference at $5V_{pp}$.

According to Moog documentation (Wyman 1981), the characteristics of the device are:

- Audio input: impedance $1M\Omega$, nominal level $+4dBm$ – $-16dBm$
- Carrier input: nominal level $-4dBm$ ($0.5V_{RMS}$)
- Output: impedance 600Ω , gain $-4dBm$
- Controls: not specified

B.2 Korg MS-50 audio effects

The Korg MS-50 is a modular analog synthesizer that was released in 1978. It consists of various audio effects among which a lowpass filter and a ring modulator. In this appendix are described some of the features of these two systems that we studied for this thesis.

B.2.1 Ring modulator

The Korg MS-50 has a transistor-based ring modulator (Fig. B.8).

Characteristics

According to Korg documentation (Korg 1978), the characteristics of the device are:

- Inputs A and B: nominal level $3V_{pp}$
- Output: nominal level $3V_{pp}$

The ring modulator operation is made such that two inputs at nominal level produces an output at nominal level:

$$y(t) = x_A(t) \times x_B(t) \times 1/3 \quad (\text{B.1})$$

Circuit

The circuit of the ring modulator (Fig. B.9) is also provided in documentation.

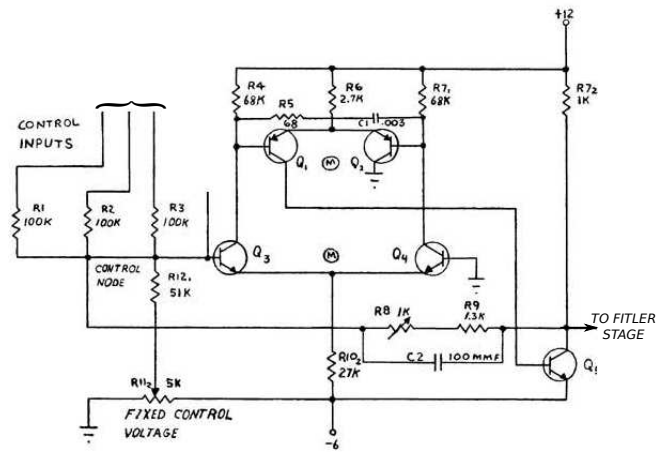


Fig. B.3 Adder circuit of the Moog lowpass filter

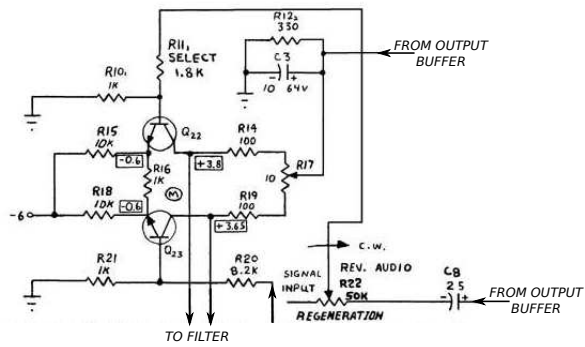


Fig. B.4 Input buffer circuit of the Moog lowpass filter



Fig. B.7 Moogfooger MF-102



Fig. B.8 Ring modulator interface of the Korg MS-50

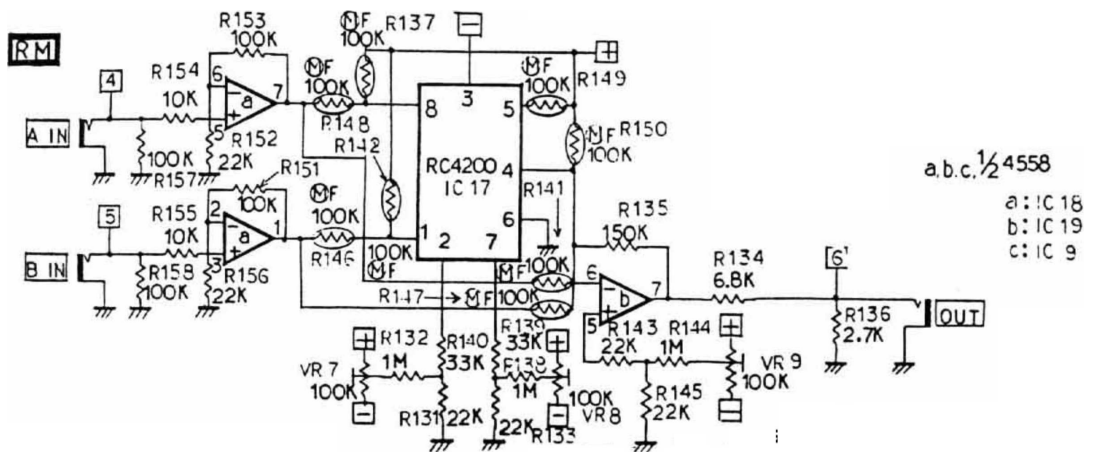


Fig. B.9 Ring modulator circuit of the Korg MS-50

Appendix C

Experimental setups

In this appendix, we detail the different set-ups for the experiments described in Section 3. In each case, a table gives the different states of the involved systems.

C.1 Moog lowpass filter

For the experiments on the Moog lowpass filter, the signals were emitted by the MOTU with no pre-amplification.

C.1.1 DC excitation of the filter

For the experiments looking at processing of DC component by the Moog filter, we applied the settings displayed in Tables C.1 and C.2. Here, we send different DC offset to the filter input while keeping the control voltage and the filter parameters fixed.

Exp. n°	Filter settings			Control voltage	
	Volt. knob	Freq. range	Reson.	Type	Volt.
1-18	-6V	3	0	DC	+4V

Table C.1 Moog filter with DC excitation — Experimental set-ups

C.1.2 Swept-sine excitation of the filter

For the experiments looking at the frequency response of the Moog filter, we applied the settings displayed in Tables C.3 and C.4. Here, we send a swept-sine signal to the filter

Exp. n°	Input signal—1st component		Input signal—2nd component		
	Type	Voltage (digital)	Type	Freq.	Digital ampl.
1-9	DC	-0.6 to +0.6 0.15 steps	-	-	-
10-18	DC	-0.6 to +0.6 0.15 steps	Sine Sine	100Hz 100Hz	0.1 0.1

Table C.2 Moog filter with DC excitation — Experimental variables

input while changing the control voltage through the second control outlet.

Exp. n°	Input signal			Filter settings	Ctrl. volt. 1	Ctrl. volt. 2
	Type	Digital ampl.	Freq.	Volt. knob	Type	Type
19-36	Lin. sweep	0.6	from 100Hz to 10kHz over 20s	-6V	DC	DC
37-42	Log. sweep	0.6	from 50Hz to 5kHz over 20s	-6V	DC	DC

Table C.3 Moog filter with swept-sine excitation — Experimental set-ups

Exp. n°	Filter settings		Ctrl. voltage 1	Ctrl. voltage 2
	Freq. range	Reson.	Ampl.	Digital ampl.
19-27	2	10	+6V	-0.8 to +0.8 0.2 steps
28-36	3	10	+4V	-0.8 to +0.8 0.2 steps
37	3	0	+4V	-0.4
38	3	0	+4V	+0.4
39	3	~7	+4V	-0.4
40	3	~7	+4V	+0.4
41	3	10	+4V	-0.4
42	3	10	+4V	+0.4

Table C.4 Moog filter with swept-sine excitation — Experimental variables

C.1.3 Sinusoidal excitation of the filter

For the experiments looking at the distortion related to amplitude of the Moog filter, we applied the settings displayed in Tables C.5 and C.6. Here, we send a sinusoid signal with different frequencies and a logarithmic amplitude envelope to the filter input while keeping the control voltage and the filter parameters fixed.

Exp. n°	Input signal		Filter settings		Ctrl. voltage	
	Ampl. envelope	Digital ampl.	Volt. knob	Freq. range	Type	Ampl.
43	Log. Sweep	From 0.05 to 0.5 over 20s	-6V	3	DC	+4V

Table C.5 Moog filter with sinusoidal excitation — Experimental set-ups

Exp. n°	Input signal		Filter settings
	Type	Freq.	Reson.
43	Sine	200Hz	0

Table C.6 Moog filter with sinusoidal excitation — Experimental variables

Noise excitation

To identify the parameters of the nonlinear models on the Moog filter, we applied the settings displayed in Tables C.7 and C.8. Here, we send a white Gaussian noise signal while keeping the filter parameters and the control voltage fixed.

Exp. n°	Filter settings			Control voltage	
	Volt. knob	Freq. range	Reson.	Type	Volt.
44	-6V	3	0	DC	+4V

Table C.7 Moog filter with noise excitation — Experimental set-ups

C.2 Korg MS-50 ring modulator

For the experiments on the Korg ring modulator, the signals were emitted by the MOTU with a pre-amplification of -3dB.

C.2.1 Sinusoidal excitation of the Korg ring modulator

In this experiment, two sinusoid with different frequencies are sent to one input of the Korg. The inputs are then reversed. The set-up parameters are displayed in Table C.9.

C.3 Moogerfooger MF-102 ring modulator

For the experiments on the Moog lowpass filter, the signals were emitted by the MOTU with a pre-amplification of -9dB.

Exp. n°	Input signal—1st component	
	Type	Standard deviation (digital)
44	WGN	0.06

Table C.8 Moog filter with noise excitation — Experimental variables

Exp. n°	Input signal A			Input signal A		
	Type	Ampl. (digital)	Freq.	Type	Ampl. (digital)	Freq.
45	Sine	0.6	100Hz	Sine	0.6	1kHz
46	Sine	0.6	1kHz	Sine	0.6	100Hz

Table C.9 Korg ring modulator with sinusoidal excitation — Experimental variables

C.3.1 Sinusoidal excitation of the MF-102

This experiment is identical to the one performed on the Korg ring modulator. The set-up parameters are displayed in Table C.10.

Exp. n°	Input signal A			Input signal A		
	Type	Ampl. (digital)	Freq.	Type	Ampl. (digital)	Freq.
47	Sine	0.6	100Hz	Sine	0.6	1kHz
48	Sine	0.6	1kHz	Sine	0.6	100Hz

Table C.10 MF-102 ring modulator with sinusoidal excitation — Experimental variables

Appendix D

Hermite polynomials

In the context of the identification of polynomial-based nonlinear models based on white Gaussian noise signals, (statistical) Hermite polynomials are essential. Indeed, they have the fundamental property to form an orthogonal polynomial basis respectively to the scalar product weighted by the probability density function of the normal distribution.

D.1 Polynomial expression

On the set of polynomials, if we define the scalar product $\langle \cdot, \cdot \rangle_1$ for the polynomials P and Q :

$$\langle P, Q \rangle_1 = \int_{-\infty}^{+\infty} P(x)Q(x)p(x)dx \quad \text{with } p(x) = \frac{1}{\sqrt{2\pi}}e^{-x^2/2} \quad (\text{D.1})$$

then, an orthogonal polynomial family for that scalar product is called *Hermite* polynomials. In this thesis, we denote $\mathcal{H}^{(m)}(x)$ the Hermite polynomial of order m . These polynomials are defined as:

$$\mathcal{H}^{(m)}(x) = (-1)^m e^{x^2/2} \frac{d^m}{dx^m} e^{-x^2/2} \quad (\text{D.2})$$

The first Hermite polynomials are given by:

$$\begin{aligned}
 \mathcal{H}^{(0)}(x) &= 1 \\
 \mathcal{H}^{(1)}(x) &= x \\
 \mathcal{H}^{(2)}(x) &= x^2 - 1 \\
 \mathcal{H}^{(3)}(x) &= x^3 - 3x \\
 \mathcal{H}^{(4)}(x) &= x^4 - 6x^2 + 3 \\
 \mathcal{H}^{(5)}(x) &= x^5 - 10x^3 + 15x \\
 &\dots
 \end{aligned} \tag{D.3}$$

It is also possible to calculate recursively the polynomials using either a one-step recursion involving differentiation:

$$\begin{aligned}
 \mathcal{H}^{(0)}(x) &= 1 \\
 \mathcal{H}^{(m+1)}(x) &= x\mathcal{H}^{(m)}(x) - \mathcal{H}^{(m)'}(x)
 \end{aligned} \tag{D.4}$$

or a two-step recursion:

$$\begin{aligned}
 \mathcal{H}^{(-1)}(x) &= 0 \\
 \mathcal{H}^{(0)}(x) &= 1 \\
 \mathcal{H}^{(m+1)}(x) &= x\mathcal{H}^{(m)}(x) - m\mathcal{H}^{(m-1)}(x)
 \end{aligned} \tag{D.5}$$

The Hermite polynomials are not normalized since:

$$E [\mathcal{H}^{(m)}(x)\mathcal{H}^{(n)}(x)] = \int_{-\infty}^{+\infty} \mathcal{H}^{(m)}(x)\mathcal{H}^{(n)}(x)p(x)dx = m!\delta_{mn} \tag{D.6}$$

The orthogonality property of the Hermite polynomials is equivalent to say that it creates an orthogonal basis for the polynomial decomposition of the function of a stationary white Gaussian noise signal x in the sense that there exists a unique set of coefficients β_m such that:

$$f(x(t)) = \sum_{m=0}^{+\infty} \beta_m \mathcal{H}^{(m)}(x(t)) \tag{D.7}$$

and

$$E [f(x(t)), \mathcal{H}^{(n)}(x(t))] = \langle f(x(t)), \mathcal{H}^{(n)}(x(t)) \rangle_1 = \alpha_n \quad (\text{D.8})$$

This property is not true anymore for other signals.

Normalized Hermite polynomials In particular, the orthogonality property is not true for signals of non-unitary variance due to the fact that we no longer have $E [PQ] = \langle P, Q \rangle_1$. We have:

$$E [PQ] = \frac{1}{\sigma_x \sqrt{2\pi}} \int_{-\infty}^{+\infty} P(x)Q(x)e^{-\frac{x^2}{2\sigma_x^2}} dx \quad (\text{D.9})$$

which can be rewritten:

$$E [PQ] = \frac{1}{\sqrt{2\pi}} \int_{-\infty}^{+\infty} P(\sigma_x y)Q(\sigma_x y)e^{-\frac{y^2}{2}} dy \quad (\text{D.10})$$

Using the terminology proposed by Westwick and Kearney (2003), we define the *normalized Hermite* polynomials $\mathcal{H}_{\mathcal{N}}^{(m)}$ such that in this case:

$$E [\mathcal{H}_{\mathcal{N}}^{(m)} \mathcal{H}_{\mathcal{N}}^{(n)}] = \alpha_m \delta_{mn} \quad (\text{D.11})$$

with α_m chosen such that the term of highest order (m) of $\mathcal{H}_{\mathcal{N}}^{(m)}$ is one.

The condition is thus equivalent to:

$$\frac{1}{\sigma_x^m} \mathcal{H}_{\mathcal{N}}^{(m)}(\sigma_x y) = \mathcal{H}^{(m)}(y) \quad (\text{D.12})$$

or:

$$\mathcal{H}_{\mathcal{N}}^{(m)}(y) = \sigma_x^m \mathcal{H}^{(m)}\left(\frac{y}{\sigma_x}\right) \quad (\text{D.13})$$

and

$$\alpha_m = \sigma_x^{2m} m! \quad (\text{D.14})$$

D.2 Extension for multi-variable polynomials

To work on parameter extraction for multi-input systems, we want to identify nonlinear transfer function using independent white Gaussian noise signals.

D.2.1 Two-variable case

Let's have two independent variables x_1 and x_2 , the probability density function of the system has the property:

$$p(x_1, x_2) = p_1(x_1)p_2(x_2) \quad (\text{D.15})$$

For two zero-mean unitary-variance white Gaussian noises, we have:

$$p_1(x) = p_2(x) = \frac{1}{\sqrt{2\pi}}e^{-x^2/2} \quad (\text{D.16})$$

From this, we can define a scalar product for two-variable polynomials $\langle \cdot, \cdot \rangle_2$ using the weight function p :

$$\langle P, Q \rangle_2 = \int_{-\infty}^{+\infty} \int_{-\infty}^{+\infty} P(x_1, x_2)Q(x_1, x_2)p(x_1, x_2)dx_1dx_2 \quad (\text{D.17})$$

with:

$$p(x_1, x_2) = \frac{1}{2\pi}e^{-x_1^2/2}e^{-x_2^2/2} \quad (\text{D.18})$$

To define a family of polynomials that, as the single-variable Hermite polynomials, will be orthogonal for white Gaussian noise inputs, we need to verify the condition:

$$\begin{aligned} \langle \mathcal{H}^{(m,p)}(x_1, x_2), \mathcal{H}^{(n,q)}(x_1, x_2) \rangle_2 &= \frac{1}{2\pi} \int_{-\infty}^{+\infty} \int_{-\infty}^{+\infty} \mathcal{H}^{(m,p)}(x_1, x_2)\mathcal{H}^{(n,q)}(x_1, x_2)e^{-\frac{x_1^2}{2}}e^{-\frac{x_2^2}{2}}dx_1dx_2 \\ &= \alpha_{m,p}\delta_{m,n}\delta_{p,q} \end{aligned} \quad (\text{D.19})$$

The other condition is that the polynomial with index (m, p) contains the term $x^m y^p$ with coefficient 1.

We see that the scalar product used in Eq. (D.19) has the property to be decoupled between the two variables, so that we can write it:

$$\langle P, Q \rangle_2 = \langle \langle P, Q \rangle_1^{x_1} \rangle_1^{x_2} \quad (\text{D.20})$$

So in the case where P and Q are separable, which means that it exists four polynomials P_1, P_2, Q_1 and Q_2 such that $P(x_1, x_2) = P_1(x_1)P_2(x_2)$ and $Q(x_1, x_2) = Q_1(x_1)Q_2(x_2)$, we

have:

$$\langle P, Q \rangle_2 = \langle P_1, Q_1 \rangle_1 \langle P_2, Q_2 \rangle_1 \quad (\text{D.21})$$

With this observation, and knowing that the single-input Hermite polynomials are orthogonal for the scalar product $\langle \cdot, \cdot \rangle_1$, we can see that the two-input Hermite polynomials can be built as separable using the equation:

$$\mathcal{H}^{(m,p)}(x_1, x_2) = \mathcal{H}^{(m)}(x_1) \mathcal{H}^{(p)}(x_2) \quad (\text{D.22})$$

which leads to:

$$\begin{aligned} \langle \mathcal{H}^{(m,p)}(x_1, x_2), \mathcal{H}^{(n,q)}(x_1, x_2) \rangle_2 &= \langle \mathcal{H}^{(m)}(x_1), \mathcal{H}^{(n)}(x_1) \rangle_1 \langle \mathcal{H}^{(p)}(x_2), \mathcal{H}^{(q)}(x_2) \rangle_1 \\ &= m! \delta_{m,n} p! \delta_{p,q} \end{aligned} \quad (\text{D.23})$$

which corresponds to the condition defined in Eq. (D.23) with $\alpha_{m,p} = m!p!$.

The first two-input Hermite polynomials are given by:

$$\begin{aligned} \mathcal{H}^{(0,0)}(x_1, x_2) &= 1 \\ \mathcal{H}^{(1,0)}(x_1, x_2) &= x_1 \\ \mathcal{H}^{(0,1)}(x_1, x_2) &= x_2 \\ \mathcal{H}^{(2,0)}(x_1, x_2) &= x_1^2 - 1 \\ \mathcal{H}^{(1,1)}(x_1, x_2) &= x_1 x_2 \\ \mathcal{H}^{(0,2)}(x_1, x_2) &= x_2^2 - 1 \\ \mathcal{H}^{(3,0)}(x_1, x_2) &= x_1^3 - 3x_1 \\ \mathcal{H}^{(2,1)}(x_1, x_2) &= x_1^2 x_2 - x_2 \\ \mathcal{H}^{(1,2)}(x_1, x_2) &= x_1 x_2^2 - x_1 \\ \mathcal{H}^{(0,3)}(x_1, x_2) &= x_2^3 - 3x_2 \\ &\dots \end{aligned} \quad (\text{D.24})$$

Normalized Hermite polynomials As in the case of a single variable, the Hermite polynomials are no longer orthogonal if the variance of each signal is non-unitary. Again,

we can define the two-input normalized Hermite polynomials as:

$$\mathcal{H}_{\mathcal{N}}^{(m,p)}(x_1, x_2) = \sigma_{x_1}^m \sigma_{x_2}^p \mathcal{H}^{(m,p)}\left(\frac{x_1}{\sigma_{x_1}}, \frac{x_2}{\sigma_{x_2}}\right) \quad (\text{D.25})$$

D.2.2 N -variable case

Following the same process, we see that in the case of N independent white Gaussian noise variables, we will have a family of N -variable Hermite polynomials such that:

$$\mathcal{H}^{(m_1, \dots, m_N)}(x_1, \dots, x_N) = \mathcal{H}^{(m_1)}(x_1) \dots \mathcal{H}^{(m_N)}(x_N) \quad (\text{D.26})$$

and for the normalized case:

$$\mathcal{H}_{\mathcal{N}}^{(m_1, \dots, m_N)}(x_1, \dots, x_N) = \sigma_{x_1}^{m_1} \dots \sigma_{x_N}^{m_N} \mathcal{H}_{\mathcal{N}}^{(m_1, \dots, m_N)}\left(\frac{x_1}{\sigma_{x_1}}, \dots, \frac{x_N}{\sigma_{x_N}}\right) \quad (\text{D.27})$$

References

- Akaike, H. 1974, dec. A new look at the statistical model identification. *Automatic Control, IEEE Transactions on* 19 (6): 716 – 723.
- Bendat, J. 1998. *Nonlinear system techniques and applications*. New York: Wiley.
- Bode, H. 1961. A new tool for the exploration of unknown electronic music instrument performances. *J. Audio Eng. Soc* 9 (4): 264–6.
- Bode, H. 1967. The multiplier type ring modulator. *Electronic Music Review* 1: 9–15.
- Bode, H. 1984. History of electronic sound modification. *J. Audio Eng. Soc* 32 (10): 730–9.
- Chadabe, J. 2000. The electronic century part iii: Computers and analog synthesizers. *Electronic Musician* 16 (4).
- Chang, F., and R. Luus. 1971. A noniterative method for identification using Hammerstein model. *Automatic Control, IEEE Transactions on* 16 (5): 464–8.
- Chen, S., and S. Billings. 1989. Representations of non-linear systems: the NARMAX model. *International Journal of Control* 49 (3): 1013–32.
- Chen, S., S. A. Billings, and P. M. Grant. 1990. Non-linear system identification using neural networks. *International Journal of Control* 51: 1191–214.
- Davies, H. 1976. A simple ring-modulator. *Musics* 6: 3–5.
- Durr, B. 1976. Le synthétiseur. *Cahiers Recherche/Musique* (3): 11–28.
- Evans, C., D. Rees, L. Jones, and M. Weiss. 1996. Periodic signals for measuring nonlinear Volterra kernels. *Instrumentation and Measurement, IEEE Transactions on* 45 (2): 362–71.
- Farina, A., and A. Farina. 2000. Simultaneous measurement of impulse response and distortion with a swept-sine technique. In *108th AES Convention*, 18–22.

- Fontana, F., and M. Civolani. 2010. Modeling of the ems vcs3 voltage—controlled filter as a nonlinear filter network. *Audio, Speech, and Language Processing, IEEE Transactions on* 18 (4): 760–72.
- Giannakis, G., and E. Serpedin. 2001. A bibliography on nonlinear system identification. *Signal Process.* 81: 533–80.
- Greblicki, W. 1997. Nonparametric approach to Wiener system identification. *Circuits and Systems I: Fundamental Theory and Applications, IEEE Transactions on* 44 (6): 538–45.
- Haber, R., and L. Keviczky. 1999. *Nonlinear system identification : input-output modeling approach*. New York: Springer Verlag.
- Haber, R., and H. Unbehauen. 1990. Structure identification of nonlinear dynamic systems—a survey on input/output approaches. *Automatica* 26: 651–77.
- Hall, C. F., and E. L. Hall. 1977. A nonlinear model for the spatial characteristics of the human visual system. *Systems, Man and Cybernetics, IEEE Transactions on* 7 (3): 161–70.
- Hélie, T. 2006. On the use of Volterra series for real-time simulations of weakly nonlinear analog audio devices: Application to the Moog ladder filter. In *Proceedings of the 9th International Conference on Digital Audio Effects (DAFx)*, 7–12.
- Hélie, T. 2010. Volterra series and state transformation for real-time simulations of audio circuits including saturations: Application to the Moog ladder filter. *IEEE Transactions on Audio, Speech and Language Processing* 18 (4): 747–59.
- Hélie, T., and M. Hasler. 2004. Volterra series for solving weakly non-linear partial differential equations: application to a dissipative Burgers' equation. *International Journal of Control* 77 (12): 1071–82.
- Hennequin, R. 2008. *Mesure, identification et simulation de systèmes non-linéaires à mémoire : Vers un sampler d'effets*. Master's thesis, Paris 6.
- Hoffmann-Burchardi, R. 2008. Digital simulation of the diode ring modulator for musical applications. *Proceedings of the International Conference on Digital Audio Effects*: 165–8.
- Hoffmann-Burchardi, R. 2009. Asymmetries make the difference: A nonlinear model of transistor-based analog ring modulators. *Proceedings of the International Conference on Digital Audio Effects*: 438–41.
- Huovilainen, A. 2004. Non-linear digital implementation of the Moog ladder filter. In *Proceedings of the 9th International Conference on Digital Audio Effects (DAFx)*, 5–8.

- Kearney, R. E., and I. W. Hunter. 1983. System identification of human triceps surae stretch reflex dynamics. *Experimental Brain Research* 51: 117–127. 10.1007/BF00236809.
- Korenberg, M. 1988. Identifying nonlinear difference equation and functional expansion representations: The fast orthogonal algorithm. *Annals of Biomedical Engineering* 16: 123–142. 10.1007/BF02367385.
- Korg. 1978. *Korg monophonic synthesizer MS-50 — Owner's manual*.
- Lee, Y. W., and M. Schetzen. 1965. Measurement of the Wiener kernels of a non-linear system by cross-correlation. *International Journal of Control* 2 (3): 237–54.
- Leontaritis, I., and S. Billings. 1985a. Input-output parametric models for non-linear systems part i: deterministic non-linear systems. *International Journal of Control* 41 (2): 303–28.
- Leontaritis, I. J., and S. A. Billings. 1985b. Input-output parametric models for non-linear systems part ii: stochastic non-linear systems. *International Journal of Control* 41 (2): 329–44.
- Mathews, V. 1991, jul. Adaptive polynomial filters. *Signal Processing Magazine, IEEE* 8 (3): 10–26.
- Moog, R. 1969. Electronic high-pass and low-pass filters employing the base to emitter diode resistance of bipolar transistors.
- Müller, S.; Massarani, P. 2001. Transfer-function measurement with sweeps. *J. Audio Eng. Soc* 49 (6): 443–71.
- Novak, A. 2009. *Identification of Nonlinear Systems in Acoustics*. Ph. D. thesis, Université du Maine, Le Mans, France AND Czech Technical University, Prague, Czech Republic.
- Oppenheim, A. V., R. W. Schaffer, and J. R. Buck. 1999. *Discrete-time signal processing (2nd ed.)*. Upper Saddle River, NJ, USA: Prentice-Hall, Inc.
- Rébillat, M., R. Hennequin, Étienne Corteel, and B. F. Katz. 2011. Identification of cascade of hammerstein models for the description of nonlinearities in vibrating devices. *Journal of Sound and Vibration* 330 (5): 1018–38.
- Reed, M., and M. Hawksford. 1996, oct. Identification of discrete volterra series using maximum length sequences. *Circuits, Devices and Systems, IEE Proceedings - 143* (5): 241–8.
- Rice, S. O. 1973. Volterra systems with more than one input port? distortion in a frequency converter. *Bell System Technical Journal* 52 (8): 1255–70.

- Rife, Douglas D.; Vanderkooy, J. 1989. Transfer-function measurement with maximum-length sequences. *J. Audio Eng. Soc* 37 (6): 419–44.
- Sedra, A., and K. Smith. 1997. *Microelectronic circuits* (4th ed.). Oxford University Press.
- Sorenson, H. 1985. *Kalman Filtering: Theory and Application*. Montvale, NJ: IEEE Press.
- Stilson, T., and J. Smith. 1996. Analyzing the Moog VCF with considerations for digital implementation. In *Proceedings of the International Computer Music Conference*, 398–401. Citeseer.
- Stinchcombe, T. E. 2006. A study of the korg ms10 & ms20 filters.
- Stinchcombe, T. E. 2008. Analysis of the Moog transistor ladder and derivative filters.
- Stockhausen, K. 1967. Notes on Mixtur. *Electronic Music Review* 1: 16–7.
- Tietze, U., and C. Schenk. 2008. *Electronic Circuits: Handbook for Design and Applications* (2nd ed.). Springer Verlag.
- Välimäki, V., and A. Huovilainen. 2006. Oscillator and filter algorithms for virtual analog synthesis. *Computer Music Journal* 30 (2): 19–31.
- Volterra, V. 1930. *Theory of functionals*. Blackie.
- Westwick, D. T., and R. E. Kearney. 2003. *Identification of Nonlinear Physiological Systems*. IEEE Biomedical Engineering Book Series. IEEE Press/Wiley.
- Wiener, R. 1958. *Nonlinear problems in random theory*. MIT Press.
- Wyman, D. 1981. *Moog Modular Owner's Manual*. Sound Arts.
- Young, G. 1989. *The Sackbut Blues: Hugh Le Caine, Pioneer in Electronic Music*. Ottawa: National Museum of Science and Technology.